Engineering Fracture Mechanics 304 (2024) 110123

Contents lists available at ScienceDirect

Engineering Fracture Mechanics

journal homepage: www.elsevier.com/locate/engfracmech

A finite element implementation of phase-field approach of fracture for nonlinear solid shells including inelastic material behavior

Angel Valverde-González [a,b], Pavan Kumar Asur Vijaya Kumar [d], Adria Quintanas-Corominas [e], José Reinoso [b,c,f,*]

[a] IMT School for Advanced Studies, Piazza San Francesco 19, Lucca 55100, Italy
[b] Grupo de Ingeniería de Materiales y Estructuras. Departamento de Mecánica de Medios Continuos y Teoría de Estructuras, Universidad de Sevilla, Escuela Técnica superior de Ingeniería, Camino de los Descubrimientos s/n, 41092 Sevilla, Spain
[c] Escuela Politécnica Superior, Universidad de Sevilla, C/ Virgen de África, 41011 Sevilla, Spain
[d] Institute of Lightweight Design and Structural Biomechanics, Technische Universität Wien, Getreidemarkt 9, 1060 Vienna, Austria
[e] Barcelona Supercomputing Center (BSC), Plaça Eusebi Güell, 1-3, Barcelona, 08034, Catalonia, Spain
[f] ENGREEN - Laboratory of Engineering for Energy and Environmental Sustainability, Universidad de Sevilla, Spain

ARTICLE INFO

Keywords:
Phase-field model
Inelastic material behavior
Shell structures
Locking

ABSTRACT

The parametrization of shell structures using the so-called solid shell concept has been widely exploited in the last decades. This trend is mainly attributed to the relatively simple kinematic treatment of solid shells in the corresponding finite element formulation in conjunction with the use of unmodified three-dimensional material laws, among other aspects. In the present investigation, we provide a comprehensive finite element implementation of solid shells incorporating: (i) the use of Enhanced Assumed Strain (EAS) and the Assumed Natural Strain (ANS) methods to prevent locking issues, (ii) the phase-field approach for triggering fracture events, and (iii) some representative inelastic material models. The current modular implementation has been integrated into the FE package ABAQUS via the user-defined routine UEL. Several representative examples demonstrate the applicability of the present formulation.

1. Introduction

Shells are ubiquitous in many engineering applications and structures. The use of shell-like structures can be traced back to the origin of civilizations. Differing from beam and column structures, which primarily rely on 1D elements to withstand the external loading, shell structures use curved, often thin, surfaces to create strong and lightweight architectural forms. The new industrial and high-tech revolution during the 21st century is leading to a new paradigmatic use of shells. For instance, contemporary shell structures often incorporate parametric design, new materials and digital fabrication techniques in conjunction with biomimetic designs, which aim at developing lightweight and adaptive designs that resemble the efficiency and resilience of natural shells.

Recent developments generally demand the comprehensive understanding of fracture events in shells, especially when these structures are made from materials which exhibit nonlinear responses, such as elasto-plastic, visco-elastic materials, among many others. The development of robust numerical methods for the description of inelastic material response in conjunction to fracture in shells still represents a scientific and technical challenge. Within this concern, the advent of the phase-field approach has been profusely exploited in the last two decades, offering a solid-rooted and versatile computational method for the prediction of fracture events in solids. Stemming from the seminal energetic vision of Griffith [1], which was revisited by Francfort and Marigo [2] and

* Corresponding author at: Grupo de Ingeniería de Materiales y Estructuras. Departamento de Mecánica de Medios Continuos y Teoría de Estructuras, Universidad de Sevilla, Escuela Técnica superior de Ingeniería, Camino de los Descubrimientos s/n, 41092 Sevilla, Spain.
E-mail address: jreinoso@us.es (J. Reinoso).

https://doi.org/10.1016/j.engfracmech.2024.110123
Received 20 February 2024; Received in revised form 19 April 2024; Accepted 28 April 2024
Available online 15 May 2024

Nomenclature

Latin Symbols

$\mathbf{A}$	Macroscopical tensor accounting for the microscopic viscous stretches
$\mathbf{b}$	Left Cauchy–Green tensor
$\mathbf{B}(\mathbf{d})$	Displacement-strain operator
$\mathbf{C}$	Right Cauchy–Green tensor
$\mathbf{d}$	Nodal displacements
d_1, d_2, d_3	Dimensionless parameters accounting for stress triaxiality
$\mathbf{E}$	Green–Lagrange strain tensor
$\mathbf{E}_i, \mathbf{e}_i$	Cartesian basis vectors
$\mathbf{F}$	Deformation gradient tensor
$g(\mathfrak{d})$	Phase-field degradation function
$\mathbf{G}^i, \mathbf{g}^i$	Contravariant basis vectors
$\mathbf{G}_i, \mathbf{g}_i$	Covariant basis vectors
G^{ij}, g^{ij}	Contravariant metric tensors
G_{ij}, g_{ij}	Covariant metric tensors
h	Element size
H	Thickness of numerical sample
$\mathbf{I}$	Second identity tensor
I_n	N-th invariant
$\mathbf{J}, \mathbf{j}$	Jacobian matrix
J	Determinant of the deformation gradient tensor
$\mathbf{k}_{[\bullet\bullet]}$	Jacobi stiffness matrix
$k(\alpha)$	Isotropic hardening modulus
K	Linear hardening coefficient
$\hat{L}$	Gateaux directional derivative
L	Length of numerical sample
$\mathbf{L}^p$	Plastic velocity gradient
m	Testing rate sensitivity for visco-hyperplasticity
$\mathbf{M}$	Matrix for interpolation of EAS enhancing strains
$\mathbf{M}^e$	Mandel stress tensor
$\mathbf{N}$	Reference outward normal vector
$\mathbf{N}(\boldsymbol{\xi})$	Shape functions
n_n	Number of nodes
$\mathbf{n}_a$	Principal elastic strain directions
$\bar{\mathbf{P}}$	Microdeformation mapping tensor
$\bar{\mathbf{P}}_{\mathbf{X}}$	Pre-microdeformation mapping tensor
$\mathbf{P}$	First Piola–Kirchhoff stress tensor
$\mathbf{R}^e$	Elastic rotation tensor
R, r	Radius of numerical sample
$\mathbf{S}$	Second Piola–Kirchhoff stress tensor
t	Current experiment time
$\mathbf{T}$	Traction vector
$\mathbf{u}$	Displacement field
$U(J)$	Volumetric contribution to the Helmholtz free energy density
$\mathbf{U}^e$	Elastic stretch tensor
v	Testing rate
W	Width of numerical sample
$\mathbf{X}$	Position vector in the reference configuration

Greek Symbols

α	Plastic hardening parameter
α_{sat}	Saturation level for plastic hardening
$\mathrm{d}\Omega$	Volume differential
$\partial\Omega$	Boundary of the solid in the current configuration
$\partial\Omega_0$	Boundary of the solid in the initial configuration
Γ_c	Internal discontinuity
$\dot{\gamma}$	Lagrange plastic multiplier, rate of accumulated plastic strain
$\gamma_l(\mathfrak{d}, \nabla_{\mathbf{X}}\mathfrak{d})$	Crack energy density
$\dot{\gamma}^0$	Referential plastic strain rate
κ	Bulk modulus
λ	Microscopical stretch
μ	Shear modulus
$\mu^{\text{visco},\gamma}$	Viscous shear modulus for viscous branch γ
Ω	Body domain in the current configuration
Ω_0	Body domain in the initial configuration
Π	Potential energy
ψ	Parameter accounting for stress triaxiality
Ψ	Helmholtz free energy density
Ψ_0	Threshold for the Helmholtz free energy density
Ψ^{elas}	Elastic contribution to the Helmholtz free energy density
Ψ^{plas}	Plastic contribution to the Helmholtz free energy density
$\Psi^{\text{visco},\gamma}$	Viscous contribution of the subnetwork γ to the Helmholtz free energy density
Ψ^{vplas}	Viscoplastic contribution to the Helmholtz free energy density
$\boldsymbol{\sigma}$	Cauchy stress tensor
σ_y	Yield stress
$\boldsymbol{\tau}$	Kirchhoff stress tensor
τ^{γ}	Relaxation time for the viscous branch γ
Υ	Internal variables stored at integration point level
$\boldsymbol{\varepsilon}$	Elastic strain tensor
ε_a	Principal elastic strains
$\boldsymbol{\varphi}$	Mapping motion vector
$\boldsymbol{\varsigma}$	Nodal incompatible strains
ξ^i	Curvilinear coordinates
$\boldsymbol{\xi}_{A,B,C,D}$	Collocation points for ANS interpolation of shear locking
$\boldsymbol{\xi}_{M,N,O,P}$	Collocation points for ANS interpolation of trapezoidal locking

Other math symbols

$\mathbb{C}, \mathbb{c}$	Constitutive Jacobi matrix
$\mathcal{D}$	Clausius-Duhem dissipated energy
$\mathcal{G}_C$	Critical energy release rate
$\mathcal{I}$	Internal variables
$\mathcal{K}$	Small conditioning parameter
ℓ	Length scale parameter
$\mathcal{L}_{\mathbf{X}}$	Initial microscopical stretch space
$\mathcal{L}_{\mathbf{x}}$	Current microscopical stretch space
$\mathfrak{d}$	Phase-field parameter
$\mathfrak{V}^{\bullet}$	Space of admissible magnitudes
$\mathbb{P}$	Fourth-order projector tensor
$\mathcal{R}^{[\bullet]}$	Residual vector

Acronyms

ANS	Assumed Natural Strain
EAS	Enhanced Assumed Strain
FEM	Finite Element Method
UEL	User Element Subroutine

Superscripts and subscripts

$[\bullet]_{+}$	Tensile (positive) contribution
$[\bullet]_{,A}$	Partial derivative with respect to A
$[\bullet]_{-}$	Compressive (negative) contribution
$[\bullet]^{-1}$	Inverse of a matrix
$[\bullet]_{0}$	Magnitude evaluated at the center of the element
$[\bullet]_{\mathbf{b}}$	Magnitude in bottom shell surface
$[\bar{\bullet}]$	Prescribed variables (vector)/ Deviatoric contribution (matrix)
$[\bullet]^{e}$	Elastic contribution of a matrix/vector
$[\bullet]_{\text{ext}}$	External contribution
$[\bullet]_{n}$	Magnitude in previous converged time step
$[\bullet]_{n+1}^{k}$	Magnitude in current time step at iteration k
$[\bullet]^{p}$	Plastic contribution of a matrix/vector
$[\bullet]_{\mathbf{t}}$	Magnitude in top shell surface
$[\tilde{\bullet}]$	EAS-enhanced contribution
$\text{tr}[\bullet]$	Trace operator
$[\bullet]^{\mathbf{u}}$	Displacement-derived contribution

Math operators

$\otimes$	Dyadic tensor product operator
$\Delta[\bullet]$	Increment of a magnitude
$\delta[\bullet]$	Variation of a magnitude
$\Delta_{*}[\bullet]$	Directional derivative operator
$\mathcal{L}_{v}[\bullet]$	Lie's derivative operator
$\|\|\bullet\|\|$	Norm of a magnitude
$\partial[\bullet]$	Partial derivative of a magnitude
$\nabla_{\mathbf{X}}[\bullet]$, $\nabla_{\mathbf{x}}[\bullet]$	Material gradient operator

subsequently regularized by Bourdin et al. [3], phase-field methods of fracture have being developed for different purposes. We recall the different approaches for the treatment of tension-compression decomposition [4–7] and alternative approaches [8,9], ductile fracture [10–16], multi-physics fracture [17–21], concrete-like materials [22] and anisotropic solids [23–25], among many others.

However, the use of phase-field methods of fracture in shells have received a more reduced attention so far. Several investigations have been carried out in the last decade recalling different structural models, see [26–30]. Alternative works have been devoted for the fracture modeling in solid shells, which are characterized by the parametrization of the director vectors of the top and bottom surfaces of the shell body, see [31–34], where different numerical technologies to alleviate locking events are employed such as Enhanced assumed strain (EAS) and the Assumed natural strain (ANS) methods, among others. Moreover, the solid shell modeling technique holds an advantage over other methods due to its capacity to directly incorporate sophisticated models such as hyperplasticity, visco-hyperelasticity, visco-hyperplasticity, thermo-mechanical, and more. This is attributed to the full integration of the Finite Element framework. For further insights into the conformity of constitutive models with the Helmholtz free energy in solid shells, refer to [35,36].

At present, only few formulations integrating solid shell parametrization with fracture modeling attributes within the spirit of the phase-field method have been implemented [37,38], and more recently extended to thermo-mechanical fracture [36,39,40], and global-local FE approaches [41]. The bibliography notably lacks references on inelastic fracture modeling in solid shells. Therefore, the aim of this work is to present the development of a phase-field approach for the simulation of fracture events in solid shells using the EAS and the ANS methods to prevent locking observed in the response of inelastic materials. Specifically, we particularize the material response prior to fracture stemming from: (i) the hyper-plastic material from Borden et al. [13], (ii) the viscous-hyper-elastic proposed by Linder et al. [42] and further developed by [43], and (iii) an innovative visco-hyper-plastic formulation developed by Chester [44]. Careful attention is devoted to the numerical treatment of the implemented formulation

and the corresponding numerical implementation. This approach will undergo comprehensive testing through various numerical examples. First, for validation purposes, experiments are conducted on a notched square tensile plate and, a double-notched asymmetric specimen especially to compare with the benchmark example. Subsequently, cylindrical samples under mixed loading conditions will be explored, involving diverse bending and traction scenarios. Despite the additional computational cost they incur and the possibility of encountering convergence issues, the EAS and ANS methods come in handy in these analyses in alleviating locking pathologies stemming from the structure.

The organization of the manuscript is as follows. Section 2 introduces the fundamental kinematic formulation for nonlinear Continuum Mechanics problems for solid shells with full integration, the phase-field approach for fracture and the EAS and ANS techniques for the mitigation of locking effects. Subsequently, Section 3 presents the variational formulation for the inelastic problem, delving deeply into the particularities for the hyperplastic, visco-hyperelastic and visco-hyperplastic models. Efforts exhibited in Section 4 are directed to simulate various numerical tests, first to validate the trio of implemented inelastic approaches and then, moving to more complex problems, to test its functionality in addressing fracture for solid shells with full integration while, at the same time, avoiding locking pathologies. Some final remarks and conclusions are provided in Section 5. In order to shed light on the employed technique, an appendix is provided for the FE implementation with the intention of providing the reader the opportunity to replicate such results.

2. Basic formulation

2.1. Kinematic definitions for nonlinear solid shells

Let $\Omega_0 \subset \mathbb{R}^n$ be a reference configuration for the n-dimensional Euclidean space with its delimiting boundary $\partial\Omega_0 \subset \mathbb{R}^{n-1}$. For each position vector in the reference configuration $\mathbf{X} \in \Omega_0$, we define a primary field of vector values displacement field $\mathbf{u}(\mathbf{X}, t) : \Omega_0 \times [0, t] \to \mathbb{R}^n$ and the phase-field damage variable $\mathfrak{d}(\mathbf{X}, t) : \Omega_0 \times [0, t] \to [0, 1]$ for each time instant t, see Fig. 1.

The shell body is parameterized by a set of curvilinear coordinates ξ^i $(i = 1, 2, 3)$, whose first two coordinates represent an in-plane mid-surface (ξ^1, ξ^2), whereas third direction (ξ^3) represents thickness direction, with $\boldsymbol{\xi} = \{\xi^1, \xi^2, \xi^3\}$. The body undergoes deformation due to Dirichlet boundary conditions prescribed by displacement field $\bar{\mathbf{u}}$ on $\partial\Omega_{0,\mathbf{u}}$ and Neumann conditions of traction $\bar{\mathbf{T}} = \mathbf{P} \cdot \mathbf{N}$ on $\partial\Omega_{0,\mathbf{t}}$, with $\mathbf{P}$ being the first Piola–Kirchhoff stress and $\mathbf{N}$ being the reference outward normal. The motion from the reference configuration $\mathbf{X} \in \Omega_0$ onto the current configuration $\mathbf{x} \in \Omega_t$ is defined via a singular valued continuous map $\boldsymbol{\varphi}(\mathbf{X}, t) : \Omega_0 \times [0, t] \to \mathbb{R}^3$, such that $\mathbf{x} = \boldsymbol{\varphi}(\mathbf{X}, t) = \mathbf{X} + \mathbf{u}(\mathbf{X}, t)$ for each time instant t.

The covariant and contravariant basis vectors in curvilinear setting on the reference $(\mathbf{G}_i)$ and the current $(\mathbf{g}_i)$ configurations are defined as

$$\mathbf{G}_i(\boldsymbol{\xi}) := \frac{\partial \mathbf{X}(\boldsymbol{\xi})}{\partial \xi^i}; \quad \mathbf{g}_i(\boldsymbol{\xi}) := \frac{\partial \mathbf{x}(\boldsymbol{\xi})}{\partial \xi^i} \tag{1}$$

The relations between the covariant and contravariant basis reads $\mathbf{G}_i \cdot \mathbf{G}^j = \delta_i^j$, where δ_i^j is the Dirac's delta. The metric tensor is defined as

$$\mathbf{G} := G^{ij}\mathbf{G}_i \otimes \mathbf{G}_j = G_{ij}\mathbf{G}^i \otimes \mathbf{G}^j, \tag{2}$$

with $G_{ij} = \mathbf{G}_i \cdot \mathbf{G}_j$ and $G^{ij} = \mathbf{G}^i \cdot \mathbf{G}^j$. Contravariant and covariant base vectors can be obtained as

$$\mathbf{G}^i = G^{ij}\mathbf{G}_j; \qquad \mathbf{G}_i = G_{ij}\mathbf{G}^j, \tag{3}$$

and correspondingly we can obtain

$$\mathbf{G}^i \cdot \mathbf{G}^k = G^{ij}\mathbf{G}_j \cdot \mathbf{G}^k = G^{ij}\delta_j^k = G^{ik}. \tag{4}$$

The definition of the displacement derived deformation gradient that maps the unit reference element d$\mathbf{X}$ onto the current element d$\mathbf{x}$ is given by

$$\mathbf{F}^{\mathbf{u}} := \frac{\partial \boldsymbol{\varphi}(\mathbf{X}, t)}{\partial \mathbf{X}} = \mathbf{G} + \nabla_{\mathbf{X}}\mathbf{u}. \tag{5}$$

The displacement dependent Green–Lagrange strain tensor $\mathbf{E}^u$ in curvilinear settings can be written in terms of deformation gradient as

$$\mathbf{E}^u = \frac{1}{2}\left[(\mathbf{F}^u)^{\mathrm{T}} \cdot \mathbf{F} - \mathbf{G}_i \cdot \mathbf{G}_j\right](\mathbf{G}^i \otimes \mathbf{G}^j) = \frac{1}{2}\left[\mathbf{g}_i \cdot \mathbf{g}_j - \mathbf{G}_i \cdot \mathbf{G}_j\right]\mathbf{G}^i \otimes \mathbf{G}^j = \frac{1}{2}\left[g_{ij} - G_{ij}\right]\mathbf{G}^i \otimes \mathbf{G}^j. \tag{6}$$

Recalling the solid shell approach, the position vectors of reference $\mathbf{X}$ and current $\mathbf{x}$ configurations are represented by the points from the bottom $(\mathbf{X_b})$ and top $(\mathbf{X_t})$ surface respectively as, see Fig. 1

$$\mathbf{X}(\boldsymbol{\xi}) = \frac{1}{2}(1+\xi^3)\mathbf{X}_{\mathbf{t}}(\xi^1, \xi^2) + \frac{1}{2}(1-\xi^3)\mathbf{X}_{\mathbf{b}}(\xi^1, \xi^2); \quad \mathbf{x}(\boldsymbol{\xi}) = \frac{1}{2}(1+\xi^3)\mathbf{x}_{\mathbf{t}}(\xi^1, \xi^2) + \frac{1}{2}(1-\xi^3)\mathbf{x}_{\mathbf{b}}(\xi^1, \xi^2), \tag{7}$$

where the subscripts b and t denote the corresponding points in the bottom and the top surface.

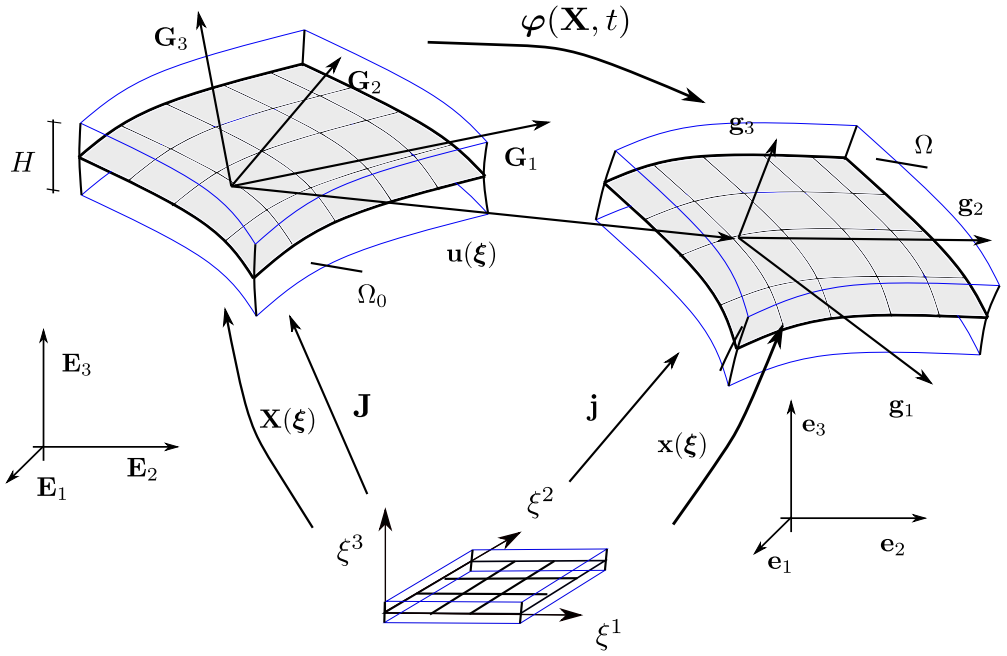

Fig. 1. Description of the shell body in the curvilinear setting. The coordinate systems for the reference Ω_0 and current Ω_t configurations are denoted by $\{\mathbf{E}_i\}_{i=1,3}$ and $\{\mathbf{e}_i\}_{i=1,3}$, respectively; the points in the reference and current configurations are denoted by $\mathbf{X}$ and $\mathbf{x}$ respectively, whereas the corresponding Jacobi matrices are given by $\mathbf{J}$ and $\mathbf{j}$.

2.2. The phase-field approach for fracture of solid shells

The phase-field approach for fracture arises from the postulation made by Griffith [1], establishing the competition between the strain energy Ψ and the energy required for the system to create new surfaces coined as crack energy. Within this context, the potential of the system takes the form

$$\Pi_\Omega(\mathbf{E}) + \Pi_{\Gamma_c} = \int_{\Omega_0} \Psi(\mathbf{E})\,\mathrm{d}\Omega + \int_{\Gamma_c} \mathcal{G}_C\,\mathrm{d}\Gamma. \tag{8}$$

Here, $\Psi(\mathbf{E})$ is the strain energy density function, Γ_c is the internal discontinuity, and $\mathcal{G}_C$ is the critical energy release rate along the crack set Γ_c. Notice that, within the context of the solid shell formulation, total Green–Lagrangian strain $\mathbf{E}$ is used for the computation of Ψ. Concerning the surface energy Π_{Γ_c} associated with the sharp crack (Fig. 2(a)), it is approximated with a smeared crack as in Fig. 2(b) using the phase-field parameter $\mathfrak{d} \in [0,1]$, and an internal length scale $\ell \in \mathbb{R}^+$ controlling the width of the smeared crack. Here $\mathfrak{d} = 0$ represents an intact material, whereas $\mathfrak{d} = 1$ represents a fully damaged material. Consequently, the crack energy function takes the form

$$\Pi_{\Gamma_c} = \int_{\Gamma_c} \mathcal{G}_C \mathrm{d}\Gamma \approx \int_{\Omega_0} \mathcal{G}_C \gamma_l(\mathfrak{d}, \nabla\mathfrak{d})\ \mathrm{d}\Omega, \tag{9}$$

where $\gamma_l(\mathfrak{d};\nabla\mathfrak{d})$ is the crack energy density. Without any loss of generality, in the sequel, we employ the AT2 formulation [3,45] which leads to the expression

$$\int_{\Omega_0} \gamma_l(\mathfrak{d}, \nabla\mathfrak{d})\ \mathrm{d}\Omega = \int_{\Omega_0} \mathcal{G}_C \left[\frac{\mathfrak{d}^2}{2\ell} + \frac{\ell}{2}|\nabla\mathfrak{d}|^2\right]\ \mathrm{d}\Omega. \tag{10}$$

Due to the smeared nature of the damage, the strain energy functional is modified to degrade the stiffness by adding a degradation function $g(\mathfrak{d})$. Consequently, the potential defined in Eq. (8) takes the form

$$\Pi_\Omega(\mathbf{E}) + \Pi_{\Gamma_c} = \int_{\Omega_0} g(\mathfrak{d})\Psi(\mathbf{E})\,\mathrm{d}\Omega + \int_{\Omega_0} \mathcal{G}_C \gamma_l(\mathfrak{d}, \nabla_{\mathbf{X}}\mathfrak{d})\ \mathrm{d}\Omega. \tag{11}$$

Here, the degradation function $g(\mathfrak{d})$ of the strain energy density has a quadratic dependence on the phase-field parameter

$$g(\mathfrak{d}) = (1-\mathfrak{d})^2 + \mathcal{K}, \tag{12}$$

where $\mathcal{K}$ is a small parameter used to avoid ill-conditioning of the stiffness matrix upon damage.

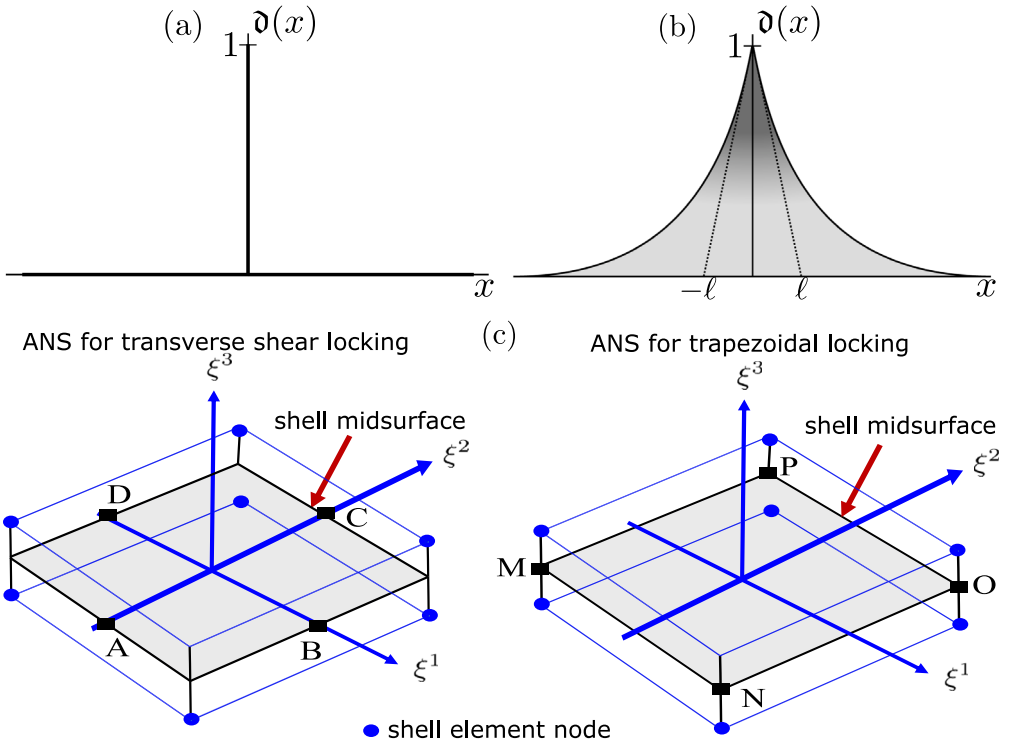

Fig. 2. Phase-field approach for fracture: Sharp (a) and diffusive (b) crack morphologies. (c) Application of ANS method: identification of collocation points for the alleviation of (Left image) transverse shear ($\xi_A = (0,-1,0)$, $\xi_B = (1,0,0)$, $\xi_C = (0,1,0)$ and $\xi_D = (-1,0,0)$), and (Right image) trapezoidal locking ($\xi_M = (-1,-1,0)$, $\xi_N = (1,-1,0)$, $\xi_O = (1,1,0)$ and $\xi_P = (-1,1,0)$) pathologies.

Complying with the anzats generated due to Eq. (7), the phase-field variable is averaged by the values at the top ($\mathfrak{d}_t$) and bottom ($\mathfrak{d}_b$) surfaces of the solid shell as

$$\mathfrak{d}(\boldsymbol{\xi}) = \frac{1}{2}(1+\xi^3)\mathfrak{d}_t(\xi^1,\xi^2) + \frac{1}{2}(1-\xi^3)\mathfrak{d}_b(\xi^1,\xi^2). \tag{13}$$

2.3. Interpolation of the enhancing strains: the EAS method

As will be described in the forthcoming Section, the alleviation of membrane and Poisson thickness locking is performed by the EAS technique, which enhances the displacement-derived Green–Lagrangian strain tensor $\mathbf{E}^u$ by considering an incompatible Green–Lagrangian strain tensor $\tilde{\mathbf{E}}$ via additive decomposition of the total Green–Lagrangian tensor $\mathbf{E}$ as $\mathbf{E} = \mathbf{E}^u + \tilde{\mathbf{E}}$, see [46] for more details. Retrieving the orthogonality condition with respect to the discrete approximation stress field, the enhanced strains are interpolated at the element level using the operator $\mathbf{M}(\boldsymbol{\xi})$:

$$\tilde{\mathbf{E}} = \left[\frac{\det\mathbf{J_0}}{\det\mathbf{J}}\right]\mathbf{T}\mathbf{M}(\boldsymbol{\xi})\boldsymbol{\varsigma}, \tag{14}$$

where $\boldsymbol{\varsigma}$ is the vector containing all the incompatible modes of strains; $\mathbf{J} = \{\mathbf{G}_1, \mathbf{G}_2, \mathbf{G}_3\}$ and $\mathbf{J_0} = \{\mathbf{G}_{1(0)}, \mathbf{G}_{2(0)}, \mathbf{G}_{3(0)}\}$ are the Jacobian in the reference configuration and its evaluation at the element center, respectively; and matrix $\mathbf{T}$ accounts for the terms $\mathbf{J}$ and $\mathbf{J_0}$ as $T_{ij} = \mathbf{G}_i \cdot \mathbf{G}_{j(0)}$. For the local operator $\mathbf{M}(\boldsymbol{\xi})$, defined in isoparametric coordinates ξ, without any loss of generality, we adopt the model proposed in Vu-Quoc and Tan [47]. Further details on the interpolation are given in Section 3.1.2.

It is worth mentioning that the consideration of assumed strains requires the modification of the right Cauchy–Green tensor $\mathbf{C}$:

$$\mathbf{C} := \mathbf{C}^u + \tilde{\mathbf{C}} = 2(\mathbf{E}^u + \tilde{\mathbf{E}}) + \mathbf{G}. \tag{15}$$

2.4. The ANS method

Transverse shear and trapezoidal locking effects are alleviated using the ANS technique. Such locking arises from the poor displacement interpolation over the thickness. In this regard, Dvorkin and Bathe [48] treatment of the shear components of the Green–Lagrange strain tensor (E_{13} and E_{23}) and those developed by Betsch and Stein [49] for the transverse normal strain components (E_{33}) are used. The ANS interpolation of the shear components considers four collocation points, which are defined

in the natural space as (Fig. 2(c), left): $\boldsymbol{\xi}_A = (0,-1,0)$, $\boldsymbol{\xi}_B = (1,0,0)$, $\boldsymbol{\xi}_C = (0,1,0)$ and $\boldsymbol{\xi}_D = (-1,0,0)$. Consequently, the modified interpolation reads

$$\begin{bmatrix} E_{13}^{ANS} \\ E_{23}^{ANS} \end{bmatrix} = \begin{bmatrix} (1-\xi^2)E_{13}(\boldsymbol{\xi}_A) + (1+\xi^2)E_{13}(\boldsymbol{\xi}_C) \\ (1+\xi^1)E_{23}(\boldsymbol{\xi}_B) + (1-\xi^1)E_{23}(\boldsymbol{\xi}_D) \end{bmatrix} = \begin{bmatrix} N^A E_{13}(\boldsymbol{\xi}_A) + N^B E_{13}(\boldsymbol{\xi}_C) \\ N^C E_{23}(\boldsymbol{\xi}_B) + N^D E_{23}(\boldsymbol{\xi}_D) \end{bmatrix}. \tag{16}$$

The proposed ANS interpolation for the treatment of the thickness strain component E_{33} accounts for the definition of four collocation points located on the corners of the shell midsurface (Fig. 2(c), right): $\boldsymbol{\xi}_M = (-1,-1,0)$, $\boldsymbol{\xi}_N = (1,-1,0)$, $\boldsymbol{\xi}_O = (1,1,0)$ and $\boldsymbol{\xi}_P = (-1,1,0)$. The associated modified interpolation component reads

$$\begin{aligned} E_{33}^{ANS} &= \sum_{m=1}^{4} N^m(\xi^1,\xi^2)E_{33}, \qquad m = M,N,O,P \\ N^m(\xi^1,\xi^2) &= \frac{1}{4}\left(1+\xi_m^1\xi^1\right)\left(1+\xi_m^2\xi^2\right), \quad \text{with } \xi_m^1,\xi_m^2 = \pm 1. \end{aligned} \tag{17}$$

The ANS method is combined with the EAS method in the current formulation in order to modify the interpolation associated with the transverse shear strains components E_{13} and E_{23}, and the transverse normal component E_{33}.

3. Modeling framework and finite element implementation details

This Section is devoted to presenting the variational formalism for the three material models for fully-integrated solid shells including fracture events through the phase-field approach of fracture and inelastic material effects within the context of nonlinear Continuum Mechanics. It is important to highlight that this trio of approaches stems from derivations based on the field Hu–Washizu principle, presented in Section 3.1.1, which will be used as the starting landmark in this Section. Accordingly, details on the its FE implementation are provided in Section 3.1.2. Additional details are given in Appendix, where we offer code listings that can serve as valuable aids during the implementation process.

Subsequently, delving into their distinct theoretical aspects, each inelastic model is individually discussed, encompassing: (i) ductile fracture in hyperplasticity by Borden et al. [13] (Section 3.2); (ii) Visco-hyperelastic material following the work of Valverde-González et al. [43] and proposed by Linder et al. [42] (Section 3.3); and (iii) the visco-hyperplastic framework proposed by Chester in [44] which can be found as open source in the website of the author are outlined in Section 3.4.

3.1. Governing functional and finite element implementation

3.1.1. Governing functional

Stemming from the use of the EAS method, in the present contribution, we adopt the additive decomposition of the Green–Lagrange strain tensor into the displacement derived part $\mathbf{E}^u$ and an enhancing counterpart $\tilde{\mathbf{E}}$, leading to $\mathbf{E} = \mathbf{E}^u + \tilde{\mathbf{E}}$. As a consequence, the multi-field Hu–Washizu formulation represents the point of departure for the proposed modellling approach, where the displacement field $\mathbf{u}$, the enhancing strain $\tilde{\mathbf{E}}$, the stress field $\mathbf{S}$, and the phase-field parameter $\mathfrak{d}$ are the independent fields. The total potential energy functional reads

$$\Pi(\mathbf{u},\tilde{\mathbf{E}},\mathbf{S},\mathfrak{d}) = \int_{\Omega_0} [g(\mathfrak{d})\Psi_+(\mathbf{E}) + \Psi_-(\mathbf{E})]\,\mathrm{d}\Omega + \int_{\Omega_0} g(\mathfrak{d})[\mathbf{S}:\tilde{\mathbf{E}}]\,\mathrm{d}\Omega + \int_{\Omega_0} \mathcal{G}_C\left[\frac{\mathfrak{d}^2}{2\ell} + \frac{\ell}{2}|\nabla\mathfrak{d}|^2\right]\,\mathrm{d}\Omega - \Pi_{\text{ext}}(\mathbf{u}), \tag{18}$$

where $\Pi_{\text{ext}}(\mathbf{u})$ is the external contribution due to the prescribed boundary conditions; $\mathbf{S}$ is the second Piola–Kirchhoff stress tensor; and Ψ_+ and Ψ_- are the tensile and compressive contributions to the stored energy, respectively, meaning that only tensile states do contribute to crack growth. Consider the variation of primary fields $(\mathbf{u},\tilde{\mathbf{E}},\mathbf{S},\mathfrak{d})$ as $(\delta\mathbf{u},\delta\tilde{\mathbf{E}},\delta\mathbf{S},\delta\mathfrak{d})$ in the appropriate spaces $(\mathfrak{V}^u,\mathfrak{V}^{\mathfrak{d}},\mathfrak{V}^{\tilde{E}},\mathfrak{V}^{\mathbf{S}})$. It is worth noting that $\mathfrak{V}^u = \left\{\delta\mathbf{u}\in[H^1(\Omega_0)] : \delta\mathbf{u} = \mathbf{0} \text{ on } \partial\Omega_{0,\mathbf{u}}\right\}$ is the space of admissible displacement variations, $\mathfrak{V}^{\tilde{E}} = \{\delta\tilde{\mathbf{E}}\in L^2(\Omega_0)\}$ is the space of the admissible enhancing strains, $\mathfrak{V}^{\mathbf{S}} = \{\delta\mathbf{S}\in L^2(\Omega_0)\}$ denotes the space stress field, and $\mathfrak{V}^{\mathfrak{d}} = \left\{\delta\mathfrak{d}\in[H^1(\Omega_0)] : \nabla_{\mathbf{X}}\delta\mathfrak{d}\cdot\mathbf{N} = 0 \text{ on } \partial\Omega_0\right\}$ is the space of admissible test functions for the phase-field damage parameter. Upon recalling the orthogonality condition between the spaces of the enhanced strains and the stresses, the stress field can be removed in the subsequent derivations. Accordingly, the approximate solution can be obtained via the stationary value of the governing functional, Eq. (18):

$$\delta\Pi = \frac{\partial\Pi}{\partial\mathbf{u}}\cdot\delta\mathbf{u} + \frac{\partial\Pi}{\partial\tilde{\mathbf{E}}} : \delta\tilde{\mathbf{E}} + \frac{\partial\Pi}{\partial\mathfrak{d}}\delta\mathfrak{d} + \frac{\partial\Pi}{\partial\nabla_{\mathbf{x}}\mathfrak{d}}\cdot\nabla_{\mathbf{x}}\delta\mathfrak{d} - \delta\Pi_{\text{ext}} = 0. \tag{19}$$

The second law of thermodynamics can be ensured using the Clausius-Duhem inequality. With $\mathcal{D}$ representing the dissipated energy, it becomes apparent that, for internal variables $\mathcal{I}$, the local actions take the form:

$$\mathcal{D} = \left[\mathbf{S} - \partial_{\mathbf{E}}\Psi\right] : \dot{\mathbf{E}} - \partial_{\mathcal{I}}\Psi : \dot{\mathcal{I}} \geq 0. \tag{20}$$

Adding the damage as an internal variables due to Eq. (19), and keeping the room for other internal variables, Eq. (20) takes the form,

$$\mathcal{D} = \left[\mathbf{S} - \partial_{\mathbf{E}}\Psi\right] : \dot{\mathbf{E}} - \partial_{\mathfrak{d}}\Psi : \dot{\mathfrak{d}} - \partial_{\mathcal{I}}\Psi : \dot{\mathcal{I}} \geq 0. \tag{21}$$

Note that in degenerated shell elements, the lack of full integration necessitates additional modifications to satisfy the Clausius-Duhem inequality within constitutive modeling.

Consequently, the following general expression of the weak form of the multi-field problem is reached

$$\begin{aligned}\delta\Pi(\mathbf{u},\tilde{\mathbf{E}},\mathfrak{d}) = &\int_{\Omega_0}\left(g(\mathfrak{d})[\mathbf{S}:\mathbf{E}^u]_+ + [\mathbf{S}:\mathbf{E}^u]_-\right)\,\mathrm{d}\Omega + \int_{\Omega_0} g(\mathfrak{d})[\mathbf{S}:\tilde{\mathbf{E}}]\,\mathrm{d}\Omega \\ &+ \int_{\Omega_0}\mathcal{G}_C\left[\frac{\mathfrak{d}}{\ell}\delta\mathfrak{d} + \ell\nabla\mathfrak{d}\cdot\nabla\delta\mathfrak{d}\right]\,\mathrm{d}\Omega + \int_{\Omega_0} g'(\mathfrak{d})\Psi_+(\mathbf{u})\,\mathrm{d}\Omega - \delta\Pi_{\text{ext}}(\mathbf{u}) = 0.\end{aligned} \tag{22}$$

Here $g'(\mathfrak{d}) = -2(1-\mathfrak{d})$, is the derivative of the degradation function. Residual equations for the FEM discretization for each of the primary fields can be obtained as

$$\mathcal{R}^{\mathbf{u}}(\mathbf{u},\tilde{\mathbf{E}},\mathfrak{d},\delta\mathbf{u}) = \delta\mathbf{u}^{\mathrm{T}}\left[\int_{\Omega_0} g(\mathfrak{d})\mathbf{B}(\mathbf{d})^{\mathrm{T}}\cdot\mathbf{S}\,\mathrm{d}\Omega\right] - \delta\Pi_{\text{ext}}(\mathbf{u}) = 0, \tag{23}$$

$$\mathcal{R}^{\tilde{\mathbf{E}}}(\mathbf{u},\tilde{\mathbf{E}},\mathfrak{d},\delta\tilde{\mathbf{E}}) = \delta\tilde{\mathbf{E}}^{\mathrm{T}}\left[\int_{\Omega_0} g(\mathfrak{d})\mathbf{M}^{\mathrm{T}}(\xi)\cdot\mathbf{S}\,\mathrm{d}\Omega\right] = 0, \tag{24}$$

$$\mathcal{R}^{\mathfrak{d}}(\mathbf{u},\tilde{\mathbf{E}},\mathfrak{d},\delta\mathfrak{d}) = \delta\mathfrak{d}^{\mathrm{T}}\left[\int_{\Omega_0}\mathcal{G}_C\left[\frac{1}{\ell}\mathbf{N}^{\mathrm{T}}(\xi)\mathfrak{d} + \ell\mathbf{B}^{\mathfrak{d}}(\xi)^{\mathrm{T}}\cdot\nabla_{\mathbf{X}}\mathfrak{d}\right]\mathrm{d}V + \int_{\Omega_0} g'(\mathfrak{d})\mathbf{N}^{\mathrm{T}}(\xi)\Psi_+(\mathbf{u})\mathfrak{d}\,\mathrm{d}\Omega\right] = 0. \tag{25}$$

In line with [38], the reference and the current geometries are interpolated through standard trilinear shape functions N^I ($\mathbf{N}(\xi)$ in matrix notation) as

$$\mathbf{X} = \sum_{I=1}^{n_n} N^I(\xi)\mathbf{X}_I = \mathbf{N}(\xi)\overline{\mathbf{X}} \quad \text{and} \quad \mathbf{x} = \sum_{I=1}^{n_n} N^I(\xi)\mathbf{x}_I = \mathbf{N}(\xi)\overline{\mathbf{x}}, \tag{26}$$

whereas the interpolation of the displacement field ($\mathbf{u}$), its variation ($\delta\mathbf{u}$) and its increment ($\Delta\mathbf{u}$) renders

$$\mathbf{u} \approx \mathbf{N}(\xi)\mathbf{d}, \quad \delta\mathbf{u} \approx \mathbf{N}(\xi)\delta\mathbf{d}, \quad \Delta\mathbf{u} \approx \mathbf{N}(\xi)\Delta\mathbf{d}. \tag{27}$$

In the previous expressions, $\mathbf{X}_I$ and $\mathbf{x}_I$ are the discrete nodal values and $n_n = 8$, being arranged into the respective global vectors $\overline{\mathbf{X}}$ and $\overline{\mathbf{x}}$ for both configurations; $\mathbf{d}$ represents the nodal displacement vector at the element level.

The compatible strain field ($\mathbf{E}^u$), its variation ($\delta\mathbf{E}^u$) and its increment ($\Delta\mathbf{E}^u$) are computed via the displacement-strain $\mathbf{B}(\mathbf{d})$ operator as

$$\mathbf{E}^u \approx \mathbf{B}(\mathbf{d})\mathbf{d}, \quad \delta\mathbf{E}^u \approx \mathbf{B}(\mathbf{d})\delta\mathbf{d}, \quad \Delta\mathbf{E}^u \approx \mathbf{B}(\mathbf{d})\Delta\mathbf{d}. \tag{28}$$

whereas the assumed strains at the element level are interpolated through the operator $\mathbf{M}(\xi)$ as

$$\tilde{\mathbf{E}} \approx \mathbf{M}(\xi)\varsigma, \quad \delta\tilde{\mathbf{E}} \approx \mathbf{M}(\xi)\delta\varsigma, \quad \Delta\tilde{\mathbf{E}} \approx \mathbf{M}(\xi)\Delta\varsigma. \tag{29}$$

In line with the previous scheme, the phase-field ($\mathfrak{d}$), its variation ($\delta\mathfrak{d}$), and its increment ($\Delta\mathfrak{d}$) are computed as

$$\mathfrak{d} = \mathbf{N}(\xi)\overline{\mathfrak{d}}, \quad \delta\mathfrak{d} = \mathbf{N}(\xi)\delta\overline{\mathfrak{d}}, \quad \Delta\mathfrak{d} = \mathbf{N}(\xi)\Delta\overline{\mathfrak{d}}, \tag{30}$$

where $\overline{\mathfrak{d}}$ are the nodal phase-field values. Finally, the material gradient of the phase-field, its variation and its increment are interpolated via the operator $\mathbf{B}^{\mathfrak{d}}$ as

$$\nabla_{\mathbf{X}}\mathfrak{d} = \mathbf{B}^{\mathfrak{d}}(\xi)\overline{\mathfrak{d}}, \quad \nabla_{\mathbf{X}}\delta\mathfrak{d} = \mathbf{B}^{\mathfrak{d}}(\xi)\delta\overline{\mathfrak{d}}, \quad \nabla_{\mathbf{X}}\Delta\mathfrak{d} = \mathbf{B}^{\mathfrak{d}}(\xi)\Delta\overline{\mathfrak{d}}. \tag{31}$$

Note that as described in [38], the assumed strains are condensed out at the element level. This is exploited for the construction of the tangent matrices, since the tangent matrices resulting from the linearization procedure through the Gateaux directional derivative for the displacement and the phase-field are solved using a staggered solution scheme. The corresponding tangent operators can be computed as follows

$$\hat{L}[\mathcal{R}^{\mathbf{u}}](\mathbf{u},\delta\mathbf{u},\Delta\mathbf{u},\mathfrak{d},\tilde{\mathbf{E}},\Delta\tilde{\mathbf{E}}) = \mathcal{R}^{\mathbf{u}}(\mathbf{u},\delta\mathbf{u},\mathfrak{d},\tilde{\mathbf{E}}) + \Delta_{\mathbf{u}}\mathcal{R}^{\mathbf{u}}\Delta\mathbf{u} + \Delta_{\tilde{\mathbf{E}}}\mathcal{R}^{\mathbf{u}}\Delta\tilde{\mathbf{E}} + \Delta_{\mathfrak{d}}\mathcal{R}^{\mathbf{u}}\Delta\mathfrak{d}, \tag{32}$$

$$\hat{L}[\mathcal{R}^{\tilde{\mathbf{E}}}](\mathbf{u},\Delta\mathbf{u},\mathfrak{d},\tilde{\mathbf{E}},\delta\tilde{\mathbf{E}},\Delta\tilde{\mathbf{E}}) = \mathcal{R}^{\tilde{\mathbf{E}}}(\mathbf{u},\mathfrak{d},\tilde{\mathbf{E}},\delta\tilde{\mathbf{E}}) + \Delta_{\mathbf{u}}\mathcal{R}^{\tilde{\mathbf{E}}}\Delta\mathbf{u} + \Delta_{\tilde{\mathbf{E}}}\mathcal{R}^{\tilde{\mathbf{E}}}\Delta\tilde{\mathbf{E}} + \Delta_{\mathfrak{d}}\mathcal{R}^{\tilde{\mathbf{E}}}\Delta\mathfrak{d}, \tag{33}$$

$$\hat{L}[\mathcal{R}^{\mathfrak{d}}](\mathbf{u},\Delta\mathbf{u},\mathfrak{d},\delta\mathfrak{d},\Delta\mathfrak{d},\tilde{\mathbf{E}},\Delta\tilde{\mathbf{E}}) = \mathcal{R}^{\mathfrak{d}}(\mathbf{u},\mathfrak{d},\delta\mathfrak{d},\tilde{\mathbf{E}}) + \Delta_{\mathbf{u}}\mathcal{R}^{\mathfrak{d}}\Delta\mathbf{u} + \Delta_{\tilde{\mathbf{E}}}\mathcal{R}^{\mathfrak{d}}\Delta\tilde{\mathbf{E}} + \Delta_{\mathfrak{d}}\mathcal{R}^{\mathfrak{d}}\Delta\mathfrak{d}, \tag{34}$$

where $\Delta_*[\bullet]$ represents the directional derivative operator with respect to the field $*$. The resulting system renders

$$\begin{bmatrix}\mathbf{k}_{dd} & \mathbf{k}_{d\varsigma} & \mathbf{0}\\ \mathbf{k}_{\varsigma d} & \mathbf{k}_{\varsigma\varsigma} & \mathbf{0}\\ \mathbf{0} & \mathbf{0} & \mathbf{k}_{\bar{\mathfrak{d}}\bar{\mathfrak{d}}}\end{bmatrix}\begin{bmatrix}\Delta\mathbf{d}\\ \Delta\varsigma\\ \Delta\overline{\mathfrak{d}}\end{bmatrix} = \begin{bmatrix}\mathcal{R}^{\mathbf{u}}_{\text{ext}}\\ \mathbf{0}\\ \mathbf{0}\end{bmatrix} - \begin{bmatrix}\mathcal{R}^{\mathbf{u}}_{\text{int}}\\ \mathcal{R}^{\tilde{\mathbf{E}}}_{\text{int}}\\ \mathcal{R}^{\mathfrak{d}}_{\text{int}}\end{bmatrix} \tag{35}$$

Algorithm 1 Algorithmic implementation of the solid shell fracture with inelastic response.

1: **Input**: Given $\{\mathbf{d}_n, \boldsymbol{\varsigma}_n, \bar{\mathfrak{d}}_n, Y_n\}$, compute $\{\mathbf{d}^{(k)}_{n+1}, \boldsymbol{\varsigma}^{(k)}_{n+1}, \bar{\mathfrak{d}}^{(k)}_{n+1}, Y^{(k)}_{n+1}\}$.
2: Compute $\Delta\mathbf{d} = \mathbf{d}^{(k)}_{n+1} - \mathbf{d}_n$ and $\Delta\bar{\mathfrak{d}}^{(k)} = \bar{\mathfrak{d}}^{(k)}_{n+1} - \bar{\mathfrak{d}}_n$.
3: Loop over the integration points based on the previous converged configuration t_n
  3.1 Compute the curvilinear basis $\mathbf{G}_n$ and $\mathbf{g}_n$.
  3.2 Compute the B-operator $\mathbf{B}_n$.
  3.3 Modify the B-operator due to ANS method.
  3.4 Compute the constitutive matrix $\mathbb{C}_{\mathtt{ALG},n}$ and stress tensors $\mathbf{S}_n$ (stored as SVARS).
  3.5 Interpolate the nodal phase-field values.
  3.6 Compute the EAS-operator $\mathbf{M}_n$.
4: Compute the matrices: $\mathbf{k}_{\varsigma d,n}$, $\mathbf{k}_{\varsigma\bar{\mathfrak{d}},n}$ and $\mathbf{k}_{\varsigma\varsigma,n}$ and the internal force vector $\mathbf{R}^{\varsigma}_{\mathrm{int},n}$.
5: Compute: $\Delta\boldsymbol{\varsigma}^{(k)}_n = -\left[\mathbf{k}_{\varsigma\varsigma,n}\right]^{-1}\left[\mathbf{R}^{\varsigma}_{\mathrm{int},n} + \mathbf{k}_{\varsigma d,n}\Delta\mathbf{d}^{(k)} + \mathbf{k}_{\varsigma\mathfrak{d},n}\Delta\bar{\mathfrak{d}}^{(k)}\right]$.
6: Update the enhancing parameters: $\boldsymbol{\varsigma}^{(k)}_{n+1} = \boldsymbol{\varsigma}_n + \Delta\boldsymbol{\varsigma}^{(k)}_n$.
7: Loop over the integration points at the current tentative time step $t^{(k)}_{n+1}$
  7.1 Compute the curvilinear basis $\mathbf{G}^{(k)}_{n+1}$ and $\mathbf{g}^{(k)}_{n+1}$.
  7.2 Compute the B-operator $\mathbf{B}^{(k)}_{n+1}$.
  7.3 Modify the B-operator due to ANS method.
  7.4 Compute $\mathbf{C} := \mathbf{C}^{u} + \tilde{\mathbf{C}}$.
  7.5 Compute the total deformation gradient $\mathbf{F}$ in Cartesian coordinates.
  7.6 Compute the constitutive block: the tangent $\mathbb{C}^{(k)}_{\mathtt{ALG},n+1}$, stress tensors $\mathbf{S}^{(k)}_{n+1}$, the internal variables $Y^{(k)}_{n+1}$, and the intact free energy $\Psi^{(k)}_{n+1}$.
  7.7 Transform operators from step 7.6 to curvilinear setting.
  7.8 Interpolate the nodal phase-field values.
  7.9 Compute the EAS-operator $\mathbf{M}^{(k)}_{n+1}$.
  7.10 Compute the phase-field operators $\mathbf{B}^{\mathfrak{d}(k)}_{n+1}$.
  7.11 Compute the geometrical stiffness matrix and modify due to ANS method.
8: Construct the element matrices and the internal force vectors of the complete system.
9: Compute the static condensation of the EAS variables.
10: Perform the final assembly.

After the condensation of the assumed strains, the resulting system of algebraic equation reads

$$\begin{bmatrix}\bar{\mathbf{k}}_{dd} & \mathbf{0}\\ \mathbf{0} & \mathbf{k}_{\bar{\mathfrak{d}}\bar{\mathfrak{d}}}\end{bmatrix}\begin{bmatrix}\Delta\mathbf{d}\\ \Delta\bar{\mathfrak{d}}\end{bmatrix} = \begin{bmatrix}\mathcal{R}^{\mathbf{u}}_{\mathrm{ext}}\\ \mathbf{0}\end{bmatrix} - \begin{bmatrix}\mathcal{R}^{\bar{\mathbf{u}}}_{\mathrm{int}}\\ \mathcal{R}^{\mathfrak{d}}_{\mathrm{int}}\end{bmatrix} \tag{36}$$

where $\bar{\mathbf{k}}_{dd}$ and $\mathcal{R}^{\bar{\mathbf{u}}}_{\mathrm{int}}$ are the modified stiffness and residual computed from the static condensation as

$$\bar{\mathbf{k}}_{dd} = \mathbf{k}_{dd} - \mathbf{k}_{d\varsigma}\left[\mathbf{k}_{\varsigma\varsigma}\right]^{-1}\mathbf{k}_{\varsigma d}, \quad \mathcal{R}^{\bar{\mathbf{u}}}_{\mathrm{int}} = \mathcal{R}^{\mathbf{u}}_{\mathrm{int}} - \mathbf{k}_{d\varsigma}\left[\mathbf{k}_{\varsigma\varsigma}\right]^{-1}\mathbf{R}^{\varsigma}_{\mathrm{int}}. \tag{37}$$

3.1.2. Finite element implementation

The current computational framework is integrated into the FE code ABAQUS using the user-defined capability UEL. Throughout the solution process, we focus our attention on the algorithmic treatment within the time increment $[t_n, t^{(k)}_{n+1}]$ (with $\Delta\tau = t^{(k)}_{n+1} - t_n$), where t_n and $t^{(k)}_{n+1}$ identify the previous converged state and the prospective current time step at the global iteration k, respectively.

The point of departure in each time step are the data, $\{\mathbf{d}_n, \boldsymbol{\varsigma}_n, \bar{\mathfrak{d}}_n, Y_n\}$, where $\boldsymbol{\varsigma}_n$ are the incompatible strains stored as elements level as state-dependent variables (SVARS in ABAQUS) [50], and Y_n are the internal variables of each material model, that are stored at integration point level. Then, the nonlinear solution scheme aims at achieving equilibrium solution states at time step $n+1$, determining the corresponding values at $\{\mathbf{d}^{(k)}_{n+1}, \boldsymbol{\varsigma}^{(k)}_{n+1}, \bar{\mathfrak{d}}^{(k)}_{n+1}, Y^{(k)}_{n+1}\}$, at the element level iteration k.

The essential flowchart outlining the FE implementation is described in Algorithm 1. Furthermore, for a more comprehensive understanding, numerous listings featuring the coded subroutines responsible for executing the mentioned procedures are provided in Appendix.

We can start the description of the detailed implementation via the computation of the discretized curvilinear basis vectors, that are given by the Listing 1 corresponding to the steps 3.1 and 7.1 of such Algorithm. These basis vectors can be computed as

$$\mathbf{G}_i = \frac{\partial\mathbf{X}}{\partial\xi^i} = \approx \sum_{I=1}^{n_n} N_{I,\xi^i}(\boldsymbol{\xi})\begin{bmatrix}X_I\\ Y_I\\ Z_I\end{bmatrix}, \quad \text{with } i = 1,2,3, \tag{38}$$

$$\mathbf{g}_i = \frac{\partial \mathbf{x}}{\partial \xi^i} = \mathbf{G}_i + \frac{\partial \mathbf{u}}{\partial \xi^i} \approx \sum_{I=1}^{n_n} N_{I,\xi^i}(\boldsymbol{\xi}) \begin{bmatrix} X_I \\ Y_I \\ Z_I \end{bmatrix} + \sum_{I=1}^{n_n} N_{I,\xi^i}(\boldsymbol{\xi}) \begin{bmatrix} d_{Ix} \\ d_{Iy} \\ d_{Iz} \end{bmatrix}, \quad \text{with } i = 1,2,3, \tag{39}$$

where $N_{I,\xi^i}(\boldsymbol{\xi})$ represents the partial derivative of the shape function $N_I(\boldsymbol{\xi})$ with respect to the natural coordinate ξ^i. The computation of the displacement-strain $\mathbf{B}(\mathbf{d})$ operator is given by the partial derivative of the vectors $\mathbf{g}_i$ with respect to the displacement vector $\mathbf{d}_I$ of the node I as

$$\frac{\partial \mathbf{g}_i}{\partial \mathbf{d}_I} = \begin{bmatrix} \frac{\partial g_{ix}}{\partial \mathbf{d}_I} \\ \frac{\partial g_{iy}}{\partial \mathbf{d}_I} \\ \frac{\partial g_{iz}}{\partial \mathbf{d}_I} \end{bmatrix} = \begin{bmatrix} N_{I,\xi^i}(\boldsymbol{\xi}) & 0 & 0 \\ 0 & N_{I,\xi^i}(\boldsymbol{\xi}) & 0 \\ 0 & 0 & N_{I,\xi^i}(\boldsymbol{\xi}) \end{bmatrix}, \quad \text{with } i = 1,2,3 \text{ and } I = 1,\dots,n_n. \tag{40}$$

Then, the column entries of the strain–displacement operator $\mathbf{B}_I(\mathbf{d})$ of the node I can be expressed as (see the Listing 2 corresponding to steps 3.2 and 7.2 of Algorithm 1):

$$\mathbf{B}_I(\mathbf{d}) = \frac{\partial \bar{\mathbf{E}}}{\partial \mathbf{d}_I} = \begin{bmatrix} \frac{\partial E^u_{11}}{\partial \mathbf{d}_I} \\ \frac{\partial E^u_{22}}{\partial \mathbf{d}_I} \\ \frac{\partial E^u_{33}}{\partial \mathbf{d}_I} \\ 2\frac{\partial E^u_{12}}{\partial \mathbf{d}_I} \\ 2\frac{\partial E^u_{13}}{\partial \mathbf{d}_I} \\ 2\frac{\partial E^u_{23}}{\partial \mathbf{d}_I} \end{bmatrix} = \begin{bmatrix} \mathbf{g}_1^{\mathrm{T}} \frac{\partial \mathbf{g}_1}{\partial \mathbf{d}_I} \\ \mathbf{g}_2^{\mathrm{T}} \frac{\partial \mathbf{g}_2}{\partial \mathbf{d}_I} \\ \mathbf{g}_3^{\mathrm{T}} \frac{\partial \mathbf{g}_3}{\partial \mathbf{d}_I} \\ \mathbf{g}_1^{\mathrm{T}} \frac{\partial \mathbf{g}_2}{\partial \mathbf{d}_I} + \mathbf{g}_2^{\mathrm{T}} \frac{\partial \mathbf{g}_1}{\partial \mathbf{d}_I} \\ \mathbf{g}_1^{\mathrm{T}} \frac{\partial \mathbf{g}_3}{\partial \mathbf{d}_I} + \mathbf{g}_3^{\mathrm{T}} \frac{\partial \mathbf{g}_1}{\partial \mathbf{d}_I} \\ \mathbf{g}_2^{\mathrm{T}} \frac{\partial \mathbf{g}_3}{\partial \mathbf{d}_I} + \mathbf{g}_3^{\mathrm{T}} \frac{\partial \mathbf{g}_2}{\partial \mathbf{d}_I} \end{bmatrix} = \begin{bmatrix} \mathbf{g}_1^{\mathrm{T}} N_{I,\xi^1} \\ \mathbf{g}_2^{\mathrm{T}} N_{I,\xi^2} \\ \mathbf{g}_3^{\mathrm{T}} N_{I,\xi^3} \\ \mathbf{g}_1^{\mathrm{T}} N_{I,\xi^2} + \mathbf{g}_2^{\mathrm{T}} N_{I,\xi^1} \\ \mathbf{g}_1^{\mathrm{T}} N_{I,\xi^3} + \mathbf{g}_3^{\mathrm{T}} N_{I,\xi^1} \\ \mathbf{g}_2^{\mathrm{T}} N_{I,\xi^3} + \mathbf{g}_3^{\mathrm{T}} N_{I,\xi^2} \end{bmatrix}. \tag{41}$$

It is noteworthy that the previous operators should be accordingly modified through the use of the ANS method (if activated), first, for alleviating trapezoidal locking, following Eq. (17) as (see Listing 3):

$$\mathbf{B}_I^{\mathrm{ANS,trap}}(\mathbf{d}, \tilde{\mathbf{E}}) = \begin{bmatrix} \mathbf{g}_1^{\mathrm{T}} N_{I,\xi^1} \\ \mathbf{g}_2^{\mathrm{T}} N_{I,\xi^2} \\ \mathbf{g}_3^{\mathrm{T}} N_{I,\xi^3} + \sum_{m=1}^{4} \mathbf{g}_{3,m}^{\mathrm{T}} N^m N_{I,m,\xi^3} \\ \mathbf{g}_1^{\mathrm{T}} N_{I,\xi^2} + \mathbf{g}_2^{\mathrm{T}} N_{I,\xi^1} \\ \mathbf{g}_1^{\mathrm{T}} N_{I,\xi^3} + \mathbf{g}_3^{\mathrm{T}} N_{I,\xi^1} \\ \mathbf{g}_2^{\mathrm{T}} N_{I,\xi^3} + \mathbf{g}_3^{\mathrm{T}} N_{I,\xi^2} \end{bmatrix}, \tag{42}$$

and, then, for shear locking, the B-operator is modified according to Eq. (16) as (see Listing 4):

$$\mathbf{B}_I^{\mathrm{ANS,shear}}(\mathbf{d}, \tilde{\mathbf{E}}) = \begin{bmatrix} \mathbf{g}_1^{\mathrm{T}} N_{I,\xi^1} \\ \mathbf{g}_2^{\mathrm{T}} N_{I,\xi^2} \\ \mathbf{g}_3^{\mathrm{T}} N_{I,\xi^3} \\ \mathbf{g}_1^{\mathrm{T}} N_{I,\xi^2} + \mathbf{g}_2^{\mathrm{T}} N_{I,\xi^1} \\ \mathbf{g}_1^{\mathrm{T}} N_{I,\xi^3} + \mathbf{g}_3^{\mathrm{T}} N_{I,\xi^1} + \frac{1}{2} N^A (\mathbf{g}_{1,A}^{\mathrm{T}} N_{I,A,\xi^3} + \mathbf{g}_{3,A}^{\mathrm{T}} N_{I,A,\xi^1}) + \frac{1}{2} N^B (\mathbf{g}_{1,B}^{\mathrm{T}} N_{I,B,\xi^3} + \mathbf{g}_{3,B}^{\mathrm{T}} N_{I,B,\xi^1}) \\ \mathbf{g}_2^{\mathrm{T}} N_{I,\xi^3} + \mathbf{g}_3^{\mathrm{T}} N_{I,\xi^2} + \frac{1}{2} N^C (\mathbf{g}_{2,C}^{\mathrm{T}} N_{I,C,\xi^3} + \mathbf{g}_{3,C}^{\mathrm{T}} N_{I,C,\xi^2}) + \frac{1}{2} N^D (\mathbf{g}_{2,D}^{\mathrm{T}} N_{I,D,\xi^3} + \mathbf{g}_{3,D}^{\mathrm{T}} N_{I,D,\xi^2}) \end{bmatrix}. \tag{43}$$

Listings 3 and 4 correspond to the Steps 3.3 and 7.3 of Algorithm 1. The following step is the computation of the enhanced counterpart of the right Cauchy–Green tensor $\tilde{\mathbf{C}}$, done through the Green–Lagrange enhanced strain tensor $\tilde{\mathbf{E}}$. For this, the $\mathbf{M}(\xi)$ tensor is assembled following the seven modes proposed by Vu-Quoc and Tan [47]. They are defined in the isoparametric space as:

$$\mathbf{M}(\xi) = \begin{bmatrix} \xi^1 & 0 & 0 & 0 & 0 & 0 & 0 \\ 0 & \xi^2 & 0 & 0 & 0 & 0 & 0 \\ 0 & 0 & \xi^3 & \xi^1\xi^3 & \xi^2\xi^3 & 0 & 0 \\ 0 & 0 & 0 & 0 & 0 & \xi^1 & \xi^2 \\ 0 & 0 & 0 & 0 & 0 & 0 & 0 \\ 0 & 0 & 0 & 0 & 0 & 0 & 0 \end{bmatrix} \tag{44}$$

Then, the enhancing counterpart $\tilde{\mathbf{E}}$ is assembled following Eq. (14), see Listing 7. This information comes in handy in step 7.4 of Algorithm 1 to compute right Cauchy–Green tensor as Eq. (15) states.

The next procedure shall be the computation of the stress tensors, the constitutive matrix and the intact free energy density combined with the phase-field approach. First, we assemble the deformation gradient $\mathbf{F}$ in Cartesian coordinates (step 7.5), which basically consists in following Eq. (5), but by using the second identity tensor $\mathbf{I}$ instead of $\mathbf{G}$. Then, we compute the constitutive material law (step 3.4 and 7.6) and since three different inelastic models are being presented in this work, further details regarding the implementation is detailed in subsequent Sections 3.2–3.4. However, it is noteworthy to mention the conversion of this magnitudes from cartesian to curvilinear coordinates, which corresponds to step 7.7 (Listing 5) and is required for the FE computation of the solid shells:

$$\mathbf{S} = S_{ij}\mathbf{G}^i \otimes \mathbf{G}^j \tag{45}$$

$$\mathbb{C} = C_{ijkl}\mathbf{G}^i \otimes \mathbf{G}^j \otimes \mathbf{G}^k \otimes \mathbf{G}^l \tag{46}$$

At last, the geometric part of the stiffness matrix at the element level requires the computation of the derivative of the B-operator with respect to the kinematic field in order to compute (step 7.11 of Algorithm 1) $\mathbf{S} : \Delta\delta\mathbf{E}^u$, where $\Delta\delta\mathbf{E}^u$ stands for the linearized virtual strains (see Listing 8):

$$\mathbf{S} : \Delta\delta\mathbf{E}^u = \delta\mathbf{d}\left[\left[\frac{\partial\mathbf{B}(\mathbf{d})}{\partial\mathbf{d}}\right]^{\mathrm{T}}\mathbf{S}\right]\Delta\mathbf{d} = \sum_{I=1}^{n_n}\sum_{K=1}^{n_n}\delta\mathbf{d}_I^{\mathrm{T}}\mathcal{H}_{IK}\Delta\mathbf{d}_K^{\mathrm{T}}, \tag{47}$$

where

$$\begin{aligned}\mathcal{H}_{IK} = {} & S^{11}N_{I,\xi^1}N_{K,\xi^1} + S^{22}N_{I,\xi^2}N_{K,\xi^2} + S^{33}N_{I,\xi^3}N_{K,\xi^3} + S^{12}\left(N_{I,\xi^1}N_{K,\xi^2} + N_{I,\xi^2}N_{K,\xi^1}\right) + \\ & S^{13}\left(N_{I,\xi^1}N_{K,\xi^3} + N_{I,\xi^3}N_{K,\xi^1}\right) + S^{23}\left(N_{I,\xi^2}N_{K,\xi^3} + N_{I,\xi^3}N_{K,\xi^2}\right).\end{aligned} \tag{48}$$

If ANS is present, Eq. (48) has to be modified accordingly (Listing 9). First, if the ANS contribution for trapezoidal locking alleviation is activated, following Eq. (17), the modification reads:

$$\begin{aligned}\mathcal{H}_{IK} = {} & S^{11}N_{I,\xi^1}N_{K,\xi^1} + S^{22}N_{I,\xi^2}N_{K,\xi^2} + S^{33}\sum_{m=1}^{4}N^m N_{I,m,\xi^3}N_{K,m,\xi^3} \\ & + S^{12}\left(N_{I,\xi^1}N_{K,\xi^2} + N_{I,\xi^2}N_{K,\xi^1}\right) + S^{13}\left(N_{I,\xi^1}N_{K,\xi^3} + N_{I,\xi^3}N_{K,\xi^1}\right) + S^{23}\left(N_{I,\xi^2}N_{K,\xi^3} + N_{I,\xi^3}N_{K,\xi^2}\right).\end{aligned} \tag{49}$$

whereas for tackling shear locking, the expression is modified according to Eq. (16):

$$\begin{aligned}\mathcal{H}_{IK} = {} & S^{11}N_{I,\xi^1}N_{K,\xi^1} + S^{22}N_{I,\xi^2}N_{K,\xi^2} + S^{33}N_{I,\xi^3}N_{K,\xi^3} + S^{12}\left(N_{I,\xi^1}N_{K,\xi^2} + N_{I,\xi^2}N_{K,\xi^1}\right) + \\ & S^{13}\left[\frac{1}{2}N^A(N_{I,A,\xi^2}N_{K,A,\xi^3} + N_{I,A,\xi^3}N_{K,A,\xi^2}) + \frac{1}{2}N^B(N_{I,B,\xi^2}N_{K,B,\xi^3} + N_{I,B,\xi^3}N_{K,B,\xi^2})\right] + \\ & S^{23}\left[\frac{1}{2}N^C(N_{I,C,\xi^2}N_{K,C,\xi^3} + N_{I,C,\xi^3}N_{K,C,\xi^2}) + \frac{1}{2}N^D(N_{I,D,\xi^2}N_{K,D,\xi^3} + N_{I,D,\xi^3}N_{K,D,\xi^2})\right].\end{aligned} \tag{50}$$

With this, we can construct the element matrices and the internal force vectors (step 8 of Algorithm 1) which are present in the system of equations presented in Eq. (35). The final assembly is constructed by applying the static condensation (step 9 of Algorithm 1), thus reaching Eq. (36).

We have postulated all the basic ingredients to synthesize our material formulation for the FE code of ABAQUS. Now, we delve into the particularities of each of the material models considered.

3.2. Phase-field fracture for hyperplasticity

According to Borden et al. [13], capturing the ductile fracture within the context of the phase-field approach of fracture is conducted via the decomposition of the free energy function of Helmholtz Ψ into elastic Ψ^{elas} and plastic contributions Ψ^{plas}. Therefore, the functional given in Eq. (18) takes the form

$$\Pi(\mathbf{C}, \tilde{\mathbf{C}}, Y, \mathfrak{d}) = \int_{\Omega_0}\left[g(\mathfrak{d})\Psi_+^{\mathrm{elas}}(\mathbf{C}, \mathbf{C}^p) + \Psi_-^{\mathrm{elas}}(\mathbf{C}, \mathbf{C}^p) + g(\mathfrak{d})\Psi^{\mathrm{plas}}(Y)\right]\mathrm{d}\Omega + \int_{\Omega_0}\mathcal{G}_C\left[\frac{\mathfrak{d}^2}{2\ell} + \frac{\ell}{2}|\nabla\mathfrak{d}|^2\right]\mathrm{d}\Omega, \tag{51}$$

where Y is a set of plastic variables containing $\mathbf{C}^p$, where $\mathbf{C} = \mathbf{F}^{\mathrm{T}} \cdot \mathbf{F}$, and $\mathbf{C}^p = (\mathbf{F}^p)^{\mathrm{T}} \cdot \mathbf{F}^p$ are the right Cauchy–Green deformation tensor and the plastic contributions, respectively. We use the same degradation function $g(\mathfrak{d})$ for the elastic and plastic parts. In this concern, plastic energy threshold is ruled a bit different as in [13] assuming a total energetic threshold Ψ_0 instead of an only plastic threshold as in the referential work, using the operator $\langle \Psi - \Psi_0 \rangle$ defined as

$$\langle \Psi - \Psi_0 \rangle = \begin{cases} 0 & \text{if } (\Psi - \Psi_0) < 0 \\ \Psi - \Psi_0 & \text{if } (\Psi - \Psi_0) > 0 \end{cases} \tag{52}$$

For the sake of clarity, we rephrase the total energy functional given in Eq. (51) as

$$\Pi(\mathbf{C}, \mathbf{C}^p, Y, \mathfrak{d}) = \int_{\Omega_0} \langle \Psi(\mathbf{C}, \mathbf{C}^p, Y, \mathfrak{d}) - \Psi_0 \rangle \, \mathrm{d}\Omega + \int_{\Omega_0} \mathcal{G}_C \left[\frac{\mathfrak{d}^2}{2\ell} + \frac{\ell}{2} |\nabla \mathfrak{d}|^2 \right] \, \mathrm{d}\Omega, \tag{53}$$

with

$$\Psi(\mathbf{C}, \mathbf{C}^p, Y, \mathfrak{d}) = g(\mathfrak{d}) \Psi_+^{\mathrm{elas}}(\mathbf{C}, \mathbf{C}^p) + \Psi_-^{\mathrm{elas}}(\mathbf{C}^e, \mathbf{C}^p) + g(\mathfrak{d}) \Psi^{\mathrm{plas}}(Y). \tag{54}$$

The hyperelastic constitutive model which ruling the elastic response prior plastic evolution is defined based upon a volumetric-deviatoric decomposition introduced by Amor et al. [4], which considers the tensile and compressive contributions in the strain energy function as

$$\Psi_+^{\mathrm{elas}} = \begin{cases} U(J) + \bar{\Psi}(\bar{\mathbf{C}}, \mathbf{C}^p) & \text{if } J \geq 1 \\ \bar{\Psi}(\bar{\mathbf{C}}, \mathbf{C}^p) & \text{if } J < 1 \end{cases}; \qquad \Psi_-^{\mathrm{elas}} = \begin{cases} 0 & \text{if } J \geq 1 \\ U(J) & \text{if } J < 1 \end{cases} \tag{55}$$

In the previous expression $U(J)$ and $\bar{\Psi}(\bar{\mathbf{C}}, \mathbf{C}^p)$ stand for the volumetric and isochoric additive contributions to the strain energy density, $J = \det \mathbf{F}^e$, and $\bar{\mathbf{C}} = J^{e-2/3}\mathbf{C}$. In line with Eq. (54), only the tensile contributions contribute to the crack growth. Both volumetric and isochoric contributions use the specific forms

$$U(J) = \frac{1}{2}\kappa \left[\frac{1}{2}(J^2 - 1) - \ln J \right]; \qquad \bar{\Psi}(\bar{\mathbf{C}}, \mathbf{C}^p) = \frac{1}{2}\mu(\bar{\mathbf{C}} : \mathbf{C}^{p-1} - 3), \tag{56}$$

where κ and μ are the volumetric and shear modulus, respectively. Second Piola–Kirchhoff stress can be easily obtained as

$$\mathbf{S} = \mu(J)^{2/3} \left[\mathbf{C}^{p-1} - \frac{1}{3}(\mathbf{C} : \mathbf{C}^{p-1})\mathbf{C}^{-1} \right] + \frac{1}{2}\kappa((J)^2 - 1)\mathbf{C}^{-1}. \tag{57}$$

It can be observed that an hybrid approach is being used, where only split in the strain energy is considered, but not within the stresses.

The plastic response obeys a standard J_2 flow theory associative elastoplastic constitutive model with isotropic hardening. Considering that the flow is isochoric, the Jacobian for the plastic part takes the form

$$\det \mathbf{F}^p = 1 \rightarrow J = \det \mathbf{F}^e. \tag{58}$$

Moreover, the standard yield function J_2 is given by

$$f(\boldsymbol{\tau}, \alpha) = ||\mathbf{s}|| - \sqrt{\frac{2}{3}} k(\alpha); \quad \mathbf{s} = \mathrm{dev}[\boldsymbol{\tau}], \tag{59}$$

where α is the hardening parameter, $k(\alpha)$ is the isotropic hardening modulus, and $\boldsymbol{\tau}$ is the Kirchhoff stress. The function has to be adapted for a phase-field approach for ductile fracture as the deformation is dominated by plastic strain. Therefore, the degradation function is added to the yield surface as

$$f(\boldsymbol{\tau}, \alpha, \mathfrak{d}) = ||\mathbf{s}|| - g(\mathfrak{d}) \sqrt{\frac{2}{3}} k(\alpha), \tag{60}$$

representing shrinkage in the yield surface as the damage progress. The hardening law can be introduced using the choice $k(\alpha)$. For example,

$$k(\alpha) = \begin{cases} \sigma_y & \text{Perfect plasticity} \\ \sigma_y + K\alpha & \text{Linear isotropic hardening} \end{cases} \tag{61}$$

where σ_y is the yield stress and K is the linear hardening coefficient. The flow rule postulated by [51] is adopted which states that under maximum plastic dissipation, the flow rule reads

$$\mathrm{dev}[\mathcal{L}_v \mathbf{b}^e] = -\frac{2}{3}\dot{\gamma}\,\mathrm{tr}[\mathbf{b}^e] \frac{\mathbf{s}}{||\mathbf{s}||}, \tag{62}$$

where $\mathbf{b}^e = \mathbf{F}^e \cdot \mathbf{F}^{eT}$ is the elastic left Cauchy–Green tensor, $\mathcal{L}_v[\bullet]$ is the Lie derivative operator, $\dot{\gamma}$ is the Lagrange plastic multiplier from the minimization problem, and $\mathrm{dev}[\bullet]$ is the deviatoric operator in the current configuration that reads $\mathrm{dev}[\bullet] = \bullet - \frac{1}{3}\mathrm{tr}[\bullet]\mathbf{I}$, with $\mathrm{tr}[\bullet]$ being the trace operator. Eq. (62) only determines the isochoric part of $\mathrm{dev}[\mathcal{L}_v \mathbf{b}^e]$, meaning that the spherical part of such tensor is determined by the isochoric contribution, i.e., $\det \mathbf{b}^e = J^2$.

In line with Borden et al. [13], two approaches to compute the effective plastic work are considered, one based on stress triaxiality, and one without. The first approach is postulated in absence of stress triaxiality effects, and the rate of the plastic strain energy density reads

$$\boxed{\dot{\Psi}_{\text{plas}} = \dot{\gamma}\,||\mathbf{s}||,} \tag{63}$$

which tells no extra information regarding the state of stress.

For the second approach, that include triaxility effects, we refer [52–54] and the Gurson-Tvergaard-Needleman (GTN) model [55, 56], that establishes the failure of ductile materials as a combination of effective plastic strain and the level of stress triaxiality. Following [13], Eq. (63) can be modified to include the stress triaxiality as

$$\boxed{\dot{\Psi}_{\text{plas}} = \dot{\gamma}\,\frac{||\mathbf{s}||}{\psi},} \tag{64}$$

where ψ is a dimensionless parameter that accounts for stress triaxiality, expressed as

$$\psi = d_1 + d_2 \exp\left[d_3 \frac{\tau_m}{||\mathbf{s}||}\right]; \quad \tau_m = \frac{\text{tr}[\boldsymbol{\tau}]}{3}, \tag{65}$$

where d_1, d_2 and d_3 are dimensionless coefficients. In the sequel, both Eqs. (63) and (64) can be considered as possible candidates to account for the plastic work affecting the crack growth.

With regard to the algorithmic treatment, following Eq. (60), in order to update the plastic flow, the updated configuration at time t_{n+1} must fulfill the Karush-Kuhn-Tucker (KKT) conditions, which reads

$$f(\tau_{n+1}, \alpha_{n+1}) \leq 0; \quad \Delta\gamma \geq 0; \quad \Delta\gamma\, f(\tau_{n+1}, \alpha_{n+1}) = 0. \tag{66}$$

Here the Kirchhoff stress is updated as $\boldsymbol{\tau}_{n+1} = g(\mathfrak{d})[\mu\ \text{dev}[\bar{\mathbf{b}}^e_{n+1}] + \text{tr}[\boldsymbol{\tau}_n]\mathbf{I}]$, and $\Delta\gamma = \gamma_{n+1} - \gamma_n$. For each time increment, we calculate an elastic predictor on $\bar{\mathbf{b}}^e_{n+1}$ whose particular expression takes the form

$$\bar{\mathbf{b}}^{\text{e trial}}_{n+1} = \bar{\mathbf{f}}_{n+1}\bar{\mathbf{b}}^e_n\bar{\mathbf{f}}^{\text{T}}_{n+1}; \quad \bar{\mathbf{f}}_{n+1} = \det[\mathbf{f}_{n+1}]^{-1/3}\mathbf{f}_{n+1}; \quad \mathbf{f}_{n+1} = \mathbf{I} + \nabla_{x_n}\mathbf{u}_n. \tag{67}$$

with update of the hardening parameter as

$$\alpha_{n+1} = \alpha_n. \tag{68}$$

If the trial state satisfies the discrete KKT conditions, then it is accepted as the updated configuration. If they are not satisfied, the trial state is dismissed and the configuration is updated according to the following flow and hardening laws

$$\text{dev}[\bar{\mathbf{b}}^e_{n+1}] = \text{dev}[\bar{\mathbf{b}}^{e\ \text{trial}}_{n+1}] - \frac{2}{3}\Delta\gamma\,\text{tr}[\bar{\mathbf{b}}^e_{n+1}]\mathbf{n}_{n+1}; \quad \mathbf{n}_{n+1} = \frac{\mathbf{s}_{n+1}}{||\mathbf{s}_{n+1}||}, \tag{69}$$

$$\alpha_{n+1} = \alpha_n + \sqrt{\frac{2}{3}}\Delta\gamma. \tag{70}$$

This update leads to the algorithm that we plot in Algorithm 2, that closely follows [13]. For the computation of an UEL subroutine updated Lagrangian approach, Cauchy stress can be obtained using Kirchhoff stress using the transformation $\boldsymbol{\sigma} = J^{-1}\boldsymbol{\tau}$, and the Jacobian tangent matrix $\mathbb{C}_{\text{ALG}}$ can be obtained numerically.

3.3. Phase-field fracture for visco-hyperelasticity

Concerning the constitutive formulation for the visco-hyperelastic material, we adopt the model adopted in Valverde-González et al. [43] based on the particular approach from Linder et al. [42]. This formulation relies on the consideration of the microstructure as highly mobile and flexible macro-molecules behaving as idealized polymer networks, thus leading to the constitutive behavior of rubber viscoelasticity. The network consists of macromolecules of polymer being strongly cross-linked with a sub-network of highly mobile and temporary entanglement mechanisms. The elastic response is due to the cross-linking, whereas the viscoelastic behavior is caused by the subnetwork. This Maxwellian rheological system is represented in Fig. 3(a). Its material response can be defined based on a hyper-viscoelastic decomposition following the distinction between tensile and compressive states that Eq. (18) postulates. With the arguments and the system presented in the previous Section, the Helmholtz free energy function Ψ for the visco-hyperelastic problem is postulated as

$$\Psi(\mathbf{C}, \mathbf{A}, J) = \Psi^{\text{elas}}(\mathbf{C}, J) + \sum_{\gamma=1}^{\text{n}} \Psi^{\text{visco},\gamma}(\mathbf{C}, \mathbf{A}). \tag{83}$$

Here the total strain Ψ is divided into two terms: (i) Ψ^{elas}, dedicated to the hyperelastic constitutive part and (ii) $\Psi^{\text{visco},\gamma}$, dedicated to every γ viscous branch. In addition to both terms, n makes reference to the number of viscous terms contained within

Algorithm 2 Algorithmic box for the return-mapping J_2 plastic flow algorithm adapted from [13].

1: **Input**: $\mathbf{F}_{n+1}$, $\mathbf{F}_n$, $\bar{\mathbf{b}}^e_n$, α_n.

2: Compute the damaged elastic predictor

$$\mathbf{f}_{n+1} = \mathbf{F}_{n+1} \cdot \mathbf{F}_n^{-1}; \quad \bar{\mathbf{f}}_{n+1} = \det[\mathbf{f}_{n+1}]^{-1/3}\mathbf{f}_{n+1}; \quad \bar{\mathbf{b}}^{e\text{trial}}_{n+1} = \bar{\mathbf{f}}_{n+1}\bar{\mathbf{b}}^e_n\bar{\mathbf{f}}^{\mathrm{T}}_{n+1} \tag{71}$$

$$\boxed{\mathbf{s}^{\text{trial}}_{n+1} = g(\mathfrak{d})\mu\ \mathrm{dev}[\bar{\mathbf{b}}^{\text{e trial}}_{n+1}]}. \tag{72}$$

3: Compute plastic loading

$$\boxed{f^{\text{trial}}_{n+1} = ||\mathbf{s}^{\text{trial}}_{n+1}|| - g(\mathfrak{d})\sqrt{\frac{2}{3}}k(\alpha_n).} \tag{73}$$

If Eq. 73 ≤ 0, exit algorithm. Otherwise, go to Step 4.

4: Return-mapping algorithm

$$\bar{I}^{e\ \text{trial}}_{n+1} = \frac{1}{3}\mathrm{tr}[\bar{\mathbf{b}}^{e\ \text{trial}}_{n+1}]; \quad \bar{\mu} = g(\mathfrak{d})\mu\bar{I}^{e\ \text{trial}}_{n+1}. \tag{74}$$

Solve the following equation to obtain the increment in the Lagrange multiplier

$$\boxed{\hat{f}(\Delta\gamma) = \frac{f^{\text{trial}}_{n+1}}{2\bar{\mu} + \frac{2}{3}g(\mathfrak{d})K}.} \tag{75}$$

Update the stress and hardening coefficient as

$$\mathbf{s}_{n+1} = \mathbf{s}^{\text{trial}}_{n+1} - 2\bar{\mu}\Delta\gamma\mathbf{n}, \tag{76}$$

$$\alpha_{n+1} = \alpha_n + \sqrt{\frac{2}{3}}\Delta\gamma. \tag{77}$$

5: Compute Kirchhoff stress

$$J_{n+1} = \det\mathbf{F}_{n+1}; \quad p_{n+1} = \frac{1}{2}g(\mathfrak{d})\kappa\Big(J_{n+1} - \frac{1}{J_{n+1}}\Big), \tag{78}$$

$$\boxed{\boldsymbol{\tau}_{n+1} = \mathbf{s}_{n+1} + J_{n+1}p_{n+1}\mathbf{I}.} \tag{79}$$

6: Find $\bar{I}^e_{n+1}$ and update the intermediate configuration

$$\boxed{\det\left[\frac{\mathbf{s}_{n+1}}{g(\mathfrak{d})\mu}\right] + \bar{I}^e_{n+1}\mathbf{I} = 1} \rightarrow \bar{\mathbf{b}}^e_{n+1} = \mathrm{dev}[\bar{\mathbf{b}}^e_{n+1}] + \bar{I}^e_{n+1}\mathbf{I}. \tag{80}$$

7: Compute energies: due to updated Lagrangian, the terms for Ψ^{elas} and Ψ^{plas} read as

$$\Psi^{\text{elas}}_{+} = \begin{cases} U(J) + \frac{1}{2}\mu(\mathrm{tr}[\bar{\mathbf{b}}^e] - 3) & \text{if } J \geq 1 \\ \frac{1}{2}\mu(\mathrm{tr}[\bar{\mathbf{b}}^e] - 3) & \text{if } J < 1 \end{cases} \quad \Psi^{\text{elas}}_{-} = \begin{cases} 0 & \text{if } J \geq 1 \\ U(J) & \text{if } J < 1 \end{cases} \tag{81}$$

$$\text{Without triaxiality: } \dot{\Psi}^{\text{plas}} = \dot{\gamma}||\mathbf{s}||; \quad \text{With triaxiality: } \dot{\Psi}^{\text{plas}} = \dot{\gamma}\frac{||\mathbf{s}||}{\psi}. \tag{82}$$

the rheological model, and $\mathbf{A}$ here is the macroscopical tensor that accounts for the microscopical stretches λ in the system of polymer chains.

Reflecting first the hyperelastic term, we highlight that is split into the corresponding volumetric ($U(J)$) and isochoric ($\bar{\Psi}$) contributions specialized to a standard neo-Hookean approach

$$\Psi^{\text{elas}}(\mathbf{C}, J) = \bar{\Psi} + U(J); \quad \bar{\Psi} = \frac{\mu}{2}(\bar{I}_1 - 3), \quad U(J) = \frac{\kappa}{2}(J-1)^2. \tag{84}$$

where $\bar{I}_1$ is the first deviatoric invariant $\bar{I}_1 = \mathrm{tr}[\bar{\mathbf{C}}] = J^{-2/3}\mathrm{tr}\mathbf{C}$.

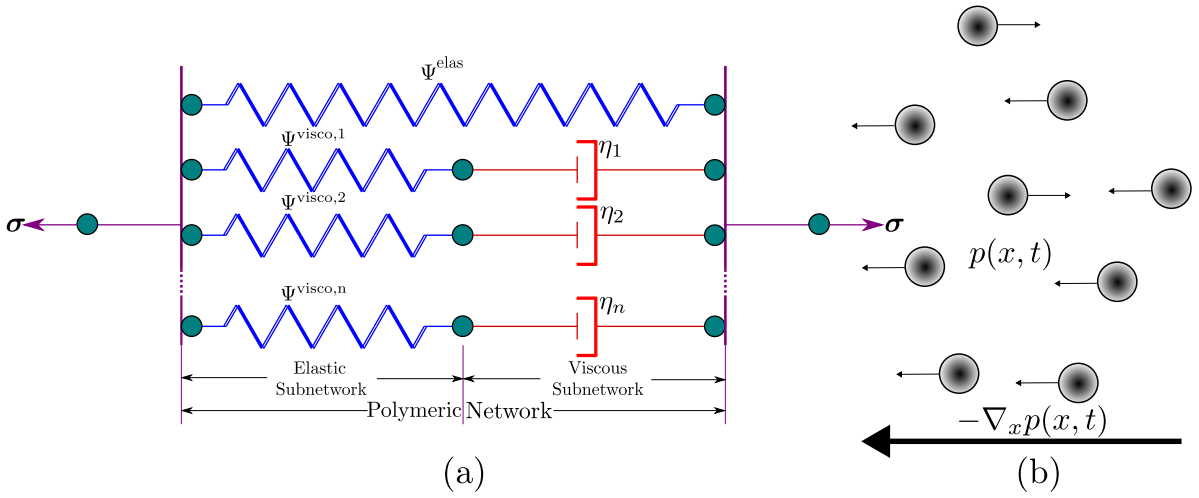

Fig. 3. (a) Maxwellian rheological model of the response of the material consisting of the elastic branches, representing the strongly cross-linked network, and the viscous branches, representing the highly mobile with entanglements subnetwork. (b) Brownian motion of non-interacting point particles submerged in a viscous medium, which serves as the starting microscopic point to synthetize the macroscopic visco-hyperelasticity theory.

For the viscoelastic part of the model, a contribution built from the Brownian particle movement is considered, see Fig. 3(b), considering the probability $p(x,t)$ of finding a particle in a certain state governed by its position x at a certain time t. Such contribution is embedded into the framework of continuous rubber viscoelasticity by considering those particles as polymer chains and by defining the probability function based on the stretch state λ rather than the position as $p(\lambda,t)$. From this definition, we can trace the evolution of a stretch space $\mathcal{L}_{\mathbf{x}}$ connected locally to a material point with position $\mathbf{x}$ in the current configuration $\Omega_t \subset \mathbb{R}^n$ and map its evolution from the initial stretch space $\mathcal{L}_{\mathbf{X}}$, linked to a material point with position $\mathbf{X}$ in the reference configuration $\Omega_0 \subset \mathbb{R}^n$, by means of the microdeformation map $\bar{\mathbf{P}}$. For further details on the implementation of the microscopic model, the reader is referred to [42]. Recalling this constitutive model, via the definition of $\bar{\mathbf{P}}$, it is possible to account for the micromechanics of the system by defining in Eq. (85)

$$\bar{\mathbf{P}} = \bar{\mathbf{F}} \cdot \bar{\mathbf{P}}_{\mathbf{X}}, \tag{85}$$

where $\bar{\mathbf{P}}_{\mathbf{X}}$ stands for the pre-deformation map tensor. The definition for the tensor accounting the stretch state $\mathbf{A}$ is reached after performing some operations in Eq. (85) reads

$$\mathbf{A} = \bar{\mathbf{P}}_{\mathbf{X}} \cdot \bar{\mathbf{P}}_{\mathbf{X}}^{\mathrm{T}}. \tag{86}$$

Considering that the tensor $\mathbf{A}$ provides the information concerning the microdeformation of the visco-elastic subnetwork in the initial configuration and it depends on macroscopic variables, the time evolution can be computed as

$$\dot{\mathbf{A}} = \frac{1}{\tau^{\gamma}}(\bar{\mathbf{C}}^{-1} - \mathbf{A}), \tag{87}$$

where τ^{γ} is the relaxation time associated to the viscous mechanism γ. Based on this definitions, we reach the expression for the viscous additional term in the Helmholtz free energy Ψ^{visco} as

$$\Psi^{\text{visco},\gamma}(\mathbf{C},\mathbf{A}) = \frac{1}{2}\mu^{\text{visco},\gamma}[(\mathbf{A}^{(\gamma)} : \bar{\mathbf{C}}) - \ln(\det\mathbf{A}^{(\gamma)})]. \tag{88}$$

With $\mu^{\text{visco},\gamma}$ being the viscous shear modulus for each mechanism γ.

We propose a formulation for visco-hyperelasticity where crack growth only accounts while in a tension state. Therefore, following Eq. (18), we decompose the elastic strain energy density Ψ to distinguish between tensile Ψ_+ and compressive states Ψ_-. For this, we employ again the isochoric-volumetric decomposition of Amor and co-authors [4], that is adopted as

$$\Psi_+(\mathbf{C},\mathbf{A},J) = \begin{cases} \Psi^{\text{elas}}(\mathbf{C}) + \sum_{\gamma=1}^{\text{n}} \Psi^{\text{visco},\gamma}(\mathbf{C},\mathbf{A}) & \text{if } J \geq 1 \\ \bar{\Psi}(\mathbf{C}) + \sum_{\gamma=1}^{\text{n}} \Psi^{\text{visco},\gamma}(\mathbf{C},\mathbf{A}) & \text{if } J < 1 \end{cases} \tag{89}$$

$$\Psi_-(J) = \begin{cases} 0 & \text{if } J \geq 1 \\ U(J) & \text{if } J < 1 \end{cases} \tag{90}$$

The expression for the second Piola–Kirchhoff stress rightfully obtained from the free Helmholtz energy reads

$$\mathbf{S} := \mu\left(J^{-2/3}\mathbf{I} - \frac{\bar{I}_1}{3}\mathbf{C}^{-1}\right) + \kappa J(J-1)\mathbf{C}^{-1} + J^{-2/3}\mathbb{P} : \left(\mu^{\text{visco},\alpha}\mathbf{A}^{(\gamma)}\right), \tag{91}$$

where $\mathbb{P}$ is the fourth-order projector operator whose particular expression takes the form

$$\mathbb{P} : (\bullet) = \bullet - \frac{1}{3}[(\bullet) : \mathbf{C}]\mathbf{C}^{-1}. \tag{92}$$

Finally, a numerical tangent $\mathbb{C}_{\text{ALG}}$ is computed for the completion of the current material model.

3.4. Phase-field fracture for visco-hyperplasticity

With the aim of the visco-hyperplastic formulation, we modify the return-mapping algorithm presented in Section 3.2 to consider test rate dependence that affects the plastic regime of the sample. Modeling hyperelastic–viscoplastic behavior requires some modifications in the original hyperplasticity formulation to be performed:

- Though we make a distinction between compressive and tensile stresses as stated in Eqs. (53)–(54), for the numerics, we use Kirchhoff-Saint Venant isotropic material, whose derivations and implementations are presented in [35,36,41] which can easily incorporate the dependence of testing rate in the return mapping algorithm.
- We utilize Mandel stress instead of the deviatoric part of the Kirchhoff stress for the elastic predictor, see Eq. (59).

For the Kirchhoff-Saint Venant isotropic material, the Helmholtz free energy function follows

$$\Psi(\mathbf{E}) = \frac{1}{2}\lambda(\text{tr}[\mathbf{E}])^2 + \mu\text{tr}[\mathbf{E}^2]. \tag{93}$$

Upon considering $\mathbf{E}$ dependency on the Eq. (93), the expression for the second Piola–Kirchhoff stress $\mathbf{S}$ reads

$$\mathbf{S} = \lambda(\text{tr}[\mathbf{E}])\mathbf{I} + 2\mu\mathbf{E}. \tag{94}$$

Due to the visco-plasticity, total deformation gradient $\mathbf{F}$ can be decomposed into elastic and plastic parts as $\mathbf{F} = \mathbf{F}^e\mathbf{F}^p$. Moreover, the Mandel stress tensor $\mathbf{M}^e$ takes the form

$$\mathbf{M}^e = \mathbf{C}^e \cdot \mathbf{S}, \tag{95}$$

where $\mathbf{C}^e = \mathbf{F}^{eT} \cdot \mathbf{F}^e$ is the elastic right Cauchy–Green tensor. The Mandel stress is given by the simple constitutive relation by modifying Eq. (94) as:

$$\mathbf{M}^e = \lambda(\text{tr}[\mathbf{E}^e])\mathbf{I} + 2\mu\mathbf{E}^e. \tag{96}$$

It is important to note that the strain measure employed is the elastic Green–Lagrange tensor $\mathbf{E}^e = \ln\mathbf{U}^e$, where $\mathbf{U}^e$ is the elastic stretch, that is related to the elastic deformation gradient as $\mathbf{F}^e = \mathbf{R}^e\mathbf{U}^e$, where $\mathbf{R}^e$ is the elastic rotation tensor. With this, the expression for the Cauchy stress $\boldsymbol{\sigma}$ takes the form from Eq. (96) as

$$\boldsymbol{\sigma} = J^{-1}\mathbf{R}^e \cdot \mathbf{M}^e \cdot (\mathbf{R}^e)^{\text{T}}. \tag{97}$$

To account for the elastic part of the model, on the contrary to the volumetric-deviatoric decomposition by Amor et al. [4] considered in both Sections 3.2 and 3.3, we employ the split based on the spectral decomposition by Miehe et al. [5] of the elastic strain tensor $\boldsymbol{\varepsilon}$ using the principal strains ε_a, and the principal strains directions $\mathbf{n}_a$ as

$$\boldsymbol{\varepsilon} = \sum_{a=1}^{3} \varepsilon_a \mathbf{n}_a \otimes \mathbf{n}_a. \tag{98}$$

With this at hand, the expression for the free Helmholtz elastic energy considering positive (tensile) and negative (compressive) terms takes the form

$$\Psi_+^{\text{elas}} = \frac{1}{2}\lambda\langle\text{tr}[\varepsilon]\rangle_+^2 + \mu\text{tr}[\langle\varepsilon\rangle_+^2]; \quad \Psi_-^{\text{elas}} = \frac{1}{2}\lambda\langle\text{tr}[\varepsilon]\rangle_-^2 + \mu\text{tr}[\langle\varepsilon\rangle_-^2]. \tag{99}$$

From these expressions, it is easy to propose a total potential functional that accounts only for tensile states affecting the crack growth following the one formulated in Eq. (18). From here, a elasto-viscoplastic constitutive model with isotropic hardening (with J_2 flow theory), is introduced. Assuming that the plastic flow is incompressible (see Eq. (58)), the time evolution equation for the plastic deformation gradient is given by

$$\dot{\mathbf{F}}^p = \mathbf{L}^p \cdot \mathbf{F}^p. \tag{100}$$

where $\mathbf{L}^p$ is the plastic velocity gradient and can be written as

$$\mathbf{L}^p = \sqrt{\frac{1}{2}}\dot{\gamma}\mathbf{n}. \tag{101}$$

Here, the direction of the plastic flow $\mathbf{n}$ is defined by the deviatoric part of the Mandel stress as

$$\mathbf{n} = \frac{\mathbf{s}}{||\mathbf{s}||}; \quad \mathbf{s} = \text{dev}[\mathbf{M}^e], \tag{102}$$

and the equivalent plastic shear strain rate $\dot{\gamma}$ is given by

$$\dot{\gamma} = \dot{\gamma}_0 \left(\frac{||\mathbf{s}||}{\sqrt{2}k(\alpha)} \right)^{1/m}, \tag{103}$$

Here, $\dot{\gamma}_0$ is the referential shear strain rate and m is the testing rate sensitivity, the ratio between $\dot{\gamma}$ and $\dot{\gamma}_0$ defines the viscous character of return mapping plasticity algorithm. The evolution equation for the hardening parameter $k(\alpha)$ can be computed as

$$\dot{k}(\alpha) = K(\alpha_{\text{sat}} - \alpha)\dot{\gamma}, \tag{104}$$

where α is the hardening parameter, α_{sat} is the saturation level for the deformation resistance and K is the linear hardening coefficient. The yield function corresponding to the plastic loading is expressed as

$$f(\mathbf{M}^e, \alpha) = ||\mathbf{s}|| - \sqrt{2}k(\alpha)\left(\frac{\dot{\gamma}}{\dot{\gamma}_0} \right)^m. \tag{105}$$

Due to the presence of damage, the degradation is added to Eq. (105) as

$$f(\mathbf{M}^e, \alpha) = ||\mathbf{s}|| - g(\mathfrak{d})\sqrt{2}k(\alpha)\left(\frac{\dot{\gamma}}{\dot{\gamma}_0} \right)^m. \tag{106}$$

To account for the viscoplastic work affecting the crack growth, the rate of the contribution to the Helmholtz free energy Ψ^{vplas} has the expression of Eq. (63), without stress triaxiality.

In the line of Section 3.2, we start by introducing the KKT conditions as in Eq. (66). The evolution equation (Eq. (100)) is integrated using an exponential map as

$$\mathbf{F}^p_{n+1} = \exp(\Delta t \mathbf{L}^p_{n+1})\mathbf{F}^p_n. \tag{107}$$

Consequently, we obtain the elastic deformation gradient $\mathbf{F}^e$ as

$$\mathbf{F}^e_{n+1} = \mathbf{F}_{n+1}\mathbf{F}^{p-1}_{n+1} \rightarrow \mathbf{F}^e_{n+1} = \mathbf{F}_{n+1}\mathbf{F}^{p-1}_n \exp(-\Delta t \mathbf{L}^p_{n+1}), \tag{108}$$

which introduces the trial state for the elastic deformation gradient, in the sense that

$$\mathbf{F}^e_{n+1} = \mathbf{F}^{e\,\text{trial}} \exp(-\Delta t \mathbf{L}^p_{n+1}); \quad \mathbf{F}^{e\,\text{trial}} = \mathbf{F}_{n+1}\mathbf{F}^{p-1}_n. \tag{109}$$

Due to the polar decomposition in Eq. (109), the expression for updating the Mandel stress accounting the phase-field degradation reads

$$\mathbf{M}^e_{n+1} = \mathbf{M}^{e\,\text{trial}}_{n+1} - \sqrt{2}\mu\Delta\gamma\mathbf{n}_{n+1}; \quad \mathbf{M}^{e\,\text{trial}}_{n+1} = g(\mathfrak{d})[2\mu(\text{dev}[\mathbf{E}^{e\,\text{trial}}_{n+1}]) + \kappa(\text{tr}[\mathbf{E}^{e\,\text{trial}}_{n+1}])\mathbf{I}]. \tag{110}$$

The deviatoric part of the Mandel stress takes the form

$$\text{dev}[\mathbf{M}^e_{n+1}] = \text{dev}[\mathbf{M}^{e\,\text{trial}}_{n+1}] - \sqrt{2}\mu\Delta\gamma\mathbf{n}_{n+1}. \tag{111}$$

Finally, the hardening parameter α, is updated using backward Euler method as

$$\alpha_{n+1} = \frac{\alpha_n + \Delta\gamma K \alpha_{\text{sat}}}{1 + \Delta\gamma K}. \tag{112}$$

In line with the Algorithm 2, the Algorithm 3 presents the detailed algorithm for hyperelasticity–viscoplasticity. Note that Cauchy stresses has to be computed after the return-mapping algorithm, see Eq. (97). In line with Sections 3.2–3.3, the tangent $\mathbb{C}_{\text{ALG}}$ is computed numerically from the Cauchy stresses.

4. Numerical experiments

In order to examine the performance to failure of the three implemented material models and their differences in the 7-parameter non-linear solid shell model, several numerical applications are presented in the sequel. Using the commercial Finite Element software ABAQUS, the first of the experiments will consist in a validation example of a square tensile plate with a hole in the center, studying the influence of the plasticity parameters and the rate of the pulling test in the crack growth and propagation; such series of tests is conducted in Section 4.1. Further illustrations are made on the plasticity regime by replicating the double-notched asymmetric example of the paper by Ambati et al. [57] for the three solid shells approaches in order to shed light on the coupling of the phase-field parameter and the plastic equivalent strains; such conducted tests are carried out in Section 4.2. Subsequently, the trio of numerical frameworks is further extended to comprise cylindrical shell geometries subjected to tensile conditions (Section 4.3) as well as mixed-mode loading scenarios (Section 4.4). Concerning the length scale parameter, our criterion for its selection follows $2h_{\text{max}} = \ell$, where h_{max} is the maximum element size in the crack trajectory.

Algorithm 3 Algorithmic box for the return-mapping J_2 visco-plastic flow algorithm.

1: **Input**: $\mathbf{F}_{n+1}$, $\mathbf{F}_n$, α_n.
2: Compute the damaged elastic predictor:

$$\mathbf{F}^e_{n+1} = \mathbf{F}^{e\ \text{trial}} \exp(-\Delta t \mathbf{L}^p_{n+1}); \quad \mathbf{F}^{e\ \text{trial}} = \mathbf{F}_{n+1}\mathbf{F}^{p-1}_n \tag{113}$$

$$\mathbf{R}^e_{n+1}\mathbf{U}^e_{n+1} = \mathbf{R}^{e\ \text{trial}}_{n+1}\mathbf{U}^{e\ \text{trial}}_{n+1} \exp(-\Delta t \mathbf{L}^p_{n+1}) \ \rightarrow \ \mathbf{E}^e_{n+1} = \ln \mathbf{U}^e_{n+1} = \mathbf{E}^{e\ \text{trial}} - \Delta t \mathbf{L}^p_{n+1} \tag{114}$$

$$\boxed{\mathbf{s}^{\text{trial}}_{n+1} = g(\mathfrak{d})\text{dev}[\mathbf{M}^e_{n+1}] = g(\mathfrak{d})\text{dev}[2\mu(\text{dev}[\mathbf{E}^{e\ \text{trial}}]) + \kappa(\text{tr}[\mathbf{E}^{e\ \text{trial}}])\mathbf{I}]} \tag{115}$$

3: Compute plastic loading

$$\boxed{f^{\text{trial}}_{n+1} = ||\mathbf{s}^{\text{trial}}_{n+1}|| - g(\mathfrak{d})\sqrt{2}k(\alpha)\left(\frac{\dot{\gamma}}{\dot{\gamma}_0}\right)^m.} \tag{116}$$

If Eq. (116) ≤ 0, exit algorithm. Otherwise, go to Step 4.
4: Return-mapping algorithm
The Lagrange multiplier is obtained by solving

$$\boxed{\hat{f}(\Delta\gamma) = ||\mathbf{s}^{\text{trial}}_{n+1}|| - g(\mathfrak{d})\sqrt{2}k(\alpha)\left(\frac{\dot{\gamma}}{\dot{\gamma}_0}\right)^m - g(\mathfrak{d})\sqrt{2}\mu\Delta\gamma.} \tag{117}$$

Update the stress and hardening coefficient as

$$\mathbf{s}_{n+1} = \mathbf{s}^{\text{trial}}_{n+1} - \sqrt{2}\mu\Delta\gamma\mathbf{n}_{n+1}, \qquad \text{(From here, we can easily compute } \boldsymbol{\sigma}_{n+1}\text{, see Eq. (97))} \tag{118}$$

$$\alpha_{n+1} = \frac{\alpha_n + \Delta\gamma K \alpha_{\text{sat}}}{1 + \Delta\gamma K}. \tag{119}$$

5: Update plastic deformation gradient (and compute the kinematical calculations for the trail state)

$$\mathbf{L}^p_{n+1} = \sqrt{\frac{1}{2}}\dot{\gamma}\mathbf{n}_{n+1}, \tag{120}$$

$$\boxed{\mathbf{F}^p_{n+1} = \exp(\Delta t \mathbf{L}^p_{n+1})\mathbf{F}^p_n.} \tag{121}$$

6: Compute energies for elastic an plastic state Ψ^{elas} and Ψ^{vplas} as

$$\Psi^{\text{elas}}_+ = \frac{1}{2}\lambda\langle\text{tr}[\varepsilon]\rangle^2_+ + \mu\text{tr}[\langle\varepsilon\rangle^2_+]; \quad \Psi^{\text{elas}}_- = \frac{1}{2}\lambda\langle\text{tr}[\varepsilon]\rangle^2_- + \mu\text{tr}[\langle\varepsilon\rangle^2_-], \tag{122}$$

$$\dot{\Psi}^{\text{vplas}} = \dot{\gamma}||\mathbf{s}|| \ . \tag{123}$$

4.1. Square tensile plate with a hole

Within this example a square plate is modeled as a benchmark example to shed light on the effects of variation of different material model, where various parametric analyses will be performed to test the performance of the solid shell inelastic models. The geometry is presented in Fig. 4(a), where it is observed that is subject to tension (with displacement control) in the upmost surface and fixed in the bottomost end. Concerning discretization, 6,120 8-node hexahedrical shell elements are employed, with its distribution and orientation being plotted in Fig. 4(b). The material properties common to the three implemented material approaches used to conduct these experiments are exhibited in Table 1, as the rest of them will be discussed in the forthcoming subsections, where we will address the problem in detail for the (a) hyperplastic, (b) visco-hyperelastic and (c) visco-hyperplastic subroutines in detail, to evaluate the main qualitative and quantitative standpoints for every formulation.

4.1.1. Results for hyperplasticity

We commence these series of baseline examples by testing the liability and performance of the solid shell formulation for phase-field in ductile fracture based in the work by Borden et al. [13], whose characteristic properties are listed in Table 2, where it is

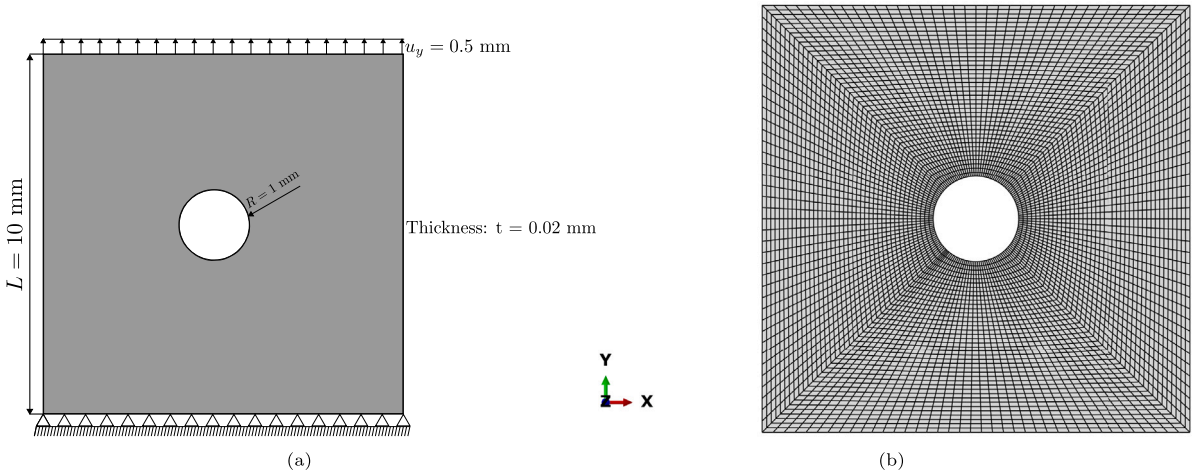

Fig. 4. (a) Dimensions and boundary condition setting and (b) mesh for the square plate with a hole subject to tension.

Table 1
Solid mechanics and phase-field parameters for the conducted plate with a hole experiments.

Property (Unit)	μ (MPa)	κ (MPa)	$\mathcal{G}_c$ (N/mm)	ℓ (mm)
Value	5.93×10^4	8.19×10^4	1.5	0.1

Table 2
Properties of the plasticity model: yield stress, hardening modulus and coefficients considering triaxiality.

Property (Unit)	σ_y (MPa)	K (MPa)	d_1	d_2	d_3
Value	350	500	0.1	3.8	0.0

observed that triaxiality effects are considered within this analysis, as they are an important part for the driving force of the crack initiation and propagation. The main target is to validate the implemented formulation and for that mission, we will focus on the obtained crack patterns and the force–displacement curves, which are compared with the referential work by [13]. In parallel with that paper, we have carried out several analysis by changing the threshold limit that accounts for damage of the plastic strains in the specimen, considering a range of $\Psi_0 = \{0, 5, 10, 15\}$ N/mm that has been studied for the realization of such analysis.

After those initial indications, we simulate crack initiation and growth within this specimen following the boundary conditions stated in Fig. 4(a), with the prescribed displacement indicated in this Figure. Starting with a qualitative address of the problem, we plot the final isocontour of the phase-field fracture for each of the proposed examples with different threshold in Fig. 5. For the same triaxiality effects, although the direction for propagation may differ if it is towards the bottomost or the topmost surface, the damage band initiation is bifurcated into two inclined branches, meaning that the crack will propagate following one of the two directions, thus resulting in a loss of symmetry in the crack trajectory. Total failure of the specimen, i.e., crack reaching the boundaries of the specimen, is not fulfilled due to premature convergence issues, being due to the complexity that solid shells supposes for the strict tolerances in the global Newton–Raphson scheme. However, predictions of such proposed solid shell meets the findings of previous experimental and numerical evidence developed in previous works [57–59].

On the quantitative side, we are aiming to capture the same behavior exhibited in the papers by Borden et al. [13]. For this purpose, we plot local displacement curves for each plastic threshold Ψ_0, along with a pure displacement case, in Fig. 6. In general, results reveal that the elastic and plastic regimes in the different force–displacement curves follow the "no fracture" example for all values of Ψ_0. On the case in absence of threshold, $\Psi_0 = 0$ N/mm, the softening happens before reaching the yield stress, thus the plastic regime is exhibited in the reduction of the force and it can be seen as prolongued, due to a competition between the hardening effect obtained from extra plastic strain and the degradation caused by the phase-field function $g(\mathfrak{d})$. For the cases considering threshold, $\Psi_0 > 0$ N/mm it is observed that the original yield force is maintained meaning that the accumulation of damage is not achieved until such threshold is overpassed. Upon yielding, the strain is dominated by plastic strain and degradation appears later in the plastic regime when Ψ_0 is met. Such findings solidly agree with those obtained in Borden et al. [13], thus, proving that our solid shell formulation is endowed to replicate such relevant results for ductile fracture.

4.1.2. Results for visco-hyperelasticity

Benchmark square plate with a hole specimen is tested following a viscoelastic regime, built-on the visco-hyperelastic element of Valverde-González et al. [43] in the field of visco-hyperelasticity. To achieve such objective, we test this solid shell formulation for

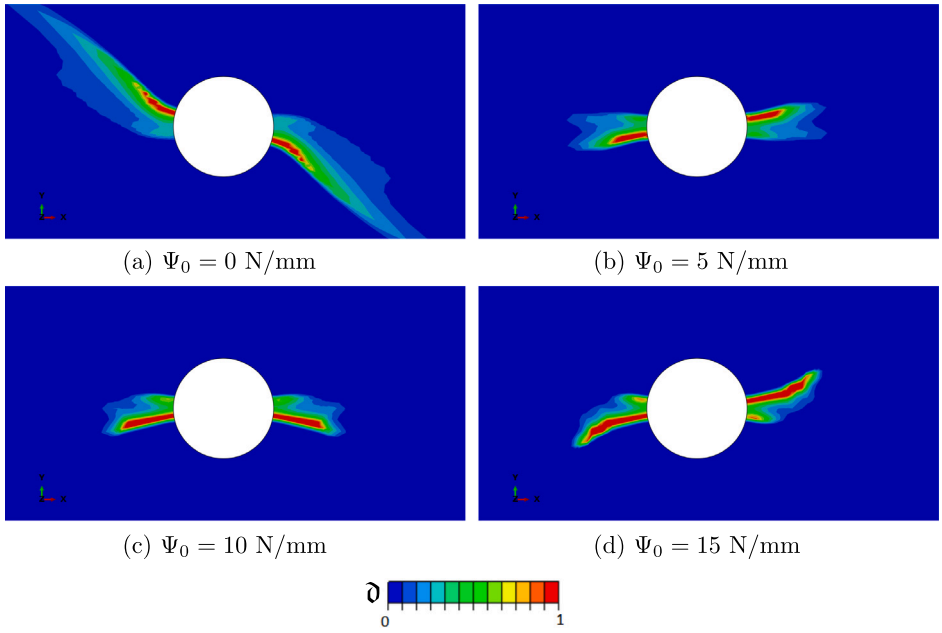

Fig. 5. Contour plots of the phase-field parameter for fracture for the final achieved increment in the hyperplastic tensile plate with a hole in the center, where the pristine and broken states are denoted by the blue and red color, respectively.

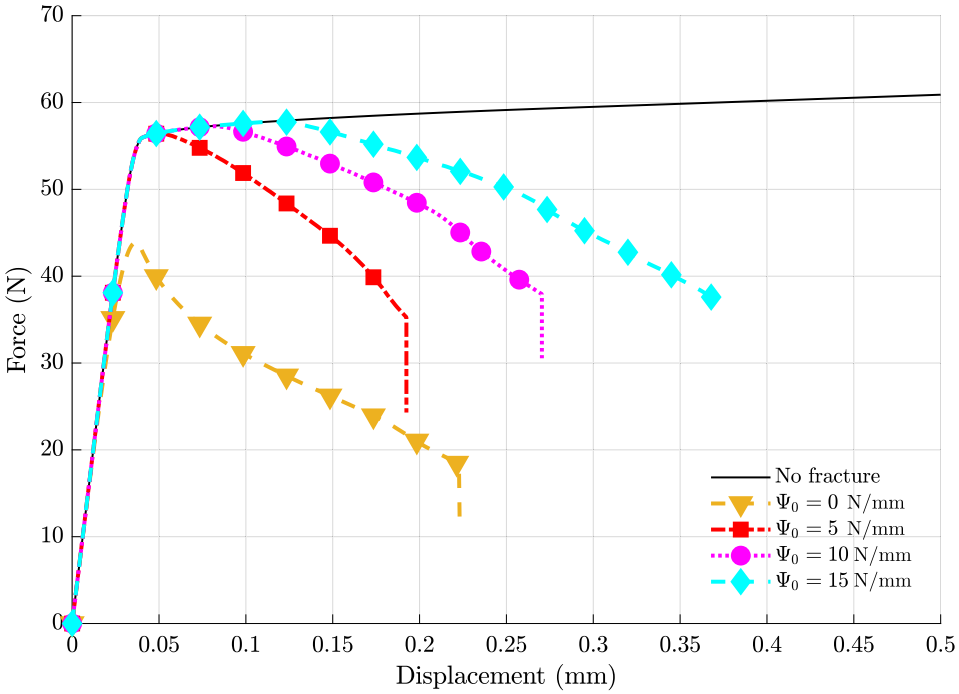

Fig. 6. Force–displacement constitutive response using several different values for the work threshold Ψ_0 in the elasto-plastic tensile plate with a hole in the center.

phase-field fracture in rate-dependent conditions. For that, we will only consider one viscous subdomain with a fixed viscous shear modulus $\mu^{\text{visco}} = 6.5 \times 10^4$ MPa. This Sections encompasses three series of experiments changing the relaxation time $\tau = \{0.1, 1, 10\}$ s and within each one of them, dependence on the test rate has been studied, considering $v = \{0.01, 0.02, 0.05, 0.1, 0.2\}$ mm/s.

On the first place, focus has been devoted in capturing the isocontour phase-field fracture for the visco-hyperelastic square plate with a hole. As can be observed in Fig. 7, the visco-hyperelastic specimen follows a classic Mode I fracture mode, with the

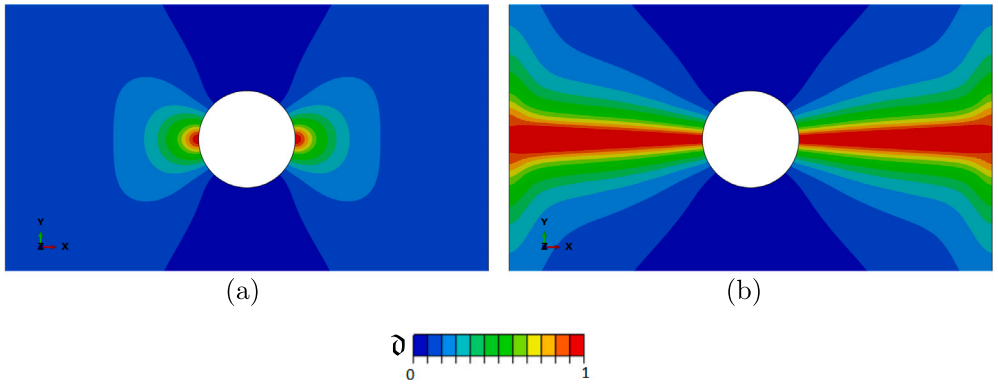

Fig. 7. Contour plots of the phase-field parameter for visco-elastic fracture in the tensile shell with a hole in the center during: Mode I (a) crack initiation and (b) propagation for the case with parameters for time relaxation $\tau = 1$ s and displacement rate $v = 0.2$ mm/s.

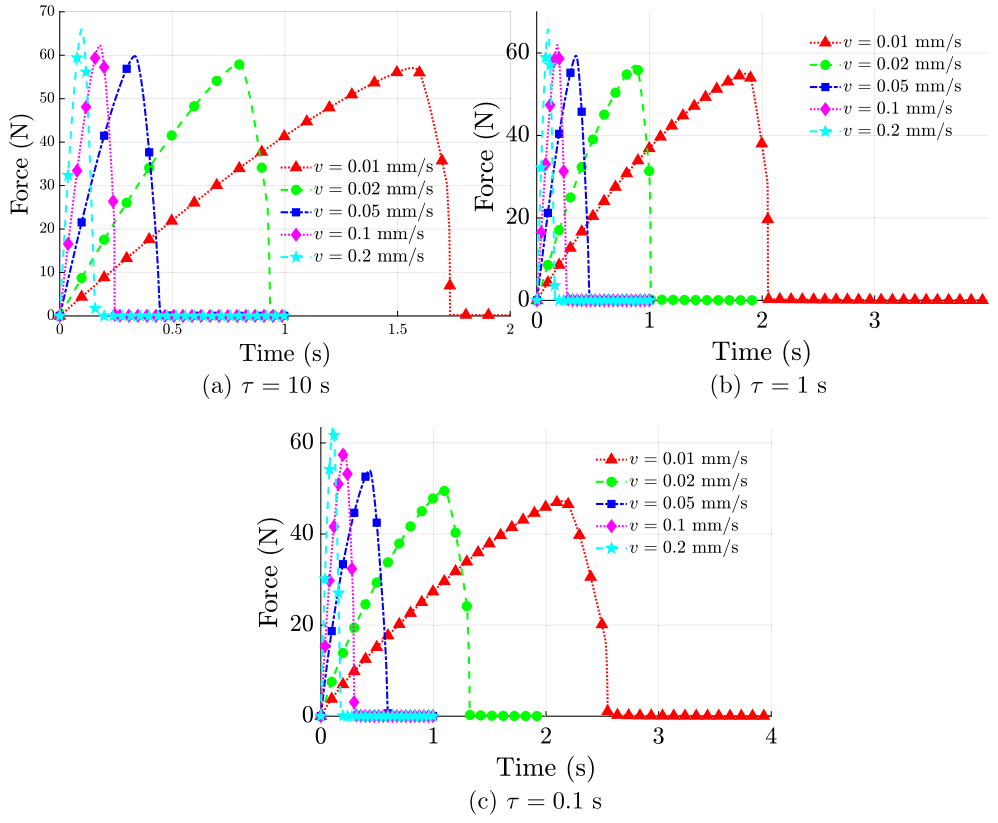

Fig. 8. Force–displacement curves for the visco-elastic tensile shell with a hole in the center. They are been sorted in here by relaxation time employed, encompassing (a) $\tau = 10$ s, (b) $\tau = 1$ s and (c) $\tau = 0.1$ s.

crack nucleating and growing in the perpendicular direction where the load is applied. This pattern is repeated for all the tests concerning this viscoelastic plate with a hole and as expected, is the representative failure trajectory for such specimen in such material conditions, being this in line with [43].

Quantifying the mechanical responses, in Fig. 8 is plotted the force–displacement curves sorted by relaxation time and from here, several standpoints are extracted. To begin with, it is observed how by increasing the relaxation time, as the viscous effects have not vanished yet, the failure of the specimen is triggered to a higher rate, resulting in a more premature failure. Furthermore, it is envisaged the increase of the peak forces with a bigger test velocity for the same relaxation times. It can also be evidenced how slightly they decrease when the relaxation time is diminished, being more distinguishable when dropping for smaller

Table 3
Properties of the viscoplasticity model: saturated deformation resistance, hardening modulus, referential shear rate, test rate sensitivity exponent and energy threshold.

Property (Unit)	α_{sat}	K (MPa)	$\dot{\gamma}_0$ (s^{-1})	m	Ψ_0 (N/mm)
Value	2.5	500	1×10^{-3}	0.05	10

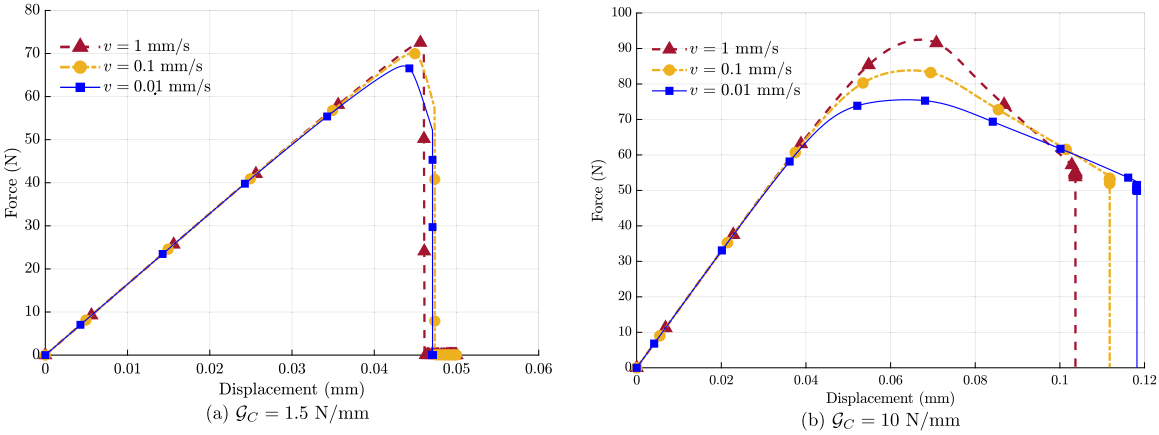

Fig. 9. Force–displacement constitutive response for different testing rates in the square plate with a hole in the center following a viscoplastic regime. These results are obtained for a (a) $\mathcal{G}_C = 1.5$ N/mm and (b) $\mathcal{G}_C = 10$ N/mm.

experiment rates. Such findings are in agreement with the nonlinear viscoelasticity theory and therefore, it may be stated that the implementation of shell theory in the field of rate-dependent materials has been accomplished.

4.1.3. Results for visco-hyperplasticity

Fulfilling this benchmark example, we run the solid shell example following the outlined visco-hyperplastic approach. The characteristic viscoplastic properties tested in this experiment are envisaged in Table 3. Considering that from the qualitative standpoint, the phase-field isocontour obtained matches with the one represented in Fig. 7, special focus is devoted to the quantitative side of the analysis. To fully cover the potentiality that the hyperelastic–viscoplastic approach for solid shells can reach, we will have two different situations for the material considered.

First, the modeling considers a case where the critical energy release rate $\mathcal{G}_C = 1.5$ N/mm (the one plotted in Table 1) is not large enough for the sample to stand for a considerable plastic regime and therefore, the mechanical behavior of the specimen is dominated by the elastic behavior. The results obtained in the form of force–displacement curves are represented in Fig. 9(a) and we can observe some analogies from the previous probes in viscoelasticity (Section 4.1.2), as the peak force augments along with the velocity of the test. After the maximum force has been reached for both specimens, curves enter the softening regime characteristic of the competition between phase-field degradation and plastic hardening and it can be envisaged that the duration of such part is hugely sensitive on the displacement rate, commencing earlier and being more prolonged for smaller rates.

Further findings are obtained by increasing the critical energy release rate up to a value of $\mathcal{G}_C = 10$ N/mm, as the curves represented in Fig. 9(b) reveal that the plastic hardening regime and subsequently, the drop in load is lengthened as the displacement rate is decreased. As the toughness of the model has been increased, also the softening of the instances is extended up to double the displacement compared to the examples with smaller $\mathcal{G}_C$. The plots of these series of experiments exhibit the performance of the visco-hyperplastic model for solid shell modeling in capturing not only the plastic regime but also its rate dependence, a feature that is brand new for Finite Element modeling in fully-integrated solid shells.

4.2. Double-notched asymmetric specimen

Following Ambati et al. [57], it is examined the double-notched asymmetrically disposed specimen illustrated in Fig. 10(a), with a fixed bottomost surface and the topmost surface being displaced vertically and restrained horizontally. The employed material properties in solid mechanics and phase-field approach coincide with those plotted in Table 1. Concerning the discretization of the model, it includes 27,085 hexahedrical shell elements, with special refining being made in the central region between the notches where the crack is expected to nucleate and grow, being zoomed in Fig. 10(b). Like the previous Section, several experiments concerning parametric analyses have been made with the three different materials to prove the potentiality of the implemented formulations.

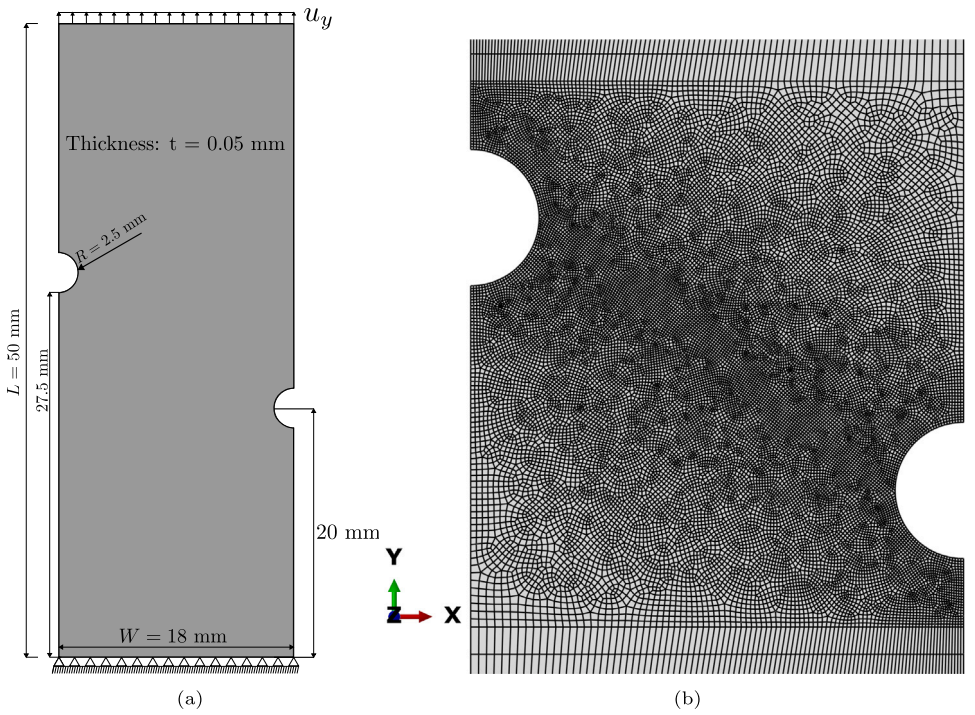

Fig. 10. (a) Dimensions and boundary condition setting and (b) zoomed mesh in the center for the double notched asymmetric specimen subject to tension.

4.2.1. Results for hyperplasticity

Tests comprising hyperplastic specimens in here match the findings of the work by Ambati et al. [57]. Following the properties represented in Table 2, we have conducted experiments by changing the energy threshold in a range such as $\Psi_0 = \{0, 1.5, 3, 4, 5\}$ N/mm.

The evolution of the phase-field parameter for fracture is provided in Fig. 11. For all the three represented models, the crack starts nucleating at both notch roots. However, for the subsequent propagation stage, there are important differences depending on the value of the energy threshold. For specimens with the smaller thresholds, the crack starts propagating horizontally to the notch, subsequently deviating towards the center of the sample as fracture reaches half of its width. As Ψ_0 is augmented, the two initial cracks take a different path during propagation, eventually merging and dividing the sample into two separated pieces leading to complete failure. These phase-field isocontours agree with the fracture map reached by the proposed model of Ambati et al. [57], therefore, justifying the postulation of the threshold to account for the contribution of the plastic deformations. The quantitative effect of the delay of the application of critical equivalent plastic strains in the damage model is highlighted in terms of load–displacement curves in Fig. 12, where it is observed the onset of fracture being belated for increasing values of displacement by augmenting Ψ_0.

4.2.2. Results for visco-hyperelasticity

Concerning the visco-hyperelastic material, we have covered several analysis in the double notched specimen pinpointing the viscous dependence. To accomplish such task, the analyses have encompassed four different viscous mechanisms, with their viscous shear modulus as $\mu^{\text{visco}} = \{6.5 \times 10^4; 60.0 \times 10^4; 5.15 \times 10^4; 1.0 \times 10^4\}$ MPa and relaxation times as $\tau = \{5; 0.05; 100; 1 \times 10^{-6}\}$ s, respectively. With these properties at hand, three series of numerical experiments varying $\mathcal{G}_C = \{1.5, 5, 10\}$ N/mm are considered and within each one of them, the test velocity is modified in the ranges of $v = \{0.05, 0.5, 5\}$ mm/s.

The evolution of the fracture process for each one of the conducted specimens is exhibited in Figs. 13(a)–13(c), where it is envisaged that, at the beginning, the trajectory of the crack coincides with the one without energy threshold for the hyperplastic specimen (Fig. 11(a)), i.e., horizontal course. Nevertheless, there is no deviation towards the center in its evolution, as it continues in Mode I upon reaching the boundary limits of the sample.

Comparing from a quantitative standpoint, Figs. 14(a)–14(c) display the force–displacement graphs for each test sorted by different critical release rate. Comparing the different images, it can be observed how, as expected, the increase in the maximum load is projected as $\mathcal{G}_C$ is augmented. Within the graphs for similar fracture toughness, we envisage reflected the viscoelastic behavior, as by increasing the displacement rate, the maximum force grows leading to a more premature final displacement for failure.

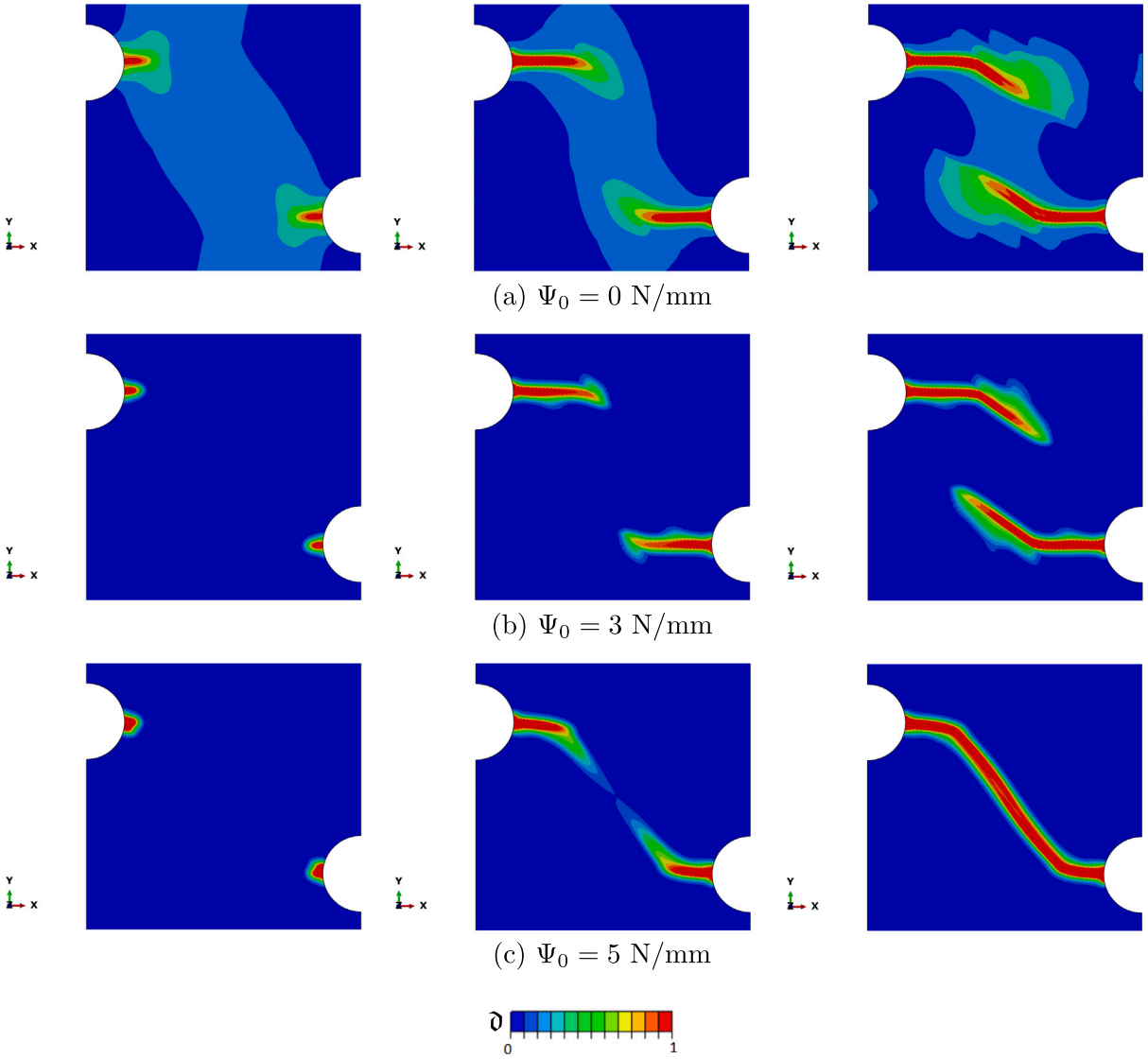

Fig. 11. Contour plots of the phase-field parameter for the hyperplastic double-notched asymmetric shell. In here, it is represented the evolution for crack nucleation and growth for (a) $\Psi_0 = 0$ N/mm, (b) $\Psi_0 = 3$ N/mm and (c) $\Psi_0 = 5$ N/mm.

4.2.3. Results for visco-hyperplasticity

Concerning the visco-hyperplastic approach, we have carried out a parametric analysis studying the dependence on the rate sensitivity of the specimen by studying the variation of the exponent m. Reaching a similar result in terms of fracture as the visco-hyperelastic sample (see Fig. 7), the parametric study encompasses a range of $m = \{0.05, 0.1, 0, 5\}$, analyzing for each exponent three different displacement rates $v = \{0.05, 0.1, 0.5\}$ mm/s. The rest of the plastic properties can be found in Table 3.

Force–displacement curves are represented for the different m values in Figs. 15(a)–15(c). It is envisaged a predominant elastic behavior for the samples with $m = 0.05$ and $m = 0.1$, where the curve upon reaching the peak force of its behavior quickly experiences a softening behavior, being extended for smaller displacement rates, as predicted by the previous tests conducted on viscoplastic specimens (see Section 4.1.3). However, once the exponent is augmented to a value of $m = 0.5$, the dominant trajectory changes, as the modification caused by the displacement rate is more highlighted on these cases. Indeed, specimens with higher values of m demonstrate a reduction in the maximum force as the displacement rate decreases, ultimately resulting in a transition to the plastic regime and leading to a bigger elongation prior to fracture. To distinguish the effect of the exponent m, the plot in Fig. 15(d) reflects the enhancement in the viscous behavior such larger exponent causes, as it enlarges the hardening during the viscoplastic regime. Therefore, from here, it is recommended that in order to reflect the visco-plastic behavior of the specimen, one should select a high enough rate-sensitivity exponent m to discern it.

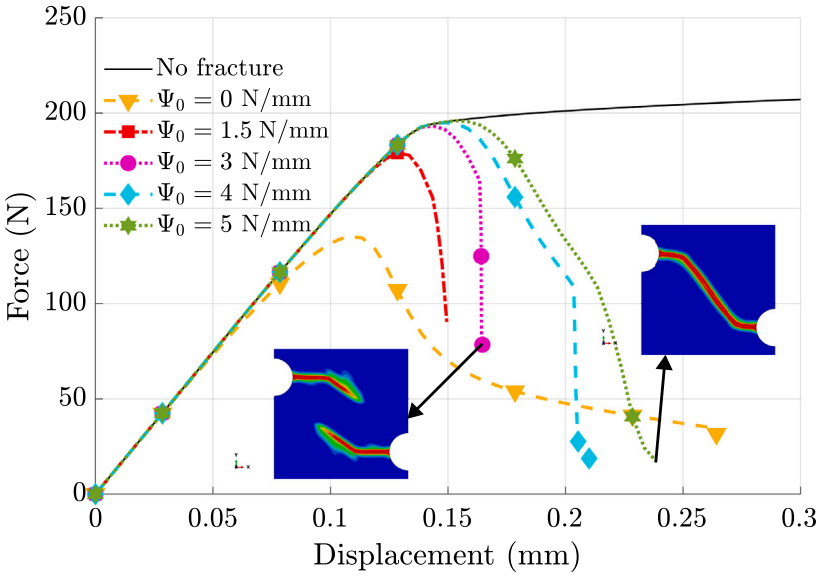

Fig. 12. Force–displacement constitutive response using several different values for the energy threshold Ψ_0 in the hyperplastic double-notched asymmetric sample. In the micrograph is included a couple of relevant phase-field contour maps, where red and blue denote the broken and intact states, respectively.

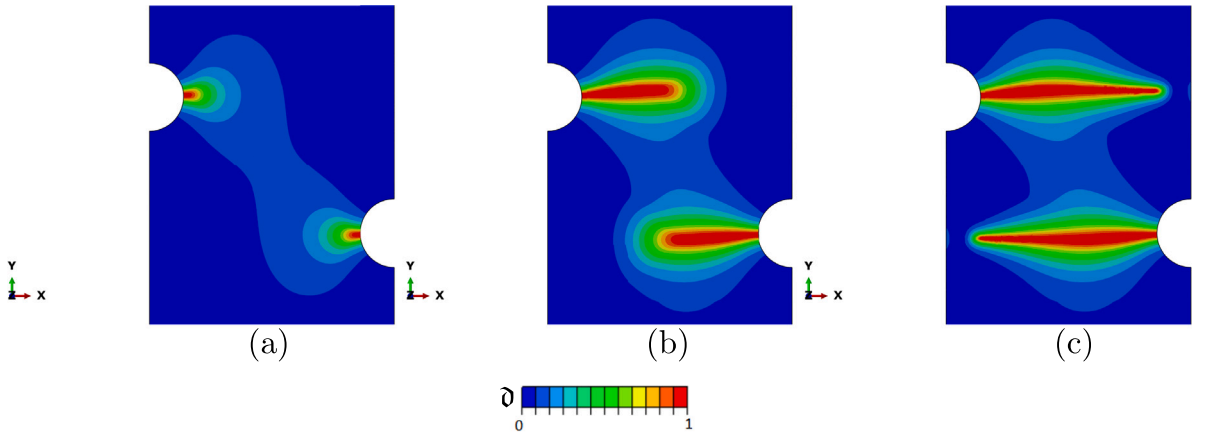

Fig. 13. Contour plots of the phase-field parameter for visco-elastic fracture in the double notched asymmetric specimen during: (a) crack initiation, (b) propagation and (c) fractured sample for the case with $\mathcal{G}_C = 5$ N/mm and displacement rate $v = 0.5$ mm/s.

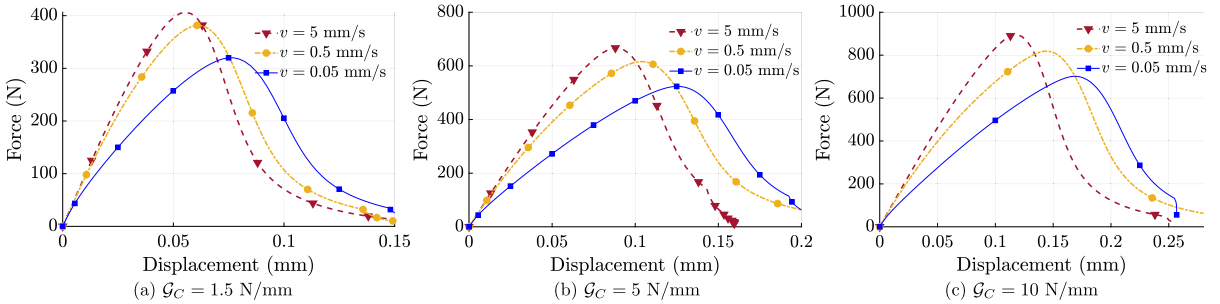

Fig. 14. Force–displacement curves for the visco-elastic double-notched asymmetric specimen. They are been sorted in here by critical energy release rate employed, encompassing (a) $\mathcal{G}_C = 1.5$ N/mm, (b) $\mathcal{G}_C = 5$ N/mm and (c) $\mathcal{G}_C = 10$ N/mm.

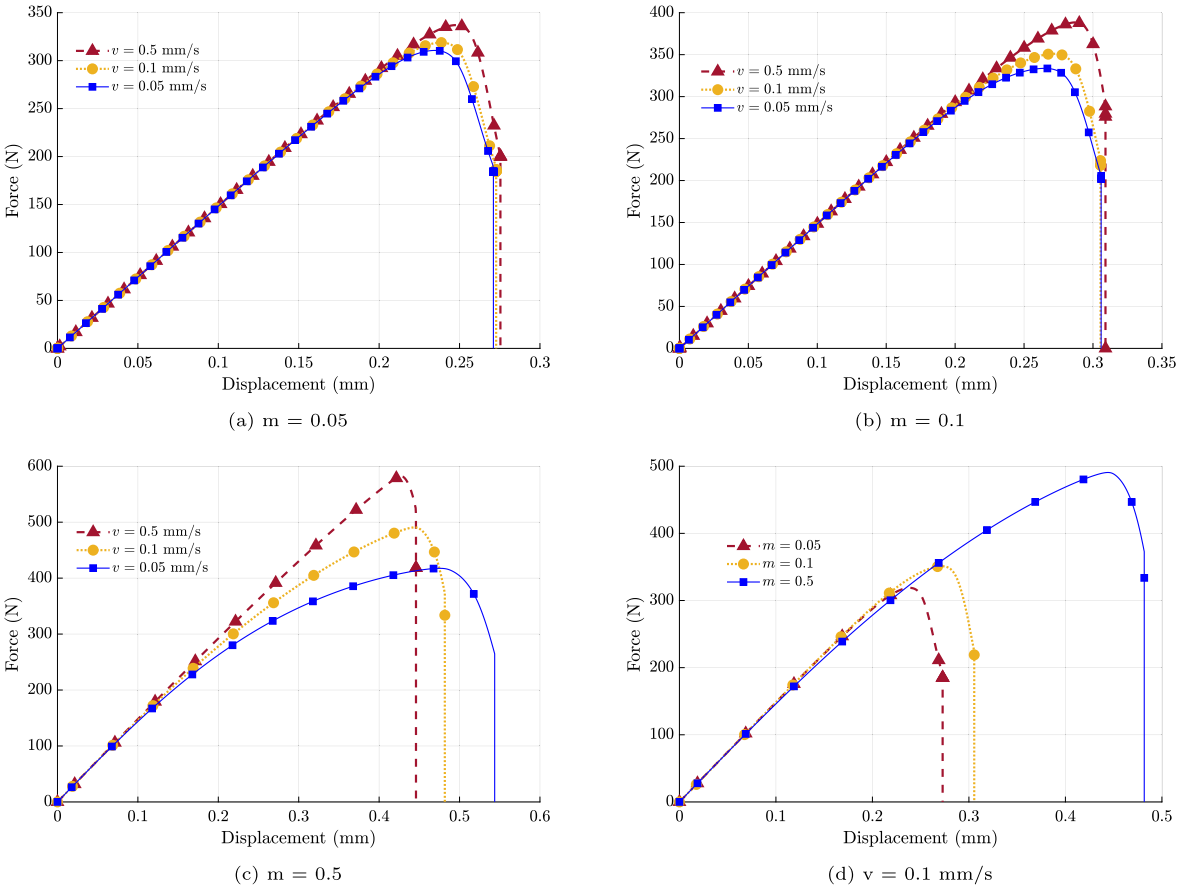

Fig. 15. Visco-plastic double notched asymmetric specimen: the first three series of graphs display the variation of the specimen behavior for different m, encompassing (a) $m = 0.05$, (b) $m = 0.1$ and (c) = $m = 0.5$. The representations in (d) for the same displacement rate of $v = 0.1$ mm/s highlight such enhancements with the increase of the exponent.

Table 4
Solid mechanics and phase-field parameters for the cylindrical shell plate with a hole experiments.

Property (Unit)	μ (MPa)	κ (MPa)	$\mathcal{G}_C$ (N/mm)	ℓ (mm)
Value	3.35×10^4	8.19×10^4	1.5	0.1

4.3. Cylinder with hole - tensile conditions

The latter part of the experiments addresses failure in cylindrical specimens, known for their susceptibility to locking phenomena under mechanical loading conditions. The results under the tensile loading in the context of brittle failure can be seen in [36] for comparison. This example, in particular, considers a half-cylindrical shell with a hole in the center under tensile conditions. The geometrical description and boundary conditions are presented in Fig. 16(a). The description follows the radius of the cylinder $R = 2$ mm, and the length of the cylinder is considered to be $L = 20$ mm. The circular hole in the center has a radius of $r = 0.15$ mm, and the thickness of the cylinder is considered as $H = 0.01$ mm, representing a thin sheet. Concerning discretization, the model is meshed with 12,491 hexahedrical elements. One of the sides is fully fixed, whereas, on the other side, a displacement-controlled load is applied in tension. The rest of this Section details the effects of the different formulations and their corresponding results.

4.3.1. Results for hyperplasticity

Solid mechanics and phase-field properties considered for this example are plotted in Table 4 and plastic properties are exhibited in Table 2. In line with the previous considerations, the effect of the variation of the energy threshold is emphasized, considering a range of $\Psi_0 = \{0, 5, 10, 15, 20\}$ N/mm for the analysis. Fig. 16(b) presents the force–displacement plots for the variation of the Ψ_0. In parallel to the plane specimens, when the threshold is absent, the crack nucleation occurs without any yielding. Consequently, the plastic regime is dominated by the reduction of the reaction force due to the damage. On the other hand, when the $\Psi_0 > 0$,

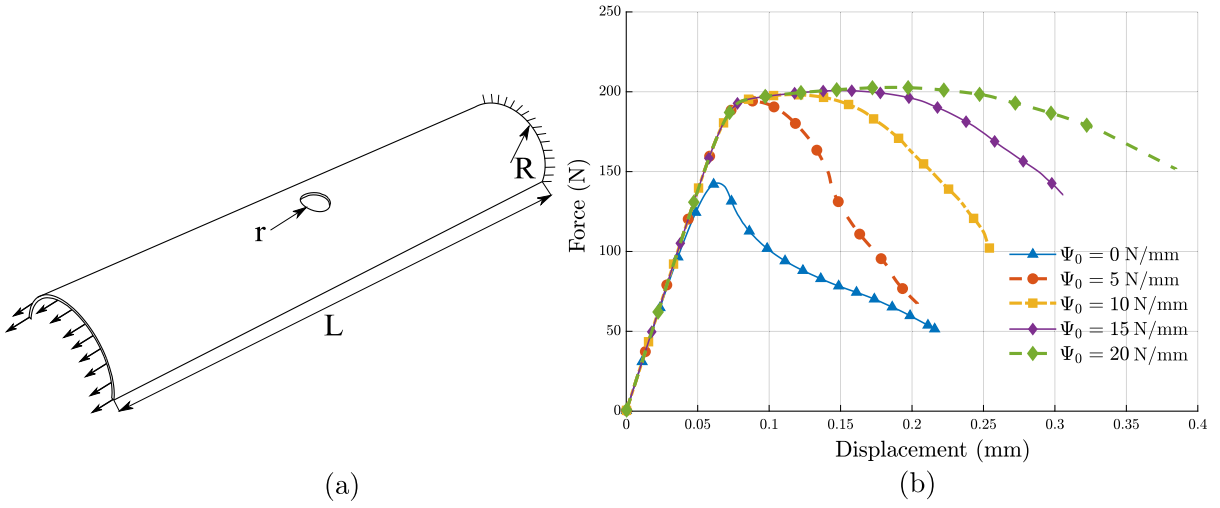

Fig. 16. (a) Geometrical description of the cylinder with the central hole. (b) Force–displacement curves for the variation of the threshold energy Ψ_0 in the hyper-plastic problem.

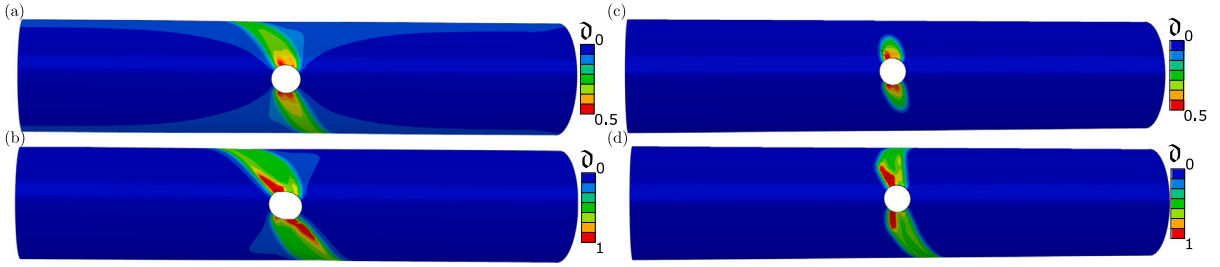

Fig. 17. Hyper-plastic cylindrical shell under tension: (a) Nucleation of the crack, and (b) propagation of the crack when the threshold is $\Psi_0 = 0$ N/mm. (c) Nucleation of the crack, and (d) propagation of the crack when the threshold $\Psi_0 = 5$ N/mm.

plastic yield is observed. As the threshold increases, the accumulation of the damage causes a delay in the fracture. Consequently, this leads to more pronounced plastic effects. Moreover, if the $\Psi_0 \to \infty$ leads to no fracture. In these cases, the damage initiation and propagation is delayed and is properly reflected in Fig. 16(b).

Figs. 17(a)–17(b) present the crack nucleation and propagation of the crack when $\Psi_0 = 0$ N/mm, whereas Figs. 17(c)–17(d) exhibit the crack nucleation and propagation when $\Psi_0 = 5$ N/mm. Due to the stress triaxiality, in the $\Psi_0 = 0$ N/mm case, the damage band is split into two oppositely inclined symmetric branches. Consequently, the crack propagation follows both branches. On the other hand, when $\Psi_0 = 5$ N/mm, the damage band at nucleation is split in the same directions, but it loses symmetry in further stages. From this, we can extract that for the half-cylindrical shell under tensile conditions the unsymmetric crack propagation is triggered when the energy threshold is $\Psi_0 > 0$.

4.3.2. Results for visco-hyperelasticity

The cylinder with a hole in the center is tested at a visco-hyperelastic regime. Employing the mechanical properties displayed in Table 4, a series of numerical experiments with relaxation time $\tau = \{1, 2\}$ s are presented to study the dependence of the test rates. Considering one viscous subdomain with a fixed viscous shear modulus $\mu^{\text{visco}} = 6.5 \times 10^4$ MPa, for a relaxation time of $\tau = 1$ s, displacement rates of $v = \{0.6, 0.5, 0.4, 0.2, 0.1\}$ mm/s are adopted, whereas for $\tau = 2$ s, test rates of $v = \{0.3, 0.25, 0.2, 0.15, 0.05\}$ mm/s are considered. The reason for this unequal distribution of the test rate can be seen in Fig. 18, where it is observed that by increasing the relaxation time, the viscous effects have not vanished and the failure of the specimen is triggered prematurely. Additionally, the peak reactions constantly decrease as the load rate decreases. Concerning qualitative results, it is highlighted in Fig. 19 that, due to the viscous effects, the crack nucleation and propagation are similar to the elastic regime where the crack propagation is straight, leading to a pure Mode I failure.

4.3.3. Results for visco-hyperplasticity

For the visco-hyperplastic cylindrical shell, following mechanical properties plotted in Table 3, a threshold energy of $\Psi_0 = 1$ N/mm is chosen and the load rate is changed on the range of $v = \{2, 0.5, 0.23, 0.15, 0.133, 0.1\}$ mm/s. Fig. 20(a) presents the force–displacement graphs, and Fig. 20(b) presents the force-time graphs, both emphasizing the rate dependency of the structure.

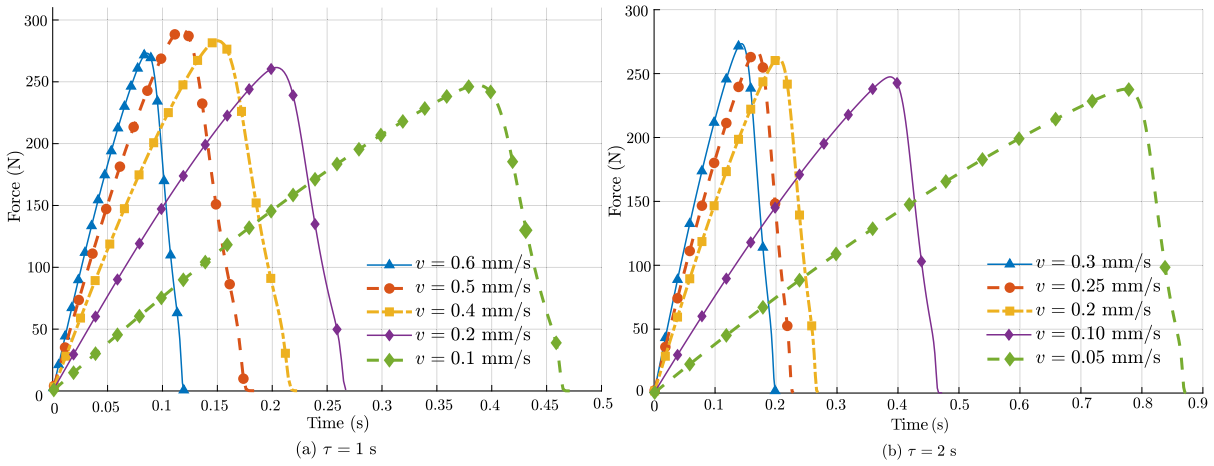

Fig. 18. Force-time curves for the visco-elastic behavior of cylinder with a hole under tensile loading. The results are sorted by relaxation time employed, encompassing (a) $\tau = 1$ s, (b) $\tau = 2$ s.

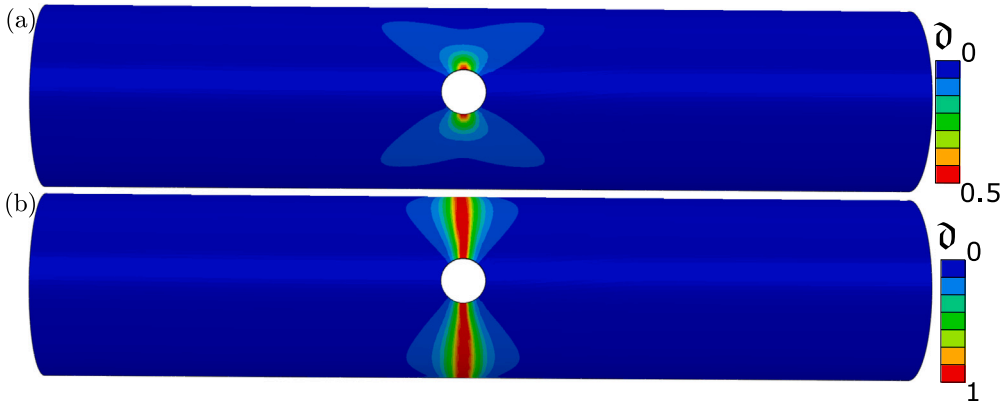

Fig. 19. (a) Crack nucleation, and (b) propagation in visco-elastic cylinder shell with a hole under tensile conditions.

Due to the low threshold, as in the plastic case, the load reaction triggers an unstable crack growth (as the ones obtained in Fig. 19). Moreover, the effects of the load rate on the structure can be seen. As the load rate increases, the maximum load-carrying capacity of the structure also increases, reflecting the viscous effects.

4.4. Cylinder with hole - mixed loading conditions

This example considers the half-cylindrical shell with a hole in the center, now with mixed loading conditions. The same dimensions and mesh as in the tensile tests are considered for this series of numerical examples. One side of the cylinder is fully restrained, whereas, on the other side, a displacement-controlled load is applied in tension and bending. The reason for the tension load alongside the bending load is to avoid the crack starting from the boundaries. Moreover, the bending of the cylinder allows extensive use of the ANS and EAS parameters, which in its absence leads to numerical locking. Furthermore, the effects of different material models are presented in the sequel.

4.4.1. Results for hyperplasticity

The considered material properties are plotted in Table 4, whereas the plastic properties are shown in Table 2. The effect of the variation of the energy threshold is emphasized for mixed loading conditions, using a range of $\Psi_0 = \{0, 2.5, 5, 7.5, 10, 12.5, 15\}$ N/mm for the comprehensive analysis. Fig. 21(b) presents the force–displacement plots for the variation of the Ψ_0. Similar to the results in the previous Section, when the threshold is absent, the crack nucleation occurs without any yielding. Moreover, due to the bending, the damage at the boundary can be seen. On the other hand, when the $\Psi_0 > 0$, plastic yield can be seen. As the energy threshold increases, damage accumulation is delayed. Consequently, this leads to more pronounced plastic hardening effects. Moreover, as the Ψ_0 increases, bending effects dominate, leading to fracture at the boundaries. Upon studying these results along with the tensile

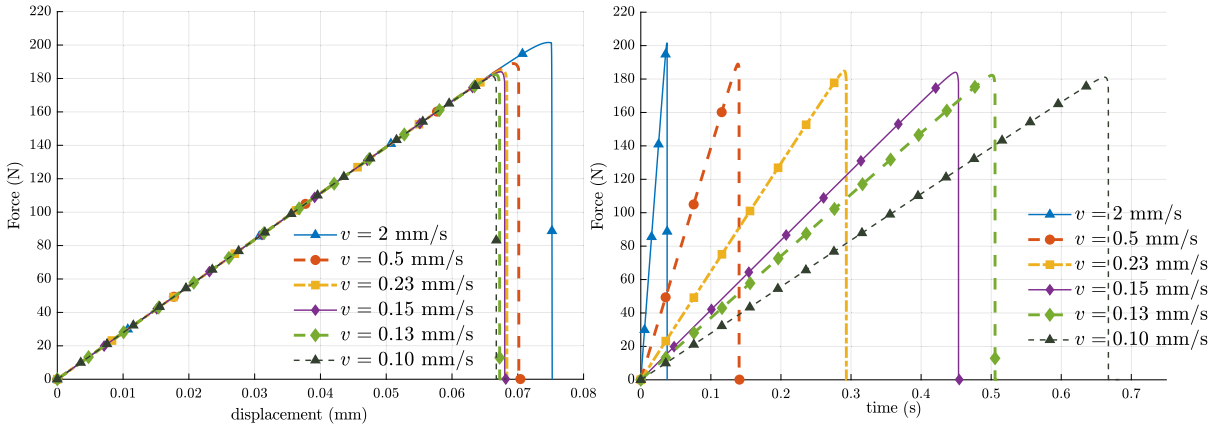

Fig. 20. (a) Force vs. displacement curve in the cylinder with a hole under tensile conditions in the viscoplastic regime with threshold energy of $\Psi_0 = 1$ N/mm and relaxation time $\tau = 1$ s. (b) Force vs. time curve in the cylinder with a hole under tensile conditions in viscoplastic regime with threshold energy of $\Psi_0 = 1$ N/mm and relaxation time $\tau = 1$ s.

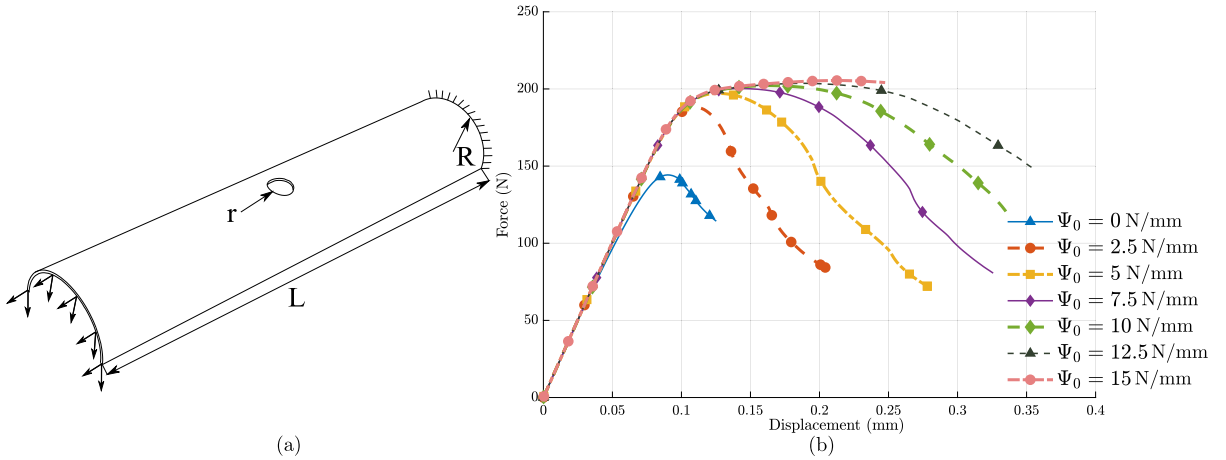

Fig. 21. (a) Geometrical description of the cylinder with a hole in a mixed loading condition. (b) Force–displacement plots for the variation of the threshold energy Ψ_0 in the hyperplastic problem.

loading tests in Fig. 16(b), the alleviation of locking pathologies is evident as the force–displacement curves for mixed loading closely match the magnitude observed in the pure tensile loading tests.

Figs. 22(a)–22(b) present the crack nucleation and propagation of the crack when $\Psi_0 = 2.5$ N/mm, whereas Figs. 22(c)–22(d) present the crack nucleation and propagation when $\Psi_0 = 5$ N/mm. Due to the stress triaxiality, the damage band is split, thus symmetry is lost. As a consequence, one can observe the unsymmetric crack propagation. As the threshold increases, the unsymmetry in the crack bands starts to grow, which is evident from Fig. 22(d).

4.4.2. Results for visco-hyperelasticity

The cylinder with a hole in the center is tested at the viscoelastic regime for mixed loading conditions to understand the difference in viscous effect and the peak reaction force due to the viscous effect, and also, to evidence that locking pathologies are alleviated by the activation of the ANS and EAS parameters. In this regard, we consider the mechanical properties displayed in Table 4 varying relaxation time as in the previous Section considering one viscous subdomain with $\mu^{\text{visco}} = 6.5{\times}10^4$ MPa. Following this line, a series of numerical experiments with relaxation time $\tau = \{1, 2\}$ s is presented with varying test rates to study the dependence of the test rate, considering the displacement rates that are adopted in Section 4.3.2. Fig. 23(a) presents the force–displacement graph, whereas Fig. 23(b) addresses the force-time curves. As the relaxation time increases, the viscous effects do not vanish, as a consequence, the maximum reaction force increases. As the magnitude of the curves is in the same level as the specimens for pure tensile loading (see Fig. 18), we can confirm that also the locking problem is solved for the visco-elastic regime. It is also important to note that the crack nucleation and propagation are mixed mode loading due to the viscous effects.

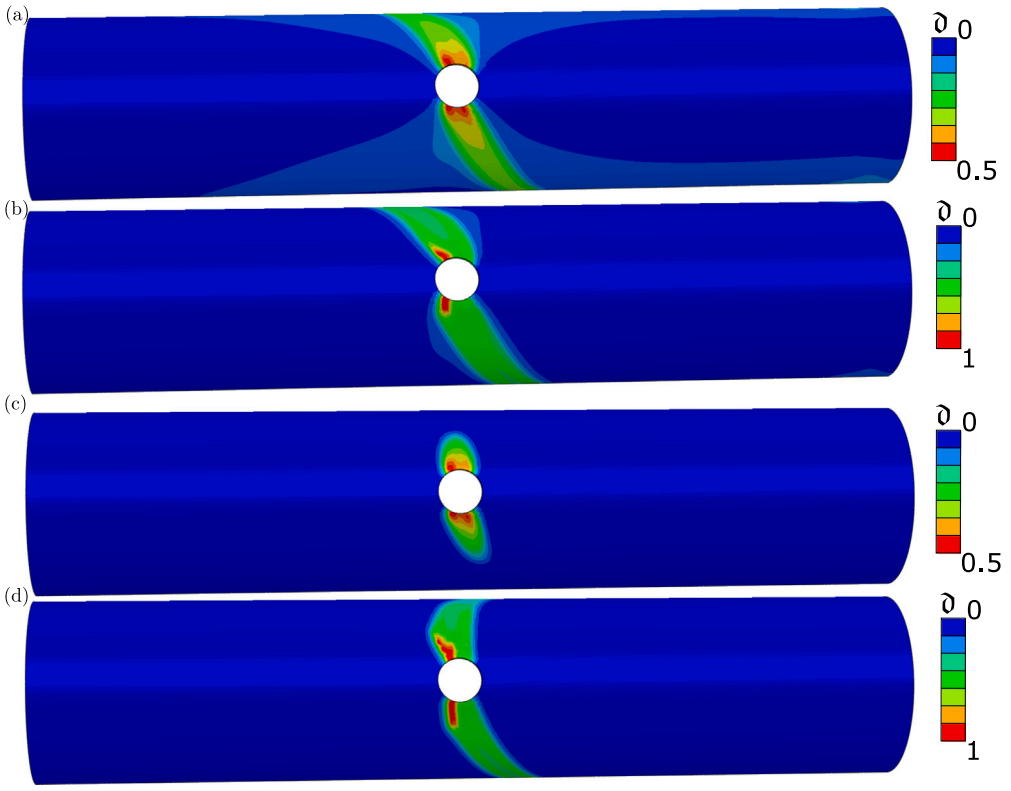

Fig. 22. Hyper-plastic cylindrical shell under mixed loading:(a) Nucleation of the crack, and (b) propagation of the crack when the threshold $\Psi_0 = 2.5$ N/mm. (c) Nucleation of the crack, and (d) propagation of the crack when the threshold $\Psi_0 = 5$ N/mm.

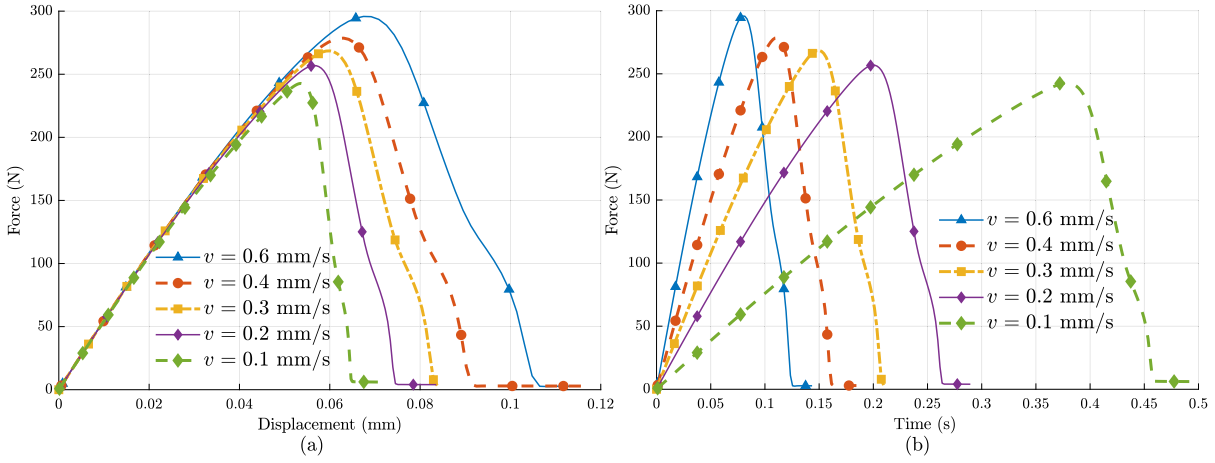

Fig. 23. (a) Force vs. Displacement, and (b) Force vs. Time for the visco-elastic mixed loading cylinder with a hole for relaxation time of $\tau = 1$ s.

4.4.3. Results for visco-hyperplasticity

Lastly, we analyze the behavior of the visco-hyperplastic material in mixed loading conditions. Considering the plastic properties displayed in Table 3, we adopt a threshold energy of $\Psi_0 = 1$ N/mm with the loading rate of $v = \{0.5, 0.4, 0.3, 0.2, 0.1\}$ mm/s. Figs. 24(a)–24(b) display the crack nucleation and propagation. It is envisaged as the plastic effect is more dominant, this results in crack propagation according to the plasticity rule. Moreover, the crack propagation in the mixed loading follows a stable crack growth even for low threshold energy, which fundamentally defers from the pure tensile loading. This could be attributed to the combined effects of Mode I and Mode II failure modes at the crack tip. Furthermore, Fig. 25(a) presents the force–displacement, and Fig. 25(b) presents the force-time plots for the various loading rates. It can be seen that as the load rate increases, the maximum

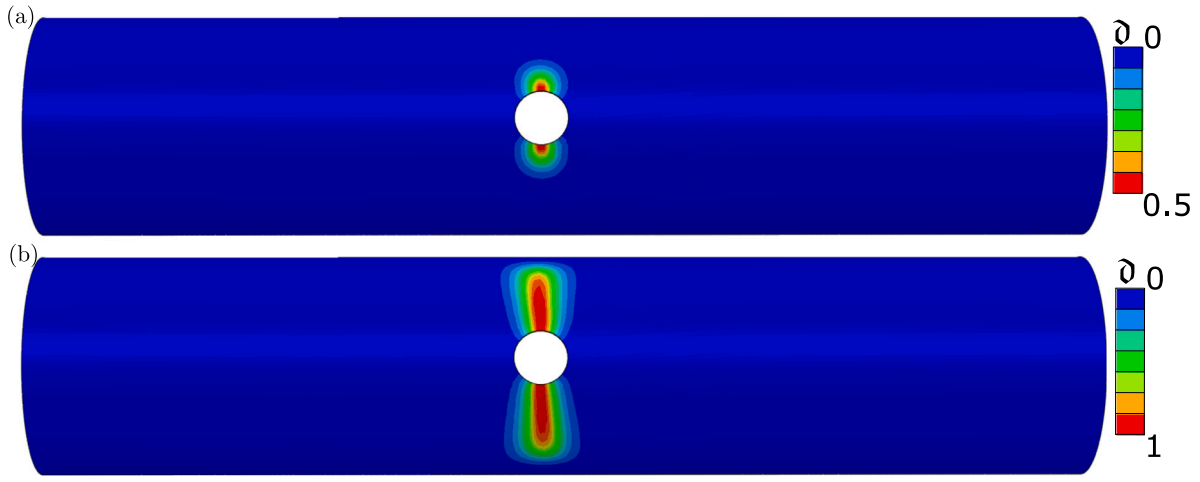

Fig. 24. Crack nucleation and crack propagation in the cylinder with hole for viscoplastic mixed loading.

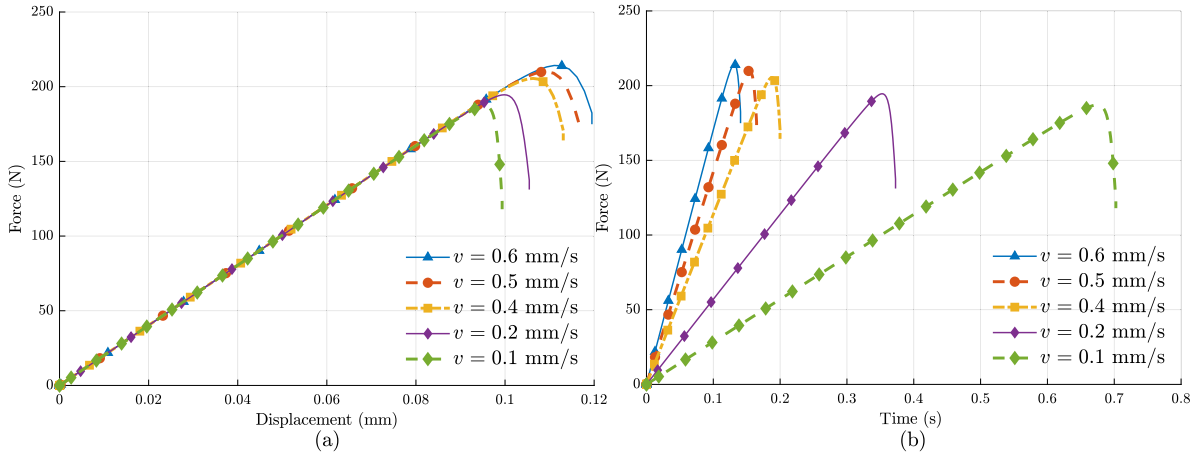

Fig. 25. (a) Force vs. Displacement, and (b) Force vs. Time for the visco-plastic mixed loading cylinder with a hole for relaxation time of $\tau = 1$ s and $\Psi_0 = 1$ N/mm.

reactions increase, emphasizing the viscoplastic effects in the structure. Moreover, it is observed that the EAS and ANS formulations effectively mitigate the issue of locking also in the context of visco-plastic behavior. This is evident as the resulting curves exhibit values of the same magnitude as those corresponding to pure tensile loading, as illustrated comparing Fig. 25 with Fig. 20. This consistency further reflects the efficacy of these formulations in addressing complex mechanical behaviors in structures prone to exhibit locking problems.

5. Conclusions

This paper outlines the numerical implementation of a general purpose nonlinear FE code of hyper-plastic, visco-hyperelastic, and visco-hyperplastic models into the solid shell model for fracture analysis. Specifically, the current formulation of such representative inelastic material models has been integrated in conjunction with the EAS and ANS techniques, which effectively addresses and mitigates locking pathologies and the incorporation of the phase-field approach to simulate cracking events. Despite the increase in computational cost and the convergence issues mentioned earlier, these new developments represent a significant advancement on the existing literature within the realm of inelastic fully-integrated solid shells.

First, the seminal experiments of a inelastic square tensile plate from Borden et al. [13] and the ductile fracture of a double-notched asymmetric sample from Ambati et al. [57] have been used as verification of the proposed solid shell theory. In these instances, the hyper-plastic formulation has demonstrated its ability to capture both crack trajectory and mechanical behavior of these numerical experiments characterized by notable evolution of plastic effects. Second, in the context of the materials encompassing viscous events, rate-dependent phenomena in these samples has been robustly simulated, aligning closely with theoretical expectations.

Consequently, this research has been extended to more relevant problems in the context of modeling of solid shells. In the context of this, the analysis of large displacements and subsequently, ductile fracture of cylindrical solid shell specimens subject to mixed loading conditions, encompassing both pulling and bending, has been captured. Notably, these simulations successfully account for the alleviation of locking events in these scenarios.

Current results pinpoint the applicability of the proposed formulation, rendering to promising simulation tools for the evaluation of real-life problems in the automotive and aerospace sectors, among others, where applications concerning shell structures with inelastic mechanical effects and fracture are of relevant importance.

CRediT authorship contribution statement

Angel Valverde-González: Writing – review & editing, Writing – original draft, Visualization, Validation, Software, Methodology, Investigation, Formal analysis, Conceptualization. **Pavan Kumar Asur Vijaya Kumar:** Writing – review & editing, Writing – original draft, Validation, Methodology, Investigation, Conceptualization. **Adria Quintanas-Corominas:** Writing – review & editing, Software, Methodology, Investigation, Conceptualization. **José Reinoso:** Writing – review & editing, Writing – original draft, Visualization, Supervision, Project administration, Formal analysis, Conceptualization.

Declaration of competing interest

The authors declare that they have no known competing financial interests or personal relationships that could have appeared to influence the work reported in this paper.

Data availability

Data will be made available on request.

Acknowledgments

The authors appreciate the financial support of Ministerio de Ciencia e Innovación de España, Spain (Projects TED2021-131649B-I00 and PID2020-117001GB-I00/AEI/10.13039/501100011033).

Appendix. Code listing for FE implementation

The listings included in here are all related to Section 3.1.2. To facilitate the reader's comprehension, we recommend following this Appendix in conjunction with the aforementioned Section.

Listing 1: Computation of covariant and contravariant basis and metrics.

```
1
      subroutine ks8metShellBody10(x,shapef,dshape,xi,nnode,ndim,
     *   gkov,gkon,gmkov,gmkon,detgkon)
      IMPLICIT NONE
! ------- Definitions ....
6     do i=1,3
          do j =1,3
              do k=1,8
                  gkov(j,i) = gkov(j,i) + dshape(i,k)*x(j,k)
              enddo
11        enddo
      enddo

      do i=1,3
          do j=1,3
16            gkon(i,j) = gkov(i,j)
          enddo
      enddo
! ------- Compute the determinant
      detgkon= ....
21! ------- Compute the inverse for the Contravariant basis
      do i=1,3
          do j=1,3
              gkon (i,j) = gkoni(i,j)
          end do
26    end do
```

```
! ------- Transpose gkon
! ------- covariant metric tensor -------
      do i=1,ndim
          do j=1,ndim
              do k=1,ndim
                  gmkov(i,j) =gmkov(i,j) + gkov(k,i)*gkov(k,j)
              end do
          end do
      end do
! -------  Calculate the inverse metrics contravariant gmkon  -------

      return
      end
```

Listing 2: Computation of the displacement-strain **B**(**d**) operator.

```
!-----------------------------------------------------------
      subroutine kBoperatorS10(Bop,gkov,dshape,nnode,ndim)
      IMPLICIT NONE
! ------- Definitions ....
! ------- initialization
      counter=1
      do inode=1,8
          Bop(1,counter)=       dshape(1,inode)*gkov(1,1)
          Bop(1,counter+1)=     dshape(1,inode)*gkov(2,1)
          Bop(1,counter+2)=     dshape(1,inode)*gkov(3,1)
!---------------------------------------
          Bop(2,counter)=      dshape(2,inode)*gkov(1,2)
          Bop(2,counter+1)=    dshape(2,inode)*gkov(2,2)
          Bop(2,counter+2)=    dshape(2,inode)*gkov(3,2)
!---------------------------------------
          Bop(3,counter) =     dshape(3,inode)*gkov(1,3)
          Bop(3,counter+1) =   dshape(3,inode)*gkov(2,3)
          Bop(3,counter+2) =   dshape(3,inode)*gkov(3,3)
!---------------------------------------
          Bop(4,counter) =    dshape(1,inode)*gkov(1,2) +
     *                       dshape(2,inode)*gkov(1,1)
          Bop(4,counter+1) =  dshape(1,inode)*gkov(2,2) +
     *                       dshape(2,inode)*gkov(2,1)
          Bop(4,counter+2) =  dshape(1,inode)*gkov(3,2) +
     *                       dshape(2,inode)*gkov(3,1)
!---------------------------------------
          Bop(5,counter) =    dshape(1,inode)*gkov(1,3) +
     *                       dshape(3,inode)*gkov(1,1)
          Bop(5,counter+1) =  dshape(1,inode)*gkov(2,3) +
     *                       dshape(3,inode)*gkov(2,1)
          Bop(5,counter+2) =  dshape(1,inode)*gkov(3,3) +
     *                       dshape(3,inode)*gkov(3,1)
!---------------------------------------
          Bop(6,counter )  =  dshape(2,inode)*gkov(1,3) +
     *                       dshape(3,inode)*gkov(1,2)
          Bop(6,counter+1) =  dshape(2,inode)*gkov(2,3) +
     *                       dshape(3,inode)*gkov(2,2)
          Bop(6,counter+2) =  dshape(2,inode)*gkov(3,3) +
     *                       dshape(3,inode)*gkov(3,2)
          counter=counter+ndim
      enddo

      return
      end
```

Listing 3: Computation of the B-operator for the alleviation of trapezoidal locking.

```
!------------------------------------------------------------
!------------------------------------------------------------
      subroutine kANStrapS10(Bop,ndim,nnode,ntens,gkovcT,frT,dshapeT,nANStrap)

      IMPLICIT NONE
      !initialization
      !definition
      node_st = 1
      do innode = 1,nnode

          do jq=1,nANStrap
              BopAux(3,node_st) =   BopAux(3,node_st)   +
     1        frT(jq)*dshapeT(jq,3,innode)*gkovcT(jq,1,3)

              BopAux(3,node_st+1) = BopAux(3,node_st+1) +
     1        frT(jq)*dshapeT(jq,3,innode)*gkovcT(jq,2,3)

              BopAux(3,node_st+2) = BopAux(3,node_st+2) +
     1        frT(jq)*dshapeT(jq,3,innode)*gkovcT(jq,3,3)
          enddo
          node_st   =  node_st  + ndim
      enddo

      do i=1,ntens
          do j=1,nnode*ndim
              Bop(i,j) =   Bop(i,j) + BopAux(i,j)
          enddo
      enddo

      return
      end
```

Listing 4: Computation of the B-operator for the alleviation of shear locking.

```
!------------------------------------------------------------
      subroutine kANSshearS10(Bop,ndim,nnode,ntens,gkovc1q1,
     1 gkovc2q2,frq,fsq,dshape1q1,dshape2q2,nANSshear)

      IMPLICIT NONE

      !initialization
      !definition
      node_st = 1
      do innode = 1,nnode
      ! 13 component

          BopAux (5,node_st) = BopAux(5,node_st)+
     1    frq(1)*dshape1q1(1,1,innode)*gkovc1q1(1,1,3) +
     2    frq(1)*dshape1q1(1,3,innode)*gkovc1q1(1,1,1) +
     3    frq(2)*dshape1q1(2,1,innode)*gkovc1q1(2,1,3) +
     4    frq(2)*dshape1q1(2,3,innode)*gkovc1q1(2,1,1)


          BopAux (5,node_st+1) = BopAux(5,node_st+1)+
     1    frq(1)*dshape1q1(1,1,innode)*gkovc1q1(1,2,3) +
     2    frq(1)*dshape1q1(1,3,innode)*gkovc1q1(1,2,1) +
     3    frq(2)*dshape1q1(2,1,innode)*gkovc1q1(2,2,3) +
     4    frq(2)*dshape1q1(2,3,innode)*gkovc1q1(2,2,1)


          BopAux (5,node_st+2) = BopAux(5,node_st+2)+
     1    frq(1)*dshape1q1(1,1,innode)*gkovc1q1(1,3,3) +
```

```
      2    frq(1)*dshape1q1(1,3,innode)*gkovc1q1(1,3,1) +
      3    frq(2)*dshape1q1(2,1,innode)*gkovc1q1(2,3,3) +
      4    frq(2)*dshape1q1(2,3,innode)*gkovc1q1(2,3,1)

       ! 23 component

           BopAux (6,node_st) = BopAux(6,node_st) +
      1    fsq(1)*dshape2q2(1,2,innode)*gkovc2q2(1,1,3) +
      2    fsq(1)*dshape2q2(1,3,innode)*gkovc2q2(1,1,2) +
      3    fsq(2)*dshape2q2(2,2,innode)*gkovc2q2(2,1,3) +
      4    fsq(2)*dshape2q2(2,3,innode)*gkovc2q2(2,1,2)


           BopAux (6,node_st+1) = BopAux(6,node_st+1) +
      1    fsq(1)*dshape2q2(1,2,innode)*gkovc2q2(1,2,3) +
      2    fsq(1)*dshape2q2(1,3,innode)*gkovc2q2(1,2,2) +
      3    fsq(2)*dshape2q2(2,2,innode)*gkovc2q2(2,2,3) +
      4    fsq(2)*dshape2q2(2,3,innode)*gkovc2q2(2,2,2)

           BopAux (6,node_st+2) = BopAux(6,node_st+2) +
      1    fsq(1)*dshape2q2(1,2,innode)*gkovc2q2(1,3,3) +
      2    fsq(1)*dshape2q2(1,3,innode)*gkovc2q2(1,3,2) +
      3    fsq(2)*dshape2q2(2,2,innode)*gkovc2q2(2,3,3) +
      4    fsq(2)*dshape2q2(2,3,innode)*gkovc2q2(2,3,2)

           node_st   = node_st   + ndim
       enddo

       do i=1,ntens
           do j=1,nnode*ndim
               Bop(i,j) =    Bop(i,j) + BopAux(i,j)
           enddo
       enddo

       return
       end
!-------------------------------------------------------------
```

Listing 5: Conversion of stress and material Jacobi tangent from cartesian to curvilinear.

```
!-----------------Convert stresses from cartesian to curvilinear--------------------
       subroutine  kcarttocurv(stress_cart, gkon, stress)

       IMPLICIT NONE

       do k=1,3
           do l=1,3
               stress_curv(k,l)=0.0d0
               do i=1,3
                   do j=1,3
                       stress_curv(k,l)=stress_curv(k,l)+gkon(i,k)*gkon(j,l)*stress_cart(i
                           ,j)
                   enddo
               enddo
           enddo
       enddo


       do i=1,3
           do j=1,3
               stress_curv(i,j)=(stress_curv(i,j)+stress_curv(j,i))/2.d0
           enddo
       enddo
```

```
      stress(1)= stress_curv(1,1)
      stress(2)= stress_curv(2,2)
      stress(3)= stress_curv(3,3)
      stress(4)= stress_curv(1,2)
      stress(5)= stress_curv(2,3)
      stress(6)= stress_curv(1,3)

      return
      end

!-----------------Convert Jacobi tangent from cartesian to curvilinear
    --------------------
      subroutine  ks84koncacu(Cmat_Cart, gkon, cmat)
      IMPLICIT NONE

      DATA    Nota/1,4,6,
     1            4,2,5,
     2            6,5,3/

      do i=1,3
          do j=1,3
              do k=1,3
                  do l=1,3
                      Cmat_curv(i,j,k,l) = 0.d0
                      do m=1,3
                          do n=1,3 ! this to curvilinear
                              do p=1,3
                                  do q=1,3
                                      Cmat_curv(i,j,k,l)=Cmat_curv(i,j,k,l) + Cmat_Cart(m
                                          ,n,p,q)*gkon(m,i)*gkon(n,j)*gkon(p,k)*gkon(q,l)
                                  enddo
                              enddo
                          enddo
                      enddo
                  enddo
              enddo
          enddo
      enddo

      cmat(:,:)=0.0d0
      do kk=1,3
          do mm=1,3
              do pp=1,3
                  do qq=1,3
                      cmatR(Nota(kk,mm),Nota(pp,qq))=Cmat_curv(kk,mm,pp,qq)
                  end do
              end do
          end do
      end do

      do i=1,6
          do j=1,6
              cmat(i,j)= (cmatR(i,j)+cmatR(j,i)) / 2.0d0
          enddo
      enddo

      return
      end
```

Listing 6: Computation of the $\mathbf{M}(\xi)$ operator.

```
!-----------------------------------------------------------
```

```
      subroutine kEASMlocal(r,s,t,Weasloc,nEAS)

      IMPLICIT NONE

      !initialization
      !definition


      rr = 1 !11 component
      ss = 2 !22 component
      tt = 3 !33 component
      rs = 4 !12 component
      rt = 5 !13 component
      st = 6 !23 component

      indexcol = 1

      Weasloc(rr,1) = xi1
      Weasloc(ss,2) = xi2

      Weasloc(tt,3) = xi3
      Weasloc(tt,4) = xi1*xi3
      Weasloc(tt,5) = xi2*xi3

      Weasloc(rs,6) = xi1
      Weasloc(rs,7) = xi2

      return
      end
```

Listing 7: Computation of $\tilde{\mathbf{E}}$.

```
!-------------------------------------------------------------

      subroutine kEASTransform(Weas,T0mat,gkovr,gkonr0,Weasloc,
     1  ndim,nnode,detr0,detr,nEAS)

      IMPLICIT NONE

    !initialization
    !definition
      TOL = 1.0d-15

      factor0= detr0/detr !relation between both determinants
      do i=1,3
          t11 = t11 + gkonr0(i,1)* gkovr(i,1)
          t12 = t12 + gkonr0(i,1)* gkovr(i,2)
          t13 = t13 + gkonr0(i,1)* gkovr(i,3)

          t21 = t21 + gkonr0(i,2)* gkovr(i,1)
          t22 = t22 + gkonr0(i,2)* gkovr(i,2)
          t23 = t23 + gkonr0(i,2)* gkovr(i,3)

          t31 = t31 + gkonr0(i,3)* gkovr(i,1)
          t32 = t32 + gkonr0(i,3)* gkovr(i,2)
          t33 = t33 + gkonr0(i,3)* gkovr(i,3)
      enddo

      !Matrix T

      T0mat(1,1) = t11*t11*factor0
      T0mat(1,2) = t21*t21*factor0
```

```
        T0mat(1,3) = t31*t31*factor0
        T0mat(1,4) = t11*t21*factor0
        T0mat(1,5) = t11*t31*factor0
        T0mat(1,6) = t21*t31*factor0

        T0mat(2,1) = t12*t12*factor0
        T0mat(2,2) = t22*t22*factor0
        T0mat(2,3) = t32*t32*factor0
        T0mat(2,4) = t12*t22*factor0
        T0mat(2,5) = t12*t32*factor0
        T0mat(2,6) = t22*t32*factor0

        T0mat(3,1) = t13*t13*factor0
        T0mat(3,2) = t23*t23*factor0
        T0mat(3,3) = t33*t33*factor0
        T0mat(3,4) = t13*t23*factor0
        T0mat(3,5) = t13*t33*factor0
        T0mat(3,6) = t23*t33*factor0

        T0mat(4,1) = (t11*t12 + t12*t11)*factor0
        T0mat(4,2) = (t21*t22 + t22*t21)*factor0
        T0mat(4,3) = (t31*t32 + t32*t31)*factor0
        T0mat(4,4) = (t11*t22 + t12*t21)*factor0
        T0mat(4,5) = (t11*t32 + t12*t31)*factor0
        T0mat(4,6) = (t21*t32 + t22*t31)*factor0

        T0mat(5,1) = (t12*t13 + t13*t12)*factor0
        T0mat(5,2) = (t22*t23 + t23*t22)*factor0
        T0mat(5,3) = (t32*t33 + t33*t32)*factor0
        T0mat(5,4) = (t12*t23 + t13*t22)*factor0
        T0mat(5,5) = (t22*t33 + t23*t32)*factor0
        T0mat(5,6) = (t12*t33 + t13*t32)*factor0

        T0mat(6,1) = (t11*t13 + t13*t11)*factor0
        T0mat(6,2) = (t21*t23 + t23*t21)*factor0
        T0mat(6,3) = (t31*t33 + t33*t31)*factor0
        T0mat(6,4) = (t11*t23 + t13*t21)*factor0
        T0mat(6,5) = (t21*t33 + t23*t31)*factor0
        T0mat(6,6) = (t11*t33 + t13*t31)*factor0

        do i=1,6
            do j=1,6

                if (abs(T0mat(i,j)).LT.TOL) then
                    T0mat(i,j) =  0.d0
                endif
            enddo
        enddo

        Weas = matmul(T0mat,Weasloc)
        do i=1,6
            do j=1,nEAS
                if (abs(Weas(i,j)).LE.TOL) then
                    Weas(i,j) =  0.d0
                endif
            enddo
        enddo

        !initialization
        do i=1,6
            Etilde(i,1) = 0.d0
        enddo

        Etilde = matmul(Weas,EASstrain)

        return
```

```
      end
```

Listing 8: Computation of the geometrical stiffness matrix.

```
!-----------------------------------------------------------
      subroutine kStiffGeomS10Alt(Kgdd,shapef,dshape,stress,ndim,nnode,
     *  ntens)

      IMPLICIT NONE

      !initialization
     !definition

      node_st=1 !initialization index of rows

      do i=1,nnode

          indexcol = 1 !initialization index of columns

          do k=1,nnode

              dNidr =   dshape(1,i)
              dNids =   dshape(2,i)
              dNidt =   dshape(3,i)

              dNkdr =   dshape(1,k)
              dNkds =   dshape(2,k)
              dNkdt =   dshape(3,k)

              Gamma =dNidr*dNkdr*stress(1)+ (dNidr*dNkds+dNids*dNkdr)*stress(4)+
     *            (dNidr*dNkdt + dNidt*dNkdr)*stress(5) + dNids*dNkds*stress(2)+
     *            (dNids*dNkdt + dNidt*dNkds)*stress(6) + dNidt*dNkdt*stress(3)

              Kgdd(node_st,indexcol) =  Gamma
              Kgdd(node_st+1,indexcol+1) =  Gamma
              Kgdd(node_st+2,indexcol+2) =  Gamma

              indexcol = indexcol+3 !update index of columns

          enddo !end k

          node_st = node_st+3 !update index of rwos
      enddo !end i

      return
      end
```

Listing 9: Computation of the geometrical stiffness matrix modified by the ANS technique.

```
!-----------------------------------------------------------

      subroutine kStiffGeomS10AltANS(Kgdd,shapef,dshape,stress,ndim,
     1 nnode,ntens,gkovc1q1,gkovc2q2,frq,fsq,dshape1q1,dshape2q2,
     2 nANSshear,ANSshearpar,gkovcT,frT,dshapeT,nANStrap,ANStrappar)

      IMPLICIT NONE

      !initialization
      !definition
```

```
      node_st=1 !initialization index of rows

      do i=1,nnode
          indexcol = 1 !initialization index of columns

          do k=1,nnode

              dNidr =   dshape(1,i)
              dNids =   dshape(2,i)
              dNidt =   dshape(3,i)

              dNkdr =   dshape(1,k)
              dNkds =   dshape(2,k)
              dNkdt =   dshape(3,k)

              Gamma11 = dNidr*dNkdr
              Gamma12 = dNidr*dNkds+dNids*dNkdr
              Gamma22 = dNids*dNkds

!------- ANS shear
              if (ANSshearpar.ne.0.d0) then

                  Gamma13 = frq(1)*(dshape1q1(1,1,i)*dshape1q1(1,3,k)) +
     1            frq(1)*(dshape1q1(1,3,i)*dshape1q1(1,1,k)) +
     2            frq(2)*(dshape1q1(2,1,i)*dshape1q1(2,3,k)) +
     3            frq(2)*(dshape1q1(2,3,i)*dshape1q1(2,1,k))

                  Gamma23 = fsq(1)*(dshape2q2(1,2,i)*dshape2q2(1,3,k)) +
     1            fsq(1)*(dshape2q2(1,3,i)*dshape2q2(1,2,k)) +
     2            fsq(2)*(dshape2q2(2,2,i)*dshape2q2(2,3,k)) +
     3            fsq(2)*(dshape2q2(2,3,i)*dshape2q2(2,2,k))

              else

                  Gamma13 = dNidr*dNkdt + dNidt*dNkdr
                  Gamma23 = dNids*dNkdt + dNidt*dNkds

              endif

!------- ANS trap
              if (ANStrappar.ne.0.d0) then

                  Gamma33 = frT(1)*dshapeT(1,3,i)*dshapeT(1,3,k) +
     1            frT(2)*dshapeT(2,3,i)*dshapeT(2,3,k) +
     2            frT(3)*dshapeT(3,3,i)*dshapeT(3,3,k) +
     3            frT(4)*dshapeT(4,3,i)*dshapeT(4,3,k)

              else

                  Gamma33 = dNidt*dNkdt

              endif

              Gamma =Gamma11*stress(1)+ (Gamma12)*stress(4)+
     1        (Gamma13)*stress(5) + Gamma22*stress(2)+
     2        (Gamma23)*stress(6) + Gamma33*stress(3)

              Kgdd(node_st,indexcol) =  Gamma
              Kgdd(node_st+1,indexcol+1) =  Gamma
              Kgdd(node_st+2,indexcol+2) =  Gamma

              indexcol = indexcol+3 !update index of columns

          enddo !end k

          node_st = node_st+3 !update index of rwos
```

```
78        enddo !end i


          return
          end
```

References

[1] Griffith A. The phenomena of rupture and flow in solids. Philos Trans A 1920;221:163–98. http://dx.doi.org/10.1098/rsta.1921.0006.
[2] Francfort G, Marigo J-J. Revisiting brittle fracture as an energy minimization problem. J Mech Phys Solids 1998;46(8):1319–42. http://dx.doi.org/10.1016/S0022-5096(98)00034-9.
[3] Bourdin B, Francfort GA, Marigo JJ. Numerical experiments in revisited brittle fracture. J Mech Phys Solids 2000;48(4):797–826. http://dx.doi.org/10.1016/S0022-5096(99)00028-9.
[4] Amor H, Marigo J-J, Maurini C. Regularized formulation of the variational brittle fracture with unilateral contact: Numerical experiments. J Mech Phys Solids 2009;57(8):1209–29. http://dx.doi.org/10.1016/j.jmps.2009.04.011.
[5] Miehe C, Hofacker M, Welschinger F. A phase field model for rate-independent crack propagation: Robust algorithmic implementation based on operator splits. Comput Methods Appl Mech Engrg 2010;199:2765–78. http://dx.doi.org/10.1016/j.cma.2010.04.011.
[6] Freddi F, Royer-Carfagni G. Regularized variational theories of fracture: A unified approach. J Mech Phys Solids 2010;58(8):1154–74. http://dx.doi.org/10.1016/j.jmps.2010.02.010.
[7] Steinke C, Kaliske M. A phase-field crack model based on directional stress decomposition. Comput Mech 2019;63(5):1019–46. http://dx.doi.org/10.1007/s00466-018-1635-0.
[8] Wu J-Y, Nguyen VP. A length scale insensitive phase-field damage model for brittle fracture. J Mech Phys Solids 2018;119:20–42. http://dx.doi.org/10.1016/j.jmps.2018.06.006.
[9] Dean A, Asur Vijaya Kumar P, Reinoso J, Gerendt C, Paggi M, Mahdi E, et al. A multi phase-field fracture model for long fiber reinforced composites based on the puck theory of failure. Compos Struct 2020;251:112446. http://dx.doi.org/10.1016/j.compstruct.2020.112446.
[10] Alessi R, Marigo J-J, Vidoli S. Gradient damage models coupled with plasticity and nucleation of cohesive cracks. Arch Ration Mech Anal 2014;214(2):575–615. http://dx.doi.org/10.1007/s00205-014-0763-8.
[11] Duda FP, Ciarbonetti A, Sánchez PJ, Huespe AE. A phase-field/gradient damage model for brittle fracture in elastic–plastic solids. Int J Plast 2015;65:269–96. http://dx.doi.org/10.1016/j.ijplas.2014.09.005.
[12] Ambati M, Kruse R, De Lorenzis L. A phase-field model for ductile fracture at finite strains and its experimental verification. Comput Mech 2016;57(1):149–67. http://dx.doi.org/10.1007/s00466-015-1225-3.
[13] Borden MJ, Hughes TJ, Landis CM, Anvari A, Lee IJ. A phase-field formulation for fracture in ductile materials: Finite deformation balance law derivation, plastic degradation, and stress triaxiality effects. Comput Methods Appl Mech Engrg 2016;312:130–66. http://dx.doi.org/10.1016/j.cma.2016.09.005, phase Field Approaches to Fracture.
[14] Dittmann M, Aldakheel F, Schulte J, Wriggers P, Hesch C. Variational phase-field formulation of non-linear ductile fracture. Comput Methods Appl Mech Engrg 2018;342:71–94. http://dx.doi.org/10.1016/j.cma.2018.07.029.
[15] Dean A, Reinoso J, Jha N, Mahdi E, Rolfes R. A phase field approach for ductile fracture of short fibre reinforced composites. Theor Appl Fract Mech 2020;106:102495. http://dx.doi.org/10.1016/j.tafmec.2020.102495.
[16] Abrari Vajari S, Neuner M, Arunachala PK, Ziccarelli A, Deierlein G, Linder C. A thermodynamically consistent finite strain phase field approach to ductile fracture considering multi-axial stress states. Comput Methods Appl Mech Engrg 2022;400:115467. http://dx.doi.org/10.1016/j.cma.2022.115467.
[17] Wu J-Y, Mandal TK, Nguyen VP. A phase-field regularized cohesive zone model for hydrogen assisted cracking. Comput Methods Appl Mech Engrg 2020;358:112614. http://dx.doi.org/10.1016/j.cma.2019.112614.
[18] Zhao Y, Wang R, Martínez-Pañeda E. A phase field electro-chemo-mechanical formulation for predicting void evolution at the Li–electrolyte interface in all-solid-state batteries. J Mech Phys Solids 2022;167:104999. http://dx.doi.org/10.1016/j.jmps.2022.104999.
[19] Ulloa J, Noii N, Alessi R, Aldakheel F, Degrande G, François S. Variational modeling of hydromechanical fracture in saturated porous media: A micromechanics-based phase-field approach. Comput Methods Appl Mech Engrg 2022;396:115084. http://dx.doi.org/10.1016/j.cma.2022.115084.
[20] Hageman T, Martínez-Pañeda E. A phase field-based framework for electro-chemo-mechanical fracture: Crack-contained electrolytes, chemical reactions and stabilisation. Comput. Methods Appl. Mech. Eng. 2023;415:116235. http://dx.doi.org/10.1016/j.cma.2023.116235.
[21] Quinteros L, García-Macías E, Martínez-Pañeda E. Electromechanical phase-field fracture modelling of piezoresistive CNT-based composites. Comput Methods Appl Mech Engrg 2023;407:115941. http://dx.doi.org/10.1016/j.cma.2023.115941.
[22] Abrari Vajari S, Neuner M, Arunachala PK, Linder C. Investigation of driving forces in a phase field approach to mixed mode fracture of concrete. Comput Methods Appl Mech Engrg 2023;417:116404. http://dx.doi.org/10.1016/j.cma.2023.116404.
[23] Gültekin O, Dal H, Holzapfel GA. A phase-field approach to model fracture of arterial walls: Theory and finite element analysis. Comput Methods Appl Mech Engrg 2016;312:542–66. http://dx.doi.org/10.1016/j.cma.2016.04.007, phase Field Approaches to Fracture.
[24] Bleyer J, Alessi R. Phase-field modeling of anisotropic brittle fracture including several damage mechanisms. Comput Methods Appl Mech Engrg 2018;336:213–36. http://dx.doi.org/10.1016/j.cma.2018.03.012.
[25] Mitrou A, Arteiro A, Reinoso J, Camanho PP. Modeling fracture of multidirectional thin-ply laminates using an anisotropic phase field formulation at the macro-scale. Int J Solids Struct 2023;273:112221. http://dx.doi.org/10.1016/j.ijsolstr.2023.112221.
[26] Ulmer H, Hofacker M, Miehe C. Phase field modeling of fracture in plates and shells. PAMM 2012;12(1):171–2. http://dx.doi.org/10.1002/pamm.201210076, arXiv:https://onlinelibrary.wiley.com/doi/pdf/10.1002/pamm.201210076.
[27] Amiri F, Millán D, Shen Y, Rabczuk T, Arroyo M. Phase-field modeling of fracture in linear thin shells. Theor Appl Fract Mech 2014;69:102–9. http://dx.doi.org/10.1016/j.tafmec.2013.12.002, introducing the new features of Theoretical and Applied Fracture Mechanics through the scientific expertise of the Editorial Board.
[28] Areias P, Rabczuk T, Msekh M. Phase-field analysis of finite-strain plates and shells including element subdivision. Comput Methods Appl Mech Engrg 2016;312:322–50. http://dx.doi.org/10.1016/j.cma.2016.01.020, phase Field Approaches to Fracture.
[29] Paul K, Zimmermann C, Duong TX, Sauer RA. Isogeometric continuity constraints for multi-patch shells governed by fourth-order deformation and phase field models. Comput Methods Appl Mech Engrg 2020;370:113219. http://dx.doi.org/10.1016/j.cma.2020.113219.
[30] Kikis G, Ambati M, De Lorenzis L, Klinkel S. Phase-field model of brittle fracture in Reissner–Mindlin plates and shells. Comput Methods Appl Mech Engrg 2021;373:113490. http://dx.doi.org/10.1016/j.cma.2020.113490.
[31] Parisch H. A continuum-based shell theory for non-linear applications. Internat J Numer Methods Engrg 1995;38(11):1855–83. http://dx.doi.org/10.1002/nme.1620381105.

[32] Schwarze M, Reese S. A reduced integration solid-shell finite element based on the eas and the ans concept—large deformation problems. Internat J Numer Methods Engrg 2011;85(3):289–329. http://dx.doi.org/10.1002/nme.2966.
[33] Bishara D, Jabareen M. Does the classical solid-shell element with the assumed natural strain method satisfy the three-dimensional patch test for arbitrary geometry? Finite Elem Anal Des 2020;168:103331. http://dx.doi.org/10.1016/j.finel.2019.103331.
[34] Alves de Sousa RJ, Cardoso RPR, Fontes Valente RA, Yoon J-W, Grácio JJ, Natal Jorge RM. A new one-point quadrature enhanced assumed strain (EAS) solid-shell element with multiple integration points along thickness—Part II: Nonlinear applications. Internat J Numer Methods Engrg 2006;67(2):160–88. http://dx.doi.org/10.1002/nme.1609.
[35] Kumar PKAV, Dean A, Sahraee S, Reinoso J, Paggi M. Non-linear thermoelastic analysis of thin-walled structures with cohesive-like interfaces relying on the solid shell concept. Finite Elem Anal Des 2022;202:103696. http://dx.doi.org/10.1016/j.finel.2021.103696.
[36] Asur Vijaya Kumar PK, Dean A, Reinoso J, Paggi M. Nonlinear thermo-elastic phase-field fracture of thin-walled structures relying on solid shell concepts. Comput Methods Appl Mech Engrg 2022;396:115096. http://dx.doi.org/10.1016/j.cma.2022.115096.
[37] Ambati M, De Lorenzis L. Phase-field modeling of brittle and ductile fracture in shells with isogeometric nurbs-based solid-shell elements. Comput Methods Appl Mech Engrg 2016;312:351–73. http://dx.doi.org/10.1016/j.cma.2016.02.017, phase Field Approaches to Fracture.
[38] Reinoso J, Paggi M, Linder C. Phase field modeling of brittle fracture for enhanced assumed strain shells at large deformations: sormulation and finite element implementation. Comput Mech 2017;59(6):981–1001. http://dx.doi.org/10.1007/s00466-017-1386-3.
[39] Asur Vijaya Kumar PK, Dean A, Reinoso J, Paggi M. Thermo-elastic solid shell formulation with phase field fracture for thin-walled FGMS. Thin-Walled Struct 2022;179:109535. http://dx.doi.org/10.1016/j.tws.2022.109535.
[40] Kumar PKAV, Dean A, Sahraee S, Reinoso J, Paggi M. Non-linear thermoelastic analysis of thin-walled structures with cohesive-like interfaces relying on the solid shell concept. Finite Elem Anal Des 2022;202:103696. http://dx.doi.org/10.1016/j.finel.2021.103696.
[41] Liu Z, Reinoso J, Paggi M. Phase field modeling of brittle fracture in large-deformation solid shells with the efficient quasi-newton solution and global–local approach. Comput Methods Appl Mech Engrg 2022;399:115410. http://dx.doi.org/10.1016/j.cma.2022.115410.
[42] Linder C, Tkachuk M, Miehe C. A micromechanically motivated diffusion-based transient network model and its incorporation into finite rubber viscoelasticity. J Mech Phys Solids 2011;59(10):2134–56. http://dx.doi.org/10.1016/j.jmps.2011.05.005.
[43] Valverde-González A, Reinoso J, Jha NK, Merodio J, Paggi M. A phase field approach to fracture for hyperelastic and visco-hyperelastic materials applied to pre-stressed cylindrical structures. Mech Adv Mater Struct 2022;1–20. http://dx.doi.org/10.1080/15376494.2022.2121452.
[44] Chester S. 2008.
[45] Bourdin B, Francfort GA, Marigo JJ. The variational approach to fracture. Springer Netherlands; 2008, http://dx.doi.org/10.1007/s10659-007-9107-3.
[46] Bischoff M, Ramm E. Shear deformable shell elements for large strains and rotations. Internat J Numer Methods Engrg 1997;40(23):4427–49. http://dx.doi.org/10.1002/(SICI)1097-0207(19971215)40:23<4427::AID-NME268>3.0.CO;2-9.
[47] Vu-Quoc L, Tan X. Optimal solid shells for non-linear analyses of multilayer composites. I. Statics. Comput Methods Appl Mech Engrg 2003;192(9):975–1016. http://dx.doi.org/10.1016/S0045-7825(02)00435-8.
[48] Dvorkin E, Bathe K-J. A continuum mechanics based four-node shell element for general nonlinear analysis. Eng Comput 1984;1:77–88. http://dx.doi.org/10.1108/eb023562.
[49] Betsch P, Stein E. An assumed strain approach avoiding artificial thickness straining for a non-linear 4-node shell element. Commun Numer Methods Eng 1995;11(11):899–909. http://dx.doi.org/10.1002/cnm.1640111104.
[50] Reinoso J, Blázquez A. Application and finite element implementation of 7-parameter shell element for geometrically nonlinear analysis of layered CFRP composites. Compos Struct 2016;139:263–76. http://dx.doi.org/10.1016/j.compstruct.2015.12.009.
[51] Simo J, Hughes T. Computational inelasticity. Interdisciplinary applied mathematics, New York: Springer; 2000, http://dx.doi.org/10.1007/b98904.
[52] Bridgman PW. Studies in large plastic flow and fracture. Cambridge, MA and London, England: Harvard University Press; 1964, http://dx.doi.org/10.4159/harvard.9780674731349.
[53] McClintock FA. A criterion for ductile fracture by the growth of holes. J Appl Mech 1968;35(2):363–71. http://dx.doi.org/10.1115/1.3601204.
[54] Rice J, Tracey D. On the ductile enlargement of voids in triaxial stress fields. J Mech Phys Solids 1969;17(3):201–17. http://dx.doi.org/10.1016/0022-5096(69)90033-7.
[55] Gurson AL. Continuum theory of ductile rupture by void nucleation and growth: Part I—Yield criteria and flow rules for porous ductile media. J Eng Mater Technol 1977;99(1):2–15. http://dx.doi.org/10.1115/1.3443401.
[56] Tvergaard V, Needleman A. Analysis of the cup-cone fracture in a round tensile bar. Acta Metall 1984;32(1):157–69. http://dx.doi.org/10.1016/0001-6160(84)90213-X.
[57] Ambati M, Gerasimov T, De Lorenzis L. Phase-field modeling of ductile fracture. Comput Mech 2015;55(5):1017–40. http://dx.doi.org/10.1007/s00466-015-1151-4.
[58] Xue L. Ductile fracture modeling: theory, experimental investigation and numerical verification. Massachusetts Institute of Technology; 2009.
[59] Baragetti S, Villa F. A numerical model to assess the role of crack-tip hydrostatic stress and plastic deformation in environmental-assisted fatigue cracking. Corros Rev 2017;35(4–5):343–53. http://dx.doi.org/10.1515/corrrev-2017-0017.